3D short fatigue crack investigation in beta titanium alloys using phase and diffraction contrast tomography

Michael Herbig

N° d'ordre 2011-ISAL-0010 Année 2011

Thèse

présentée devant:

L'Institut National des Sciences Appliquées de Lyon

par

Michael HERBIG

pour obtenir le grade de docteur

Ecole doctorale : Matériaux de Lyon

3D Short Fatigue Crack Investigation in Beta Titanium Alloys using Phase and Diffraction Contrast Tomography

Soutenue le 26 janvier 2011

Jury:

M. Ulrich Krupp	rapporteur
M. Maxime Sauzay	rapporteur
M. Haël Mughrabi	examinateur
M. Jean Petit	examinateur
M. Henry Proudhon	examinateur
M. Jean-Yves Buffière	directeur de thèse
M. Wolfgang Ludwig	directeur de thèse

Dedicated to
Mama, Papa, Oma und Aileen

There are people who relate the extinction of the dinosaurs to the disrespect of deadlines (see figure to the right). Obviously, a PhD student not respecting the deadline of his thesis submission has a less global, but still severe personal impact. I want to thank Dan Regan[1], whose cartoon made me clear where the expression "deadline" comes from. It gave me the needed motivation to finish my work in time. I depicted this cartoon here in order to support all others sharing my situation.

Michael Herbig[2], Grenoble, December 2010

Dan Regan, "The reason why...".

[1] Hallmark Cards Inc., Kansas City, Missouri, USA
[2] Herbig.Michael@gmail.com

Acknowledgments

I'd like to thank:

My supervisors and friends Jean-Yves Buffière and Wolfgang Ludwig for the very pleasant team work, for their time, support, hospitality and all the fun we had.

The INSA Lyon and the French government for financing this thesis.ing this thesis.

The ESRF for hosting me and supporting my work with the best possible service and equipment.

The whole team of ID19 for the help and the pleasant atmosphere. For the help concerning holotomography and ring correction special thanks go to Max Langer and Paul Tafforeau, respectively.

My office mate Lukas Helfen for, apart from the help concerning science, many entertaining hours and for financiating my excessive coffee consumption.

The "grain trackers" Wolfgang Ludwig, Péter Reischig, Andrew King, Greg Johnson and Sabine Roland du Roscoat who have been developing the DCT code.

Andrew King on whose ideas many fundamental principles of this work are based on, as e.g. using a mesh to visualize surface orientation. Also the pole figures shown here were done using his scripts.

Henry Proudhon for the excellent scientific collaboration, for hosting me so nicely during my stays in Paris, and him and the Ecole de Mines, ParisTech for the financial support at the end of my thesis.

Christoph Böttger from the University of Darmstadt who has been working on the automatization of the registration procedure.

My colleagues from the ESRF and ILL: Andrew Fitch and Adrian Hill for the XRD measurements, Alexei Bosak for the IXS experiments and Claudio Ferrero and Matthia Allieta for the SAXS measurements and interpretation.

Andreas Müller and Jakob Wilfert from the Max Planck institutes for metal and for solid state research in Stuttgart for the FESEM experiment.

Fernando Warchomicka from the Technical University of Vienna for supplying us with material and the characterization of VST55531.

Ingmar Roth, Helge Knobbe and Hans-Jürgen Christ from Siegen for supporting me with material and helping with the EBSD interpretation.

Erik Lauridsen from Risø National Laboratory, Denmark and Richard Fonda from the Naval Research Laboratory, Washington DC, for supplying us with Beta21S and helping us with the heat treatment decorating the grain boundaries.

Frédéric Lorut from ST Microelectronics, Crolles, for FIB sample machining

Shigehisa Naka and Ladislas Kubin from CNRS-ONERA, Maxime Sauzay from CEA Saclay, David Embury from McMaster University, Yves Brechet and Marc Fivel from SIMAP Grenoble, André Pineau from Mines Paristech and James Marrow from Oxford University for helpful and informative discussions. Special thanks to Haël Mughrabi from Erlangen University for all his support and all the time he spent to answer my questions.

All my friends and colleagues at the ESRF and at INSA Lyon that made my stay in Lyon and Grenoble so pleasant.

Abstract

X-Ray Diffraction Contrast Tomography (DCT) is a recently developed, non-destructive synchrotron imaging technique which characterizes microstructure and grain orientation in polycrystalline materials in three dimensions (3D). By combining it with propagation based phase contrast tomography (PCT) it is for the first time possible to observe in situ the 3D propagation behavior of short fatigue cracks (SFCs) within a set of fully characterized grains (orientation and shape). The combined approach, termed 3-Dimensional X-ray Tomography of Short cracks and Microstructure (3DXTSM), has been developed on the metastable β titanium alloy "Beta21S".

A big part of this work deals with the challenges encountered during development of the 3DXTSM methodology. In the combined dataset, each point on the 3D fracture surface can be associated with a multidimensional data structure containing variables describing the grain orientation, the local fracture surface normal and the propagation history. The method uses a surface mesh composed of triangles that describes the crack (in other words: the fracture surface) in the last propagation state measured. Grain orientations, crack fronts, local growth rates and grain boundaries can be visualized by assigning colors to this mesh. The data structure can be interrogated in a number of different ways. Tools for extracting pole figures and pole density distribution functions have been implemented. An algorithm was developed that is capable of measuring the 3D local growth rate of a crack containing branches. The accuracy of the grain boundaries as reconstructed with DCT was evaluated and the elastic constants of Beta21S were determined.

The first experiment, conducted on the metastable β titanium alloy Beta21S, allowed to establish and validate the 3DXTSM methodology itself. The quantitative analysis of crack propagation in this alloy was compromised by the fact that changes in crack propagation behavior occur at length scales which could only partly be resolved with the experimental settings used. Apart from the resolution the slip character was identified as one of the key factors that decide in how far the measured data represents reality and thereby about the data interpretability. A second 3DXTSM experiment using optimized conditions was designed and conducted on the near beta alloy "VST55531". The observation of crystallographic growth behavior in this alloy confirms the prevalence of stage I crack propagation.

Due to the 3D nature of this study it could be observed that the orientation of the corrugated fracture surface patterns visible during stage I is independent of the crack

growth direction. The characteristics of stage I and II were correspondingly revised. No correlation between slip directions and growth direction of a crack propagating on a single slip plane was observed.

The crystallographic orientation of the fracture facets observed do not correspond to the most activated slip systems (Schmid factor). This suggests that modifications of the stress field due to the 3D crack geometry and the elastic anisotropy of the material need to be taken into account to model crack propagation. This could be achieved, in future work, using crystal plasticity finite element simulations.

Key words: 3D, short fatigue crack, synchrotron imaging, beta titanium, phase contrast tomography, diffraction contrast tomography

Résumé

La tomographie en contraste de diffraction est une nouvelle technique non destructive d'imagerie synchrotron qui caractérise la microstructure et l'orientation des grains dans les matériaux polycristallins en trois dimensions (3D). En la combinant avec la tomographie par contraste de phase, il est pour la première fois possible d'observer in situ la propagation 3D des fissures de fatigue courtes au sein d'un ensemble de grains entièrement caractérisé (orientation et forme). L'approche combinée, appelée "tomographie tri-dimensionelle par rayons X des fissures courtes et de la microstructure" (T3DXFM), a été développée sur l'alliage de titane métastable "Beta21S". Une grande partie de ce travail porte sur le développement de la méthodologie T3DXFM. Dans le jeu de données combinées, chaque point de la surface de rupture 3D peut être associé à une structure de données multidimensionnelle contenant des variables décrivant l'orientation des grains, l'orientation locale de la surface de rupture ainsi que l'histoire de la propagation. La méthode utilise un maillage de surface composé de triangles qui décrit la fissure (en d'autres termes: la surface de rupture) dans l'état de propagation mesuré au dernier cycle de fatigue réalisé. Les orientations des grains, les différents fronts de la fissure, les vitesses de croissance locales ainsi que les joints de grains peuvent être visualisés en attribuant des couleurs à ce maillage. Des outils d'extraction des figures de poles ont été créés et mis en œuvre. Un algorithme a été développé qui est capable de mesurer la vitesse de propagation locale 3D d'une fissure contenant des branchements. La précision des joints de grains reconstitué avec TCD a été évaluée et les constantes élastiques de Beta21S ont été déterminées.

Mots de clés : 3D, fissures courtes de fatigue, imagerie synchrotron, titane béta, tomographie par contraste de phase, tomographie par contraste de diffraction

Résumé substantiel

Introduction et contexte Le mécanisme de propagation des fissures longues de fatigue est assez bien compris et pris en compte, depuis de nombreuses années, dans les concepts d'intégrité structurale, par exemple, dans l'industrie aéronautique ou nucléaire. L'extension de la prédiction de la durée de vie au régime de la fatigue à grand nombre de cycles, où l'amorçage et la croissance des fissures courtes de fatigue sont les mécanismes d'endommagement prédominants, rendrait l'utilisation de matériaux d'ingénierie plus efficace. Toutefois, les fissures courtes de fatigue (FCF) interagissent d'une manière très complexe avec la microstructurale locale, ce qui rend leur comportement difficilement prévisible.

Les chapitres 1 et 2 de ce travail décrivent les mécanismes qui sont responsable de la grande dispersion de la vitesse de propagation des fissures de fatigue courtes (figure 2.1). Plusieurs études antérieures ont montré que l'arrangement tri dimensionel local des orientations des grains et joints de grains (et/ou de phase) est la clé pour comprendre et décrire de manière quantitative la propagation des fissures courtes de fatigue. La compréhension actuelle du mécanisme de propagation des fissures de fatigue courtes à travers les joints de grains fait apparaître un paramètre essentiel qui est la position du joint de grain par rapport aux plans de glissement dans les grains adjacents. La fissure se propage sur un plan de glissement dans le premier grain jusqu'à ce que celui-ci atteigne la limite des grains. Si ce front de fissure ne correspond pas à une ligne d'intersection entre les plans de glissement dans le grain suivant et la surface du joint de grains, la fissure est entravée. Pour compenser cette incompatibilité une partie du joint de grain doit rompre, faute de quoi l'échantillon serait encore connecté au joint de grain empechant la fissure de s'ouvrir. Pour que cette rupture se produise, des mécanismes de plasticité doivent être activés localement ce qui ralentit la fissure en amont du joint de grain. La surface de rupture correspondante peut être minimisée par la formation d'une surface en «tôle ondulée» dans le grain si celui-ci est composé de deux plans de glissement alternatif (figure 6.12). Comme une surface de fracture ondulée implique un coût énergétique plus élevé qu'une rupture lisse la fissure se propage plus lentement [Schäf, 2010].

Afin d'obtenir une vue complète du comportement des FCF la microstructure 3D (forme des grains et orientation cristallographique) ainsi que la cinétique de propagation 3D des fissures doivent être connus. Les méthodes de caractérisation utilisées jusqu'à présent pour étudier la microstructure 3D ont mis en œuvre par polissage séquentiel

mécanique ou par faisceau d'ions focalisé combiné avec la caractérisation en électrons rétrodiffusés (Electron Back Scattering Diffraction - EBSD). A cause du caractère destructif de ces méthodes, il est seulement possible de caractériser la microstructure 3D et la forme de la fissure à un moment donné de la propagation. Par conséquent, la propagation de la fissure n'a été observée que sur la surface et les variations locales du taux de croissance sur la partie non visible du front de fissure ont été négligés.

Cette thèse porte sur le développement d'une technique de caractérisation qui donne, en raison de son caractère non destructif, accès à toutes les informations cruciales pour la caractérisation de la propagation des FCF. La tomographie en contraste de diffraction (TCD) est une nouvelle technique non destructive d'imagerie synchrotron qui caractérise la microstructure et l'orientation des grains dans les matériaux polycristallins en 3D. En la combinant avec la tomographie par contraste de phase (TCP), il est pour la première fois possible d'observer in situ la propagation 3D des fissures de fatigue courtes au sein d'un ensemble de grains entièrement caractérisé (orientation et forme). L'approche combinée, appelée "tomographie tri-dimensionnelle par rayons X des fissures courtes et de la microstructure" (T3DXFM), a été développée sur l'alliage de titane métastable "Beta21S". Dans ce matériau un traitement thermique peut être réalisé pour décorer les joints de grains avec des précipités alpha. Ces précipités peuvent être visualisés en 3D en utilisant la TCP [Dey et al., 2007], ce qui peut être utilisé pour une cartographie précise de la position des joints de grains. Ainsi la méthode TCD a pu être évaluée. L'erreur moyenne dans la position des joints de grains reconstitués par TCD est de l'ordre de 2-3 micromètres, pour une granulométrie moyenne de 55 micromètres. Un second matériau, l'alliage de titane bêta "VST55531", a également été étudié. En raison de sa stabilité thermodynamique plus élevée ce matériau est moins compliqué que l'alliage Beta21S tout en étant assez proche pour être comparable. Un traitement thermique a été appliqué sur l'alliage VST55531 qui entraine un mode de déformation plastique beaucoup plus planaire que pour le Beta21S, ce qui simplifie l'interprétation des données de T3DXFM.

Matériaux et méthodes Tous les détails des expériences, ainsi que la théorie nécessaire à la compréhension des méthodes utilisées sont donnés dans le chapitre 3. Au total, quatre échantillons de Beta21S et deux de VST55531 ont été utilisés dans cette étude (tableau 3.1). Tous les échantillons de Beta21S ont été mis en solution pendant deux heures à 850 °C et trempés à l'eau. Les deux échantillons de VST55531 ont été mis en solution pendant deux heures à 843 °C et refroidis à l'air. Ces traitements thermiques conduisent à une taille de grains moyenne de 55 μm dans le cas du Beta21S et de 65 μm dans le cas du VST55531. Pour tous les traitements thermiques l'encapsulation des échantillons dans des tubes de quartz était nécessaire afin d'éviter l'absorption des gaz atmosphériques. Les expériences de T3DXFM ont été menées pour étudier la croissance des fissures en 3D. La morphologie des fissures à la surface des échantillons a été étudiée en utilisant un microscope électronique à balayage classique (MEB) et à l'effet de champ (MEB-FEG). L'apparition de la transformation martensitique sous l'effet de la contrainte (TMSC) a été étudié sur la surface et dans le volume en utilisant l'EBSD

et la diffraction des rayons X (DRX). Les constantes élastiques de Beta21S nécessaires pour des simulations numériques ont été mesurées sur une feuille mince en utilisant la diffusion inélastique des rayons X (DIX): C_{11} = 153 GPa, C_{12} = 101 GPa et C_{44} = 57 GPa.

Les deux types de tomographie utilisées dans cette étude (tomographie par contraste de diffraction (TCD) et de phase (TCP)), partagent une configuration expérimentale similaire (figures 3.5, 3.9), mais exploitent des mécanismes de contrastes differents. Les deux méthodes ont en commune l'illumination de l'échantillon par un faisceau de rayonnement X synchrotron monochromatique qui est capté sur un détecteur d'imagerie haute résolution situé derrière l'échantillon; l'échantillon est mis en rotation pendant une série de radiographies est enregistrée, et à partir de ces images un volume 3D de l'échantillon est reconstruit à l'aide des techniques de reconstruction algébrique ou arithmétique.

La TCP exploite deux mécanismes de contraste, l'absorption et le déphasage des rayons X qui se propagent à travers l'échantillon. L'absorption est controlée par l'intégrale du coefficient d'atténuation le long du trajet du faisceau dans la métière et ne nécessite pas de propriétés d'onde particulière du faisceau incident. Le contraste de phase, par contre, est régi par l'indice de réfraction locale et nécessite un faisceau X cohérent. Dans les zones du matériau présentant un indice de réfraction élevée les rayons X se propagent plus lentement, ce qui provoque un déphasage du faisceau transmis et produit des franges d'interférence à la frontière entre les zones de haut et bas indices de réfraction. Le contraste de phase rend ainsi visibles les frontières entre des régions de haute et basse densité électronique qui ne sont pas visibles en contraste d'absorption. Ce qui signifie pour l'étude actuelle, que les parties de la fissure qui sont presque fermés ne sont visibles que grâce à la TCP.

La TCD est une technique d'imagerie synchrotron basée sur la diffraction de Bragg des grains dans un échantillon cristallin (figure 3.9): un monocristal mis en rotation dans un faisceau étendu de rayons X monochromatique diffracte chaque fois que la condition de Bragg entre le faisceau incident et les plans cristallographiques du monocristal et satisfaite. Un détecteur, plus grand que le faisceau direct et monté immédiatement derrière l'échantillon (distance typique de l'ordre de 3-6 mm), permet d'enregistrer une partie de ces événements de diffraction. Dans le faisceau transmis l'intensité diffractée est visible comme tache sombre (tache d'extinction), et dans le faisceau diffracté comme une tache plus claire (tache de diffraction). En première approximation (diffraction cinématique et gradients d'orientation dans le monocristal négligeables), la distribution d'intensité à l'intérieur des taches d'extinction et de diffraction correspond aux projections des volumes de grains dans le plan du détecteur. En utilisant la distribution de l'intensité des taches de diffraction lors de la rotation, la forme 3D du monocristal/grain peut être reconstruite par des techniques de reconstruction algébrique. L'orientation du grain peut être déduite de l'analyse des vecteurs de diffraction associés aux réflexions observées. La DCT applique ce principe à des polycristaux pour lesquels un algorithme supplémentaire doit être utilisé pour appairer les taches de diffraction et le grain du matériau qui diffracte.

Des essais de fatigue in situ ont été réalisés en utilisant une machine de fatigue dédiée qui peut être montée directement sur l'installation de tomographie (figure 3.10) [Buffière et al., 2006]. Les expériences ont été effectuées à amplitude de contrainte constante, à une fréquence de 25 Hz, à température ambiante avec une contrainte uniaxiale de traction cyclique variant de 10 à 320 MPa (R = 0,03). Les échantillons en forme d'haltère (figure 3.4) ont un diamètre compris entre 350 et 600 μm. Pour améliorer la précision de détection de la fissure les scans tomographiques ont été faits en maintenant l'échantillon sous charge afin de réduire au minimum les zones de contact entre les lèvres de la fissure. Une taille de voxel de 0,7 μm a été utilisée.

Data Processing Une grande partie de ce travail porte sur le développement de la méthodologie de la technique T3DXFM. Dans le jeu de données combinées, chaque point de la surface de rupture 3D peut être associé à une structure de données multi-dimensionnelle contenant des variables décrivant l'orientation des grains, l'orientation locale de la surface de rupture ainsi que l'histoire de la propagation. La méthode utilise un maillage de surface composé de triangles qui décrit la fissure (en d'autres termes: la surface de rupture) dans l'état de propagation mesuré au dernier cycle de fatigue réalisé. Les orientations des grains, les différents fronts de la fissure, les vitesses de croissance locales ainsi que les joints de grains peuvent être visualisés en attribuant des couleurs à ce maillage. Des outils d'extraction des figures de poles ont été créés et mis en œuvre. Un algorithme a été développé qui est capable de mesurer la vitesse de propagation locale 3D d'une fissure contenant des branchements.

Résultats Comme illustré dans le chapitre 5, le contenu d'un tel ensemble de données T3DXFM est trop étendu d'être illustré en une seule image. Mais en utilisant la structure de données décrite au chapitre 4, il est facile de visualiser de façon combinée plusieurs informations . La surface de rupture peut ainsi être montrée sous différents angles (figures 5.5 (b-d)), l'orientation physique (figures 5.5) ou cristallographique (figure 5.6) de la surface de rupture peut être visualisée. Les joints de grains ou les fronts de fissure peuvent également être ajoutés à la figure (figure 5.7a), la propagation de la fissure à différents nombres de cycles peut être vsualisée (figure 6.13), des sous-régions content un sous ensemble de grains peuvent être représentées (figure 6.11), du texte ainsi que des numéros facilitant l'identification des grains peuvent être ajoutés (figure 5.4), des plans de glissement semi-transparents peuvent être ajoutés (figure 6.10b) et des vidéos peuvent être créées, montrant plusieurs aspects de la propagation de la fissure (voir la vidéo rattachée à la publication en ligne [Herbig et al., 2011]). Des statistiques sur les orientations ont été réalisées à partir des figures de pôles. Une version simple, traçant un symbole pour chaque pôle, a été utilisée pour comparer l'activation des plans de glissement et la distribution d'orientation de la surface de rupture dans un grain donné (figure 5.10). Une version plus sophistiquée représentant la densité de pôles a été utilisée pour analyser la texture (figure 5.12) ainsi que la distribution en densité des pôles (figure 5.11).

Discussion et conclusions Les chapitres 6 et 7 contiennent la discussion et la conclusion, respectivement. Pour le Beta21S, l'étude de la transformation martensitique sous contrainte (TMSC) par MEB, EBSD, MEB-FEG et DRX montre que la fraction volumique de phase transformée, si elle existe, se situe en dessous de la limite de sensibilité de ces méthodes; son impact sur le champ de contrainte et la direction de propagation de fissures doit donc être négligeable. Pour l'alliage VST55531 l'apparition de TMSC peut être exclue, en raison principalement de la composition de l'alliage, mais aussi en raison du traitement thermique appliqué.

La qualité des reconstructions de la TCP dépend de manière critique des paramètres d'acquisition. Les meilleures conditions d'imagerie, telle qu'évaluées sur l'échantillon VST55531 (installé dans la machine de fatigue) sont les suivantes: une distance échantillon-détecteur de 49 mm, une énergie de 52 keV, une taille de pixel de 0,7 μm et au moins 1500 projections. Pour des raisons de qualité d'image et de temps d'exposition l'utilisation d'une machine de fatigue plus petite (plus faible diamètre du tube polymère) serait fortement souhaitable. Cela permettrait de travailler à des distances plus courtes, et réduirait les artefacts causés par le contraste de phase. Une réduction du poids de la machine de fatigue permettrait également de réduire les inexactitudes mécanique (par exemple l'oscillation de la platine de rotation), qui est l'un des facteurs limitant pour la résolution spatiale ultime réalisables avec l'instrument actuel.

Le sur-échantillonage des données tomographiques a été identifié comme une étape obligatoire du traitement d'image pour préserver les caractéristiques morphologiques à l'échelle de la résolution lors de la conversion de la fissure en un maillage de surface à partir des données de volume.

L'orientation cristallographique de la surface de rupture mesurée pour l'alliage Beta21S ne correspond pas, en majorité, aux plans de glissement attendus pour la structure cubique centrée. Ce fait ne peut pas s'expliquer par des erreurs de mesure et doit donc être causé par des changements de la direction de propagation de la fissure se produisant à des échelles de longueur qui ne peuvent être résolu qu'en partie avec l'installation expérimentale utilisée. Les observations de la surface de l'échantillon en MEB et MEB-FEG mettent effectivement en évidence de tels changements de direction. Outre la résolution, le caractère plus ou moins planaire/cristallographique du glissement a été identifié comme un des facteurs clés qui décident dans quelle mesure les données mesurées représentent le chemin de fissuration réel et, autorisent, par conséquent, une interprétation correcte des données.

Les deux fissures caractérisées dans les alliages Beta21S et VST55531 dans cette étude étaient des fissures de stade I jusqu'à la dernière étape mesurée. La différence principale entre les deux systèmes de matériaux, est que dans le cas du VST55531 les changements de la direction de propagation de la fissure sont moins fréquents. La distance sur laquelle une fissure se propage sur un plan de glissement avant d'en adopter un autre peut, en principe, descendre à l'échelle atomique. Le rapport entre cette distance et la résolution est d'une grande importance pour la T3DXFM. Si la fissure reste suffisamment longtemps sur un seul plan (environ 10 μm à la résolution utilisée dans cette étude) l'orientation de la surface de rupture mesurée correspond bien à l'orientation

réelle. Si la distance entre les changements de plans est proche de cette valeur, mais plus petite, les changements de plans sont visibles comme stries périodiques sur la surface de rupture (figure 6.11, grains d et m). Si la distance est très courte les changements de plans ne sont plus visibles et la normale de la surface de rupture mesurée est une combinaison linéaire des normales des plans de glissement mis en jeu. Afin d'être en mesure d'interpréter correctement les données T3DXFM, des matériaux qui montrent un caractère de glissement planaire doivent donc être utilisés.

Puisque, selon nos résultats, nous ne pouvons pas trouver une différence significative entre ce qui est appelé glissement simples et doubles dans la littérature nous proposons de classer les fissures en stade I de fatigue en fonction de leur *fréquence* de changements de plan.

Une fissure en stade I - basse fréquence n'a pas de direction de croissance constante dans les polycristaux (figure 6.10). Cela implique également qu'il n'y a pas de relation directe entre la direction de croissance locale et la (les) direction(s) de glissement au sein du plan de glissement suivi. Les stries sur la surface de rupture d'une fissure en stade I sont différents en morphologie, orientation, espacement et continuité de celles de stade II. Cette observation peut aider à identifier le stade de croissance par inspection de la surface de rupture post-mortem.

Grâce à la nature 3D de cette étude, on a pu clairement mettre en évidence que l'orientation des stries visible sur la surface de rupture dans une fissure de fatigue en stade I est indépendante de la direction de croissance de la fissure (figure 6.11). Les caractéristiques stade I et II ont été révisées en conséquence.

Dans la plupart des cas l'orientation cristallographique de la surface de rupture mesurée ne correspond pas aux systèmes de glissement les plus activés (facteur de Schmid le plus grand). Ceci suggère que les modifications du champ de contrainte dues à la géométrie de la fissure 3D et à l'anisotropie élastique du matériau doivent être pris en compte pour la modélisation de la propagation de la fissure. Cela pourrait être réalisé, dans des travaux futurs, en utilisant des simulations de type plasticité cristalline.

Contents

Chapter 1

Introduction

The expression "fatigue" in materials science describes a failure phenomenon that occurs during cyclic loading. During each cycle damage is accumulated which finally leads to failure. For economical as for safety reasons the phenomenon is of great importance since most of the structural parts are exposed to varying stress fields. For example parts that experience vibrations, or that are subjected to heat or pressure changes, like engines, bridges, turbines or pipes, are all concerned. Engineers generally accept that every cyclically loaded part can fail eventually and will try to work with lifetime predictions. Since fatigue lifetimes exhibit a certain variability, safety factors have to be applied in order to make sure that crucial parts are exchanged before they fail. However, exchanging parts which could last longer has a direct effect on cost. By measuring the length of existing cracks at regular intervals a more precise failure prediction can be done and the safety factors can be reduced. However, during most of the fatigue life, cracks cannot be detected by visual inspection because they are too small [Schijve, 2009]. This part of the fatigue life corresponds to the initiation and growth of short fatigue cracks (SFCs, typical length $<$ 1 mm). Only in the last 5-10 % of its lifetime the crack is long enough to allow its propagation rate to be described by empirical laws such as the Paris law [Shiozawa and Matsushita, 1996; Paris and Erdogan, 1960]. Hence, even small improvements in the material's behavior during the SFC period can have a large impact on the overall life time. Investigating the mechanisms of short fatigue crack propagation can help in two ways: first, more fatigue resistant materials can be designed. Second, by creating more accurate models for failure prediction safety factors and thereby costs can be reduced. The aim of this work is to develop and use new non-destructive characterization techniques to study SFCs in-situ, in order to improve our understanding of their behavior.

Chapter 2

Background

2.1 Introduction to Short Fatigue Cracks

Davidson et al. [Davidson et al., 2003] point out that in the USA people distinguish between short and small cracks while in Europe the expressions are used as equivalents. This work follows the European convention to always speak of short cracks. The so called "short crack problem" was identified by Pearson in 1975 [Pearson, 1975] who drew a lot of attention to the topic. While the growth rate of long fatigue cracks (LFCs) can be predicted using the Paris law [Paris and Erdogan, 1960], describing the behavior of SFCs was found to be much more difficult. Pearson found out that short surface flaws grew up to 100 times faster than longer flaws when being subjected to the same nominal value of the stress intensity range ΔK. The "short crack problem" arises because the usual prediction of the growth rate by measuring the crack length and calculating ΔK using linear elastic fracture mechanics (LEFM) fails for the regime of short fatigue cracks, resulting in a problem for lifetime predictions. Davidson et al. summarize the growth behavior of SFCs as follows: SFCs can grow faster than would be predicted by the extrapolated Paris law than corresponding LFCs at the same ΔK. Significant growth rates are measured below ΔK_{th}, the threshold value of the stress intensity range below which LFCs do not grow. While the growth rate of long fatigue cracks normally increases with increasing ΔK the growth rates of SFCs are observed to increase, decrease or remain constant with increasing ΔK. Additionally, compared to the growth rates of LFCs there is a large scatter in the growth rates of SFCs [Krupp, 2007; Davidson et al., 1996] (figure 2.1). In practice this means that the growth laws of SFCs are different from the ones of LFCs.

The general behavior of SFCs is schematically drawn in figure 2.2. Right after initiation SFCs are described as slowing down continuously. Depending on the grain size the cracks arrest or are delayed due to microstructural barriers like phase or grain boundaries [Miller et al., 1986]. The crack completely stops for ΔK values below ΔK_{th}, otherwise the growth rate increases again after the barrier is overcome. Krupp [Krupp, 2007] states that the minimum growth rate is determined by how much plasticity is induced in the next grain after the crack front. There is a preferential propagation

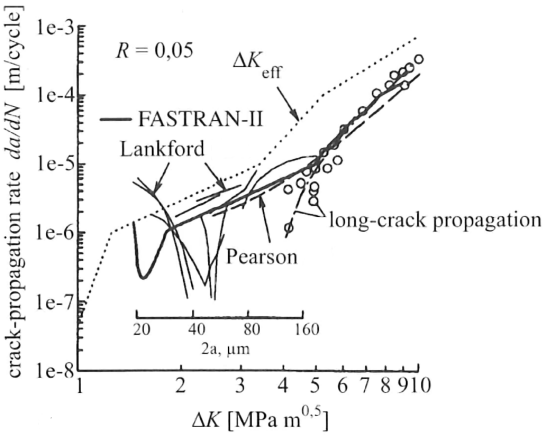

Figure 2.1: Illustration by [Krupp, 2007; Newman. et al., 1999] showing the scatter in the growth rates of short fatigue cracks [Pearson, 1975; Lankford, 1982] and comparing to the values calculated by the program FASTRAN-II [Newman, 1992].

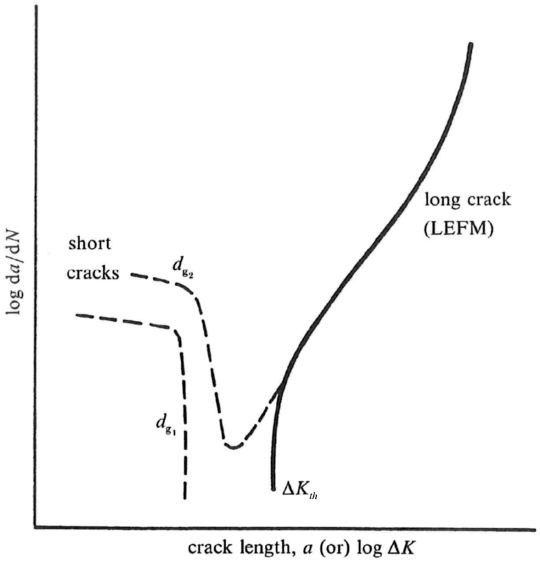

Figure 2.2: Schematic comparison between the growth rate of short and of long fatigue cracks for two different grain sizes d_g with $d_{g2} > d_{g1}$ [Suresh, 2003].

of microstructurally SFCs (see section 2.2) along low-index slip planes [Ruppen et al., 1979]. Krupp concludes that not the grain but the slip plane misorientation between two adjacent grains is important. The mechanism can be described as follows for materials with planar slip character: when the slip planes are not completely compatible the dislocation pile up in front of the grain boundary which leads to a stress concentration at dislocation sources in the next grain. The closer the crack comes to the grain boundary the higher the dislocation pile-up, thereby the higher the force driving against the crack propagation and the slower the crack propagation. The slip continuation or transmission takes place when a critical stress is exceeded. If the grains are bigger more dislocations can pile up which increases the stress on the dislocation sources in the neighboring grains. Thereby, a bigger grain size means a reduced barrier effect of the grain boundaries (Hall-Petch relationship) and thus a lower fatigue limit. Since the crack will slow down and accelerate again at all grain boundaries where the slip planes

are not compatible an oscillation of the growth rate is measured [Blom et al., 1986]. As high angle grain misorientations often coincide with high angle slip plane misorientation, high angle grain boundaries are often reported as effective dislocation barriers and thereby have a crack arresting or retarding effect, while low angle grain boundaries don't impede crack propagation [Newman. et al., 1999; Lankford, 1982], but this topic is still controversial. Zhai and al. describe the misorientation between two slip planes with a twist and a tilt angle [Zhai et al., 2000, 2005]. A big twist angle strongly retards crack propagation whereas the tilt angle has less influence. According to Zhai rupture has to happen along the grain boundary to bridge the incompatible slip planes in the adjacent grains. Since the twist angle is proportional to the amount of rupture it is also proportional to the crack retardation. After recent insights by Schäf [Schäf, 2010; Schäf et al., 2011] the mechanism of the SFC propagation across a grain boundary might be summarized as follows: what is essential is the position of the grain boundary with respect to the slip planes in the adjacent grains. The crack propagates on a slip plane in the first grain until it reaches the grain boundary. If this crack front is not compatible with one of the intersection lines between the slip planes in the next grain and the grain boundary the crack is impeded. In order to compensate for this incompatibility a part of the grain boundary has to rupture, otherwise the sample would still be connected at the grain boundary and the crack could not open. The rupture needs the accumulation of plasticity which slows the crack down before the grain boundary. The amount of ruptured surface can be minimized by the formation of a corrugated fracture surface in the second grain, that is composed of two alternating slip planes. Since a corrugated fracture surface involves a higher energetic cost compared to its flat equivalent the crack advances correspondingly slower.

2.2 Definitions of Short Fatigue Cracks

The classification introduced by Suresh and Ritchie in 1984 [Suresh and Ritchie, 1984] finds a wide acceptance[1]: Fatigue cracks are "microstructurally short" when their size is comparable to the scale of a characteristic microstructural dimension (CMD), which is usually the grain size[2]. They are "mechanically short" when the size of the ZPD is at the scale of the crack size. They are "physically short" when the crack is long compared to the ZPD and the CMD but the crack's absolute size is not more than about 1-2 mm. According to Krupp [Krupp, 2007] the influence of the microstructure is high for microstructurally short cracks and little for mechanically and physically SFCs. The laws of LEFM can be applied to physically SFCs and LFCs but not to microstructurally or mechanically short cracks because in the latter two cases the material can't be considered as continuum what means that the ΔK concept is not applicable [Krupp, 2007].

[1] But there is no unified definition for SFCs. The American Society for Testing and Materials (ASTM) for example defines short cracks not according to the growth mechanism, nor to the possibility to predict the growth rate but simply according to its size: a crack is short as long as its zone of plastic deformation (ZPD) is larger than 1/50 of the crack length [Krupp, 2007].

[2] It can also be the size of a second phase, e.g. in α/β Ti alloys or in duplex steel

2.3 Classification of Fatigue Growth Stages

Growth stages and their corresponding growth mechanisms of fatigue cracks are classified differently by different authors. The following section reviews the descriptions given in three recent textbooks by Suresh [Suresh, 2003], Davidson et. al [Davidson et al., 2003] and Krupp [Krupp, 2007] in order to give an impression of how the fatigue phenomena occurring during the different growth stages can be defined.

According to Suresh, stage I growth[3], happens when both, the zone of plastic deformation at the crack tip, and the crack itself are confined to a few grain diameters. He assigns stage I growth to the near-threshold growth regime, describes the fracture surface as serrated / faceted and the crack growth mechanism as single shear in direction of the primary slip system, leading to a zig-zag path. Stage II growth [Forsyth, 1962] is described by Suresh as happening when the zone of plastic deformation around the crack tip encompasses many grains. During this stage the crack grows according to the Paris law, the fracture surface is planar with "striations" (ripples) [Zappfe and Worden, 1951] and the crack propagates normal to the tensile axis. The striations are perpendicular to the local crack growth direction and the spacing between them corresponds to the crack advance during one cycle.

As an explanation for the ripple formation Suresh refers to the model of plastic blunting / re-sharpening by Laird [Laird and Thomas, 1967] (figure 2.3) in the case of a wide variety of ductile materials, or the coarse slip (double slip) model by Neumann [Neumann, 1969] (figure 2.4) in the case of ductile metal single crystals.

Krupp [Krupp, 2007] classifies the growth stages of SFCs differently from Suresh by subdividing stage I in stage Ia (single slip) and Ib (double slip). The main difference is that Krupp distinguishes between the period of the corrugated pattern arising from double slip on two alternating slip planes (stage Ib) and the period of the striations arising from the plastic blunting / resharpening crack growth mechanism of Laird [Laird and Smith, 1962]. The crack propagation in stage Ib and II may appear similar but the period of the corrugated pattern in the first case is not directly coupled to the growth rate, while in the latter case one inter-striation distance corresponds to the crack propagation during one loading cycle. According to Krupp stage Ib crack growth is a matter of cyclic slip, dislocation pile-up and work hardening in alternate manner on multiple slip systems. The facets of slip band cracks are never perfectly flat since the crack is driven by cyclic plasticity on parallel slip planes but rather exhibit small slip steps or traces of intersections with secondary slip systems. The change from Ia to Ib happens when the crack tip reaches a grain which slip planes are unfavorably oriented with respect to applied stress states for the crack to propagate in single slip. In such cases the crack tends to continue its propagation perpendicular to the remote loading direction under operation of alternate slip systems. Krupp reports that the crack propagation can switch back and forth between Ia and Ib and states that the Neumann model can be relevant for both, stage Ib and II. He explains the crystallographic crack growth during stage Ia and Ib by the model of Wilkinson [Wilkinson et al., 1998] which

[3]The terms stage I and stage II have been first proposed by Forsyth [Forsyth, 1962]

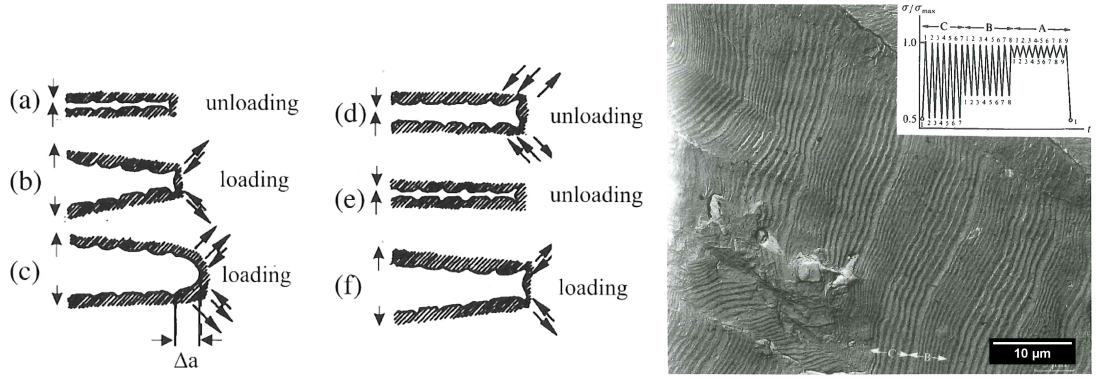

(a) (b)

Figure 2.3: (a) Plastic blunting / resharpening growth mechanism according to Laird [Laird and Smith, 1962]): The maximum shear stress during loading occurs on planes inclined at 60° with respect to the loading axis. Plastic deformation occurs on these planes during loading and causes blunting of the crack tip which is not reversible during unloading/compression. During the next loading cycle the crack tip resharpens, which causes the crack to advance. In one loading and unloading cycle one striation is formed. (b) Striations on fracture surface caused by stage II crack growth [McMillian and Pelloux, 1967].

is based on dislocation annihilation in front of the crack tip.

According to Krupp stage II growth happens due to a high stress concentration at 60° of the crack tip with respect to the loading axis that activates many independent slip systems with the result that the plastic deformation is "smeared" and is no longer dependent on local crystallographic orientation.

Finally, Davidson [Davidson et al., 2003] argues that in industrial alloys cracks usually initiate in stage II anyway. He briefly describes stage I as growth of small cracks in the region near the nucleation site in pure metals and some single-phase polycrystalline alloys where the crack grows at an angle while stage II is characterized by a growth more perpendicular to the stress axis. Davidson characterizes "short-crack behavior" by the growth rate and not by the crack length or the mechanism: short-crack behavior is observed when crack growth occurs below ΔK_{th} or when the growth rates are above the extrapolation of the Paris law.

2.4 The Slip Character

The slip character is a material-specific parameter that describes what kind of 3D dislocation arrangement forms during fatigue [Christ, 1991]. The two extremes of slip characters are planar slip and wavy slip, meaning that the dislocations form groups that stay on their slip plane or that they form, depending on the plastic strain amplitude $\Delta\epsilon_{pl}$ form complicated 3D arrangements like, dipoles, dipole-bundles, persistent slip bands

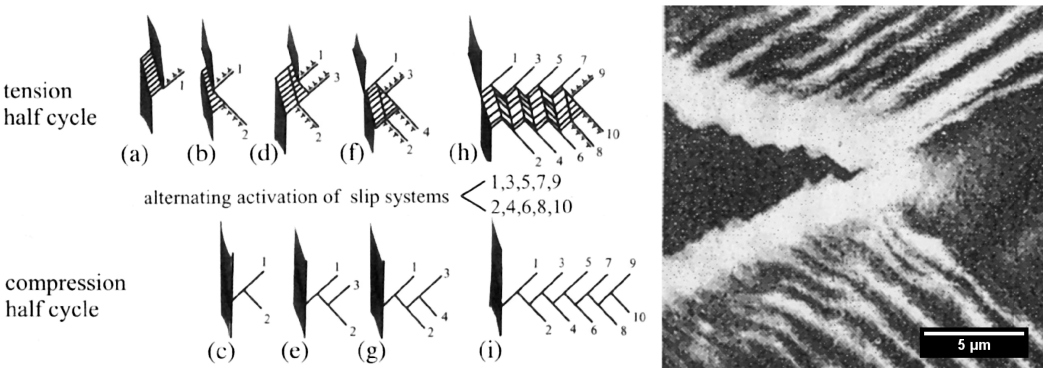

(a) (b)

Figure 2.4: (a) Scheme of double slip mechanism according to Neumann [Neumann, 1969]. During fatigue, dislocations emanate from the crack tip on the slip plane on which the crack is propagating. Their pile-up at obstacles causes a stress-field that acts against the emission of new dislocations. With increasing crack length the crack has increasing difficulties to continue on the same slip plane until it is eventually easier to continue on another slip plane even if it is less activated. (b) Scanning electron microscope (SEM) observation done by Vehoff [Vehoff and Neumann, 1987] on single crystals.

or cell structures, respectively [Feltner and Laird, 1968; Lukáš and Klesnil, 1972]. The slip character might be a mesoscale material characteristic but it has great influence on the macroscopic scale. Stage I crack growth can be observed in most metallic materials during the early stage of low-stress fatigue but it is particularly pronounced in alloys with planar slip character [Tanaka and Mura, 1984]. This point is of importance since the slip character influences greatly the measured patterns of this study.

Influence of the Stacking Fault Energy The stacking fault energy once was assumed to be the key factor influencing the slip character. It was argued that in order that dislocations can form 3D arrangements they must be able to leave their slip plane. Screw dislocations can do so via a process called cross-slip. But since they are split up into pairs of partial dislocations, separated by a stacking fault, they must recombine first to be able to leave their plane. The split up distance d is given by the equilibrium of attractive and repellent forces within a pair of partial dislocations. They repel each other due to their stress fields, whilst there is an attractive driving force trying to minimize the stacking fault area between them:

$$d = \frac{Gb^2}{4\pi\gamma_{SF}}, \tag{2.1}$$

where G is the shear modulus, b is the Burgers vector and γ_{SF} the stacking fault energy. The energy needed for recombination increases with increasing d which means that the

higher γ_{SF}, the easier the cross-slip and the more pronounced the wavy-slip behavior. However, systematic experiments showed that only in the case of pure metals are γ_{SF} and slip character linked in such a straight-forward way [Gerold and Karnthaler, 1989].

Influence of Short-range Order According to Gerold and Karnthaler [Gerold and Karnthaler, 1989] the existence of a short-range order or short-range decomposition processes is of much greater importance for the slip character than γ_{SF}. Wavy slip behavior can be often seen in materials without short-range order, planar slip in materials with short-range order, for example in materials containing small precipitates.

Christ [Christ, 1991] links the occurrence of a short-range order to a planar slip character in the following way: The first dislocation moving through destroys the short range order. The next dislocation cannot recreate the original condition since the short-range order does not have a periodicity of a whole-number multiple of the Burger's vector. Since the short-range ordered condition is energetically favored the first dislocation must overcome a strong resistance to move. The necessary local stress can be reached by dislocation pile-up. For all following dislocations it is easier to remain on the same plane. A short-range order thus localizes the plastic deformation and causes a planar slip behavior. This is valid for screw as well as for edge dislocations. Cross-slip also occurs in materials with planar slip character but cross-slipping screw-dislocations propagate in as identically confined manner like the edge dislocations. However, in materials with wavy slip character the dislocations can slip/cross-slip relatively independent from one another and tend to distribute in 3D on different slip planes.

In the case that the planar slip character is due to precipitates they must have a certain size, hardness and distance from one another in order for pronounced planar slip to occur. A few very small or soft precipitates are easily cut and represent no real obstacle to the dislocations. If the precipitates are big but far enough apart to be surrounded by Orowan loops [Hirsch and Humphreys, 1969], as it is typical for over aged alloys, they will not cause planar slip. The most effective precipitates for planar slip to be promoted are small enough to still be coherent, numerous and harder than the matrix (typical for peak-aged alloys).

2.5 History of Short Fatigue Crack Characterization

Since the pioneering work of Pearson [Pearson, 1975] in the seventies, numerous authors have studied the growth of SFCs in a wide variety of metallic materials. This topic has been the subject of review papers and conferences [Ritchie and Lankford, 1986; Miller and de los Rios, 1992; Ravichandran et al., 1999]. One common trend shown by this large body of work is that SFC growth rates show a very large scatter [Hertzberg, 1995]. Several authors, have suggested that this scatter can be partly explained by the 3D growth of SFCs which are in contact with only a few grains (typically between 1 to 5 grains) [Pineau, 1986; Ravichandran and Li, 2000; Newman, 1998]. The orientation and shape of those grains have a direct influence on the local stress field [Pommier, 2002]. This in turn, influences the direction and rate of the local crack growth via the

activation of slip systems and local plasticity. Therefore, an exhaustive analysis of SFCs would require information on grain shape, grain orientation and crack propagation rate in 3D.

Since the first observations of SFC at the surface of Al fatigue samples by optical microscopy [Pearson, 1975], more sophisticated techniques involving beach marking using ink [Verreman and Nie, 1996] or changes in environment [Nadot et al., 1997], serial polishing [Clément et al., 1984], FIB milling [Holzapfel et al., 2007] and synchrotron micro tomography [Ludwig et al., 2003; Ferrié et al., 2005] have been used to study the relationship between local microstructure and the 3D growth of SFCs . All these techniques have merits and disadvantages. Beach marking, for example, has a limited spatial resolution and the method used to mark crack fronts can potentially have an influence on crack growth. Serial polishing provides a higher spatial resolution. The series of 2D micrographs used to reconstruct 3D images of short cracks can be obtained by mechanical milling or by focused ion beam (FIB) machining [Zaefferer et al., 2008; Schäf et al., 2011]. In the last case, very high spatial resolution can be obtained allowing the study of fine details of the fracture surface, but the maximum volume that can currently be observed is about 100x30x30 μm^3, impeding, for example, the study of a full crack front even in the case of short cracks. Another obvious disadvantage is that those techniques are destructive and can only provide post mortem information.

Synchrotron radiation X-ray microtomography is a non destructive 3D imaging technique and can be used to circumvent this problem. The technique provides a spatial resolution comparable to optical microscopy (voxel sizes of about 1 micrometer) and the use of phase sensitive imaging modes enables the detection of cracks with submicrometer opening displacements. The evolution of the 3D shape of growing cracks can be obtained in (interrupted) in-situ experiments. However, this technique does not provide information on the local grain microstructure along the crack fronts. Grain boundaries can be visualized in some specific material systems via decoration techniques [Ludwig et al., 2003, 2009a] but even in such cases PCT lacks information on the crystallographic orientations of grains which determines the local stress state, plasticity and hence the crack growth.

The correlation between local plastic activity and the growth of SFC was first investigated via 2D surface observations using electron diffraction techniques such as electron channeling contrast [Zhang and Edwards, 1992] and electron back scattering diffraction (EBSD) [Wilkinson et al., 1996; Taylor et al., 1999]. By coupling PCT and EBSD maps obtained post mortem it has recently become possible to correlate the growth of a SFC with the local microstructure of an α/β Ti alloy [Birosca et al., 2009]. The experimental task is however challenging as the EBSD maps are obtained by manual serial polishing, leading to a rather large distances between them. Automated serial polishing [Spowart, 2006] can be used to obtain serial EBSD maps which provide an accurate 3D description of polycrystalline aggregates (accuracy in vertical slice separation is typically 1-2 μm) containing typically several thousand grains. However, this technique has not been used with cracked samples so far. It is likely that the presence of a plastic zone around the crack, the tendency of the crack to be closed by abraded material and

the break-out of loose pieces of material parts during serial-polishing will remain an issue. To avoid these problems, crystallographic characterization should be carried out prior to the fatigue experiment using a non destructive technique. This can be achieved thanks to the development of diffraction-based synchrotron imaging techniques such as "three dimensional X-ray diffraction microscopy" (3DXRD) [Poulsen, 2004] and "X-ray diffraction contrast tomography" (DCT) [Johnson et al., 2008; Ludwig et al., 2009b] which are capable of measuring non-destructively 3D grain shape and orientation in many polycrystalline material systems.

The approach used here combines two characterization techniques. DCT is used to measure the 3D microstructure (grain shape and orientation). PCT is used to measure the 3D crack shape. By measuring the crack shape at different numbers of fatigue cycles the 3D crack evolution can be accessed. Thereby all crucial information on SFC propagation can be gathered which wouldn't be possible using 2D surface microscopy techniques. When using 2D techniques the crack propagation can be followed on the surface, missing the 3D aspect of the crack and the microstructure. And even if it were properly possible to characterize a cracked sample using alternately EBSD and polishing, only a single crack propagation stage could be measured, missing out on the aspect of crack evolution. The combination of PCT and DCT gives access to 3D SFC evolution and its surrounding 3D microstructure which was never possible before.

3DXTSM A new discipline that investigates the 3D interaction of short fatigue cracks with their surrounding microstructure is evolving [Schäf et al., 2011; Herbig et al., 2011]. In order to delimit the method described in this work from others we introduce a definition. We call this method "3-Dimensional X-ray Tomography of Short cracks and Microstructure" (3DXTSM) and define it as all approaches that characterize a short crack and the shape and orientation of its surrounding grains in 3D using X-rays. By using the expression "X-rays" a clear line between methods based on EBSD and FIB or EBSD and serial polishing is drawn. Such a delimitation makes sense since those methods are destructive, can only characterize relatively small volumes, but have a higher spatial resolution. Using the general expression "X-rays" leaves space for the choice and evolution of the X-ray methods being used. Fatigue is not mentioned since also other types of cracks could be investigated using the method. Also expressions like "propagation" or "time-resolved" are neglected because that way the definition also covers experiments that characterize the crack only at a single point of time. The definition leaves entirely freedom on how the data is processed, analyzed or visualized.

Chapter 3

Materials and Methods

3.1 Introduction to Titanium

3.1.1 Titanium in general

Although there are only two primary phases of titanium alloys, a hexagonal close packed (hcp) α phase, stable at low temperatures and a body centered cubic (bcc) β phase, stable at high temperatures, the literature describes many more, depending on alloying contents, orientation relations, precipitation state and thermomechanical processing. The following paragraph summarizes the expressions used in the literature [Welsch et al., 1994] and thereby defines the terms used for this work. For reasons of completeness all phases are listed although for this work mainly primary β, secondary α, α" and ω_{ath} are of importance.

Primary $\boldsymbol{\alpha}$ is the bulk α phase that forms during the first heat treatment at high temperature and persists during heat treatments in the $\alpha - \beta$ field.

Secondary $\boldsymbol{\alpha}$ is the lamellar α phase that forms by diffusion during annealing.

$\boldsymbol{\alpha}$' and $\boldsymbol{\alpha}$" form by a martensitic phase transformation. α' is a hexagonal distorted phase that forms in alloys with a low concentration of β-stabilizing elements during rapid cooling (thermal martensite). α" is an orthorhombic phase that forms in alloys with an intermediate concentration of β-stabilizing elements (e.g. Mo, V, Ta, Nb). The phase transformation can occur during rapid cooling or stress/strain induced (stress/strain induced martensitic transformation, SIMT)) according to the reaction $\beta \rightarrow \alpha'' + \beta_{twinned}$. The orientation relation between β and α" is: $(110)_\beta // (002)_{\alpha''}, [111]_\beta // [110]_{\alpha''}$.

$\boldsymbol{\alpha_2}$ refers to α phase containing Ti_3Al precipitates.

Type 1 $\boldsymbol{\alpha}$ and **type 2 $\boldsymbol{\alpha}$** is an additional classification that generally splits up all α phases that formed during aging of β into two groups. Between β and type 1 α there is Burgers orientation relation, between β and type 2 α there is not.

ω_{ath} and ω_{iso} are trigonal transition phases between β and α. The transition phases form at low temperatures in alloys containing β-stabilizing elements because those elements slow down the α formation [Clément et al., 2007]. The coherent athermal ω phase forms during rapid cooling by a martensitic process and has a size of 2-4 nm. The isothermal ω phase forms at constant temperatures from ω_{ath} seeds by a diffusion controlled process. Both ω phases have same orientation relation with the β matrix: $(11\bar{2}0)_\omega//(110)_\beta, < 0001 > \omega// < 111 > \beta$ [Murakami, 1980]. A typical value for the ω particle density is $10^{18}/\mathrm{cm}^3$ [Duerig et al., 1980a].

β' refers to a solute lean β phase that remains after solutes have diffused into a neighboring phase during annealing.

Primary β is the bulk β phase that nucleates from melt or forms during the first heat treatment at high temperature and persists during heat treatments in the $\alpha - \beta$ field.

Pure titanium has an extreme chemical affinity to oxygen, nitrogen and hydrogen which dissolve rapidly above ca. 400 °C [Dunand, 2004]. Once those gases are dissolved in titanium they can only be removed by remelting under vacuum. The solubility of oxygen in titanium is 33 at. % and the oxygen partial pressure above which titanium absorbs oxygen as low as $3{\cdot}10^{-19}$ bar [Heinl et al., 2007]. Oxygen and nitrogen stabilize the α phase that is already hard and brittle and further increase, being interstitially dissolved, its hardness and brittleness [Zwicker, 1974]. Hydrogen causes embrittlement due to stress induced formation of brittle hydride phases and their subsequent "cleavage" fracture [Eliezer et al., 2005]. The chemical affinity of titanium to some atmospheric gases can be reduced by adding certain alloying elements. Nevertheless, heat treatments of titanium and its alloys above a certain temperature must be performed in a controlled atmosphere.

3.1.2 Beta Titanium Alloys

β titanium alloys are defined as alloys that keep their β structure upon quenching from the high temperature β field because they contain enough β-stabilizing elements to avoid the formation of martensite [Weiss and Semiatin, 1998]. These alloys are subclassified into stable β (also called near β) , metastable β, and β-rich α/β alloys, depending on the amount of β-stabilizing elements (figure 3.1). The metastable β titanium alloys carry their name from the fact that after quenching to room temperature they are not at the thermodynamic equilibrium. That is why SIMT is an issue in these alloys. β titanium alloys offer a broad versatility with respect to processing, microstructure, and mechanical properties. Their bcc structure offers several advantages compared to α/β alloys: an increased heat treatability, a wide range of strength-to-weight ratios, a deep hardening potential and a high ductility. Additionally their fatigue resistance is superior to that of α/β alloys [Weiss and Semiatin, 1998]. Nevertheless the α/β alloys are used more often because of the increased density, the smaller processing window and the higher costs of β alloys [Leyens and Peters, 2003]. In this work two different β titanium

alloys were used: Beta21S and VST55531. Their main characteristics are recalled in the next paragraph.

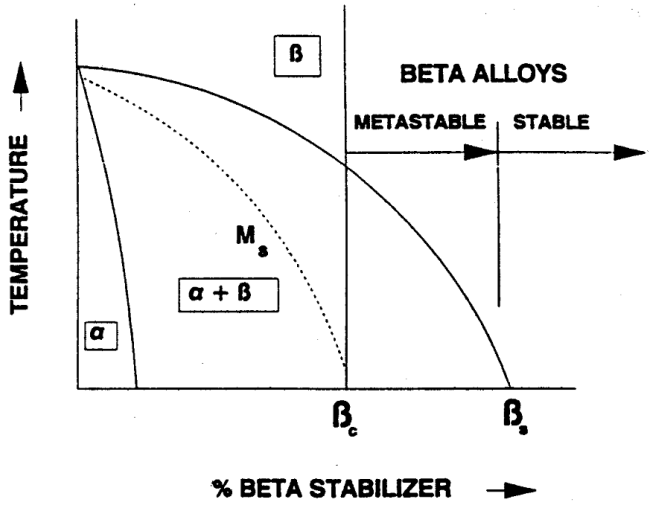

Figure 3.1: Pseudobinary phase diagram of titanium and a beta stabilizer [Bania, 1994].

Beta21S Beta21S or TIMETAL®21S with the chemical composition Ti-15Mo-3Nb-3Al-0.2Si is a metastable β titanium alloy that was introduced in 1989 and designed for elevated temperature strength, creep resistance, good cold formability, good oxidation resistance and thermal stability for applications up to 593°C [Weiss and Semiatin, 1998; Welsch et al., 1994; Timet, 2010]. Its β transus temperature T_β (transformation temperature between α and β,)is 807 °C. The α phase can be solutionized at 816-843°C at solution times between 3-30 minutes. The alloy is normally aged for 8-16 hours at 510-691°C which results in a microstructure composed of a β matrix with α precipitates. A corresponding semi-quantitative time-temperature-transition diagram is shown in figure 3.2. The 0.2% yield strength for strips and sheets is 759-931 MPa for the air-cooled, unaged alloy condition and reaches a maximum of 1013 MPa at the peak-aged condition [Timet, 2010]. Fatigue data for Beta21S show a crack propagation behavior comparable to other β titanium alloys (such as Ti-10V-2Fe-3Al) [Weiss and Semiatin, 1998; Terlinde and Fischer, 1996] and also show negligible influence of the heat treatment on the fatigue growth rate [Fanning, 1993].

VST55531 Only very little is known about the alloy VST55531 (composition Ti-5.5Al-5V-5Mo-3Cr-1Zr) produced by the VSMPO-AVISMA corporation and used in this study. The β transus temperature T_β is 803 °C. Fifteen minutes at 843 °C solutionizes all traces of alpha phase and results in a grain size of approximately 100 μm (unpublished data by Fernando Warchomicka, Technical University of Vienna). A very similar alloy TIMETAL 5553 [Fanning, 2005], which is also called TIMETAL 555, (Ti-5Al-5Mo-5V-3Cr-0.5Fe) produced by the Timet company contains ω_{ath} precipitates in the solutionized and quenched condition [Nag, 2008].

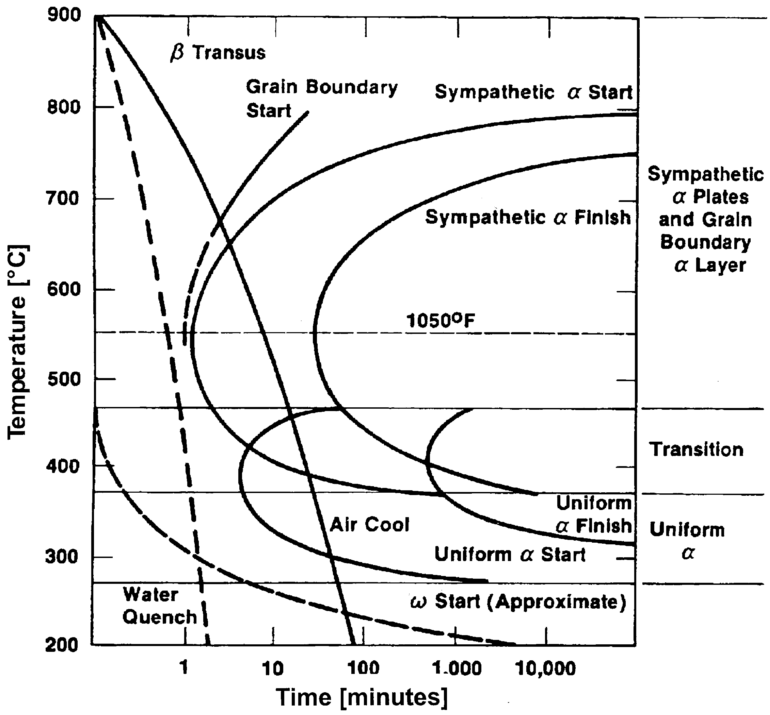

Figure 3.2: Time-temperature-transition (TTT) diagram of metastable β titanium alloy Ti-10V-2Fe-3Al [Duerig et al., 1980b; Terlinde and Fischer, 1996]. For near β titanium alloys all α regions would be shifted to the lower right part of the diagram.

Beta21S offers a mechanism with which grain boundaries can be made visible in PCT [Dey et al., 2007]. The formation of α precipitates is triggered by lattice defects like plastic deformation, impurities (e.g. nitrogen, oxygen or hydrogen) or grain boundaries. A heat treatment of an undeformed titanium sample without impurities just below T_β will result in layer-like α precipitates along the grain boundaries (see figure 3.2), the so called grain boundary α [Chesnutt and Froes, 1977] (see figure 3.3). For the best possible decoration of the grain boundaries with α phase the temperature must be just above the sympathetic alpha start temperature (see figure 3.2). Beta21S contains Al and Mo. Since Al is an α stabilizer and Mo is a β stabilizer they migrate into the α and β phase, respectively during the diffusion controlled formation of grain boundary α. PCT is sensitive enough to reveal such fine electron density differences what makes it possible to detect the 3D grain boundary position.

Metallographic Preparation The high ductility of titanium alloys causes scratches when being polished with diamond pastes that can't easily be removed again. When using very fine grinding paper the abrasive particles get imprinted into the surface (inclusions). Around those particles form holes that fill with abraded material during polishing. That causes comet-like artifacts (black dots with equiaxed tails) in the polished

surface. Therefore, no finer grades than 1200 grinding paper can be used for titanium and a long chemical-mechanical polishing step must follow. Chemical-mechanical polishing is usually done by using a mixture of H_2O_2 and fine SiO_2 particles. While H_2O_2 oxidizes titanium the SiO_2 particles continuously remove the oxide layer. Due to its production process titanium is very clean. All dark dots visible on the surface using an optical microscope are inclusions [Welsch et al., 1994; Taylor and Weidmann, 2008]. Those artifacts can be reduced by rotating the sample in big circles against the sense of rotation of the polishing disk.

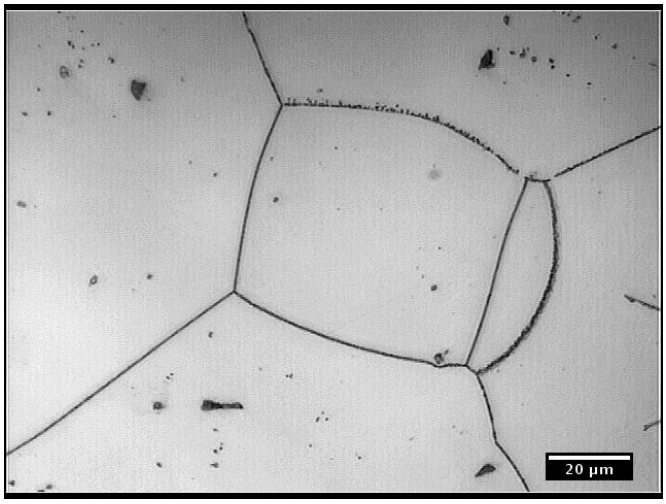

Figure 3.3: Light optical micrograph of a polished and etched cross-section through Beta21S after 1 hour at 790°C. Layer-like α precipitates are visible along the grain boundaries. The dark dots inside the grains are mostly inclusions.

3.2 As-received Materials

Beta21S was received as rolled, 1.6 mm thick sheet with an initial grain size of 20-30 μm. VST55531 was received as a forged bar of 12.7 cm x 3.75 cm that was heat-treated for 2 hours at 773 °C and air cooled.

3.3 Samples

Overview Altogether four Beta21S and two VST55531 samples were used in this study (table 3.1). All Beta21S samples were solution annealed for 2 hours at 850 °C and quenched in water. Both VST55531 samples were solution annealed for 2 hours at 843 °C and air cooled. This solution heat treatment resulted in a mean grain size of 55 μm and 65 μm in the case of Beta21S and VST55531, respectively. All heat treatments required encapsulation. 3DXTSM experiments were carried out to investigate the crack growth in 3D. The crack morphology at the surface of flat samples was investigated

Material	Experiment	Shape
VST55531	3DXTSM	cylindrical, bone-shaped
	SEM, EBSD, FESEM	flat, bone-shaped
Beta21S	3DXTSM, DCT evaluation	cylindrical, bone-shaped
	SEM, EBSD, FESEM	flat, bone-shaped
	XRD	cylindrical, bone-shaped
	IXS	thin foil

Table 3.1: Summary of all samples used for this study.

using a Scanning Electron Microspcope (SEM) and a Field Emission Scanning Electron Microscope (FESEM). Using Electron Back Scattering Diffraction (EBSD) and X-Ray Diffraction (XRD) the occurence of Stress-Induced Martensitic Transformation (SIMT) was investigated on the surface and in the bulk, respectively. The elastic constants of Beta21S were measured on a thin foil using Inelastic X-ray Scattering (IXS). The following paragraphs describes which preparation steps each samples received. The preparation steps themselves are detailed in the next section.

3DXTSM and XRD Samples The samples were spark erosion cut to a bone-shaped fatigue sample with a cylindrical gage section of 0.7 mm diameter as seen in figure 3.4a. The samples were polished because spark erosion leaves a rough surface with highly deformed grains, problematic for inspection with DCT. After polishing the diameters of the Beta21S and the VST55531 sample were ≈600 μm and ≈350 μm, respectively. A wedge-shaped notch (150 μm wide, 2 μm high and 40 μm deep) was inserted in the sample gage length using focused ion beam machining in order to localize crack initiation as described in Ferrié et al. [Ferrié et al., 2006]. After performing the 3DXTSM experiment the Beta21S sample was heat treated for 24 hours at 790 °C in order make the grain boundaries visible in PCT.

SEM, EBSD and FESEM Samples The samples were spark erosion cut to a bone-shaped fatigue sample with a square cross section in the center part of 600 μm edge length as shown in figure 3.4b. After grinding and polishing one side the sample thickness was 400 μm.

IXS Sample The preparation of this Beta21S sample was challenging and is given in more detail in the attachment.

3.4 Sample Preparation Techniques

Encapsulation When dealing with small samples it is especially important that during the heat treatment no atmospheric gases, in particular oxygen and nitrogen, are present. A certain effort is involved with avoiding this scenario. Prior to encapsulation

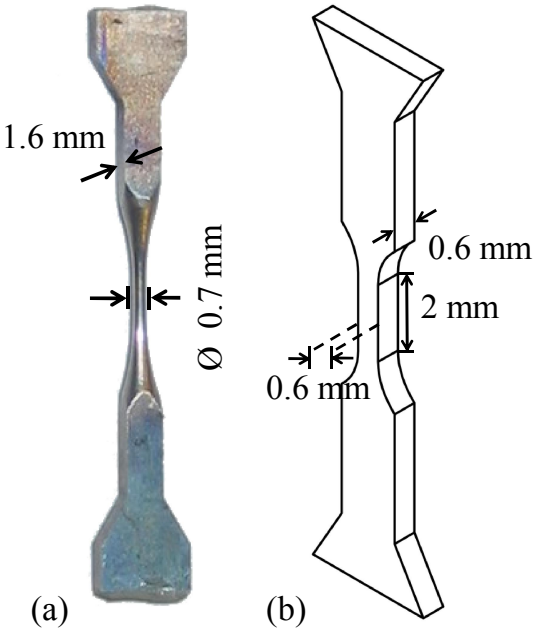

Figure 3.4: (a) Round bone-shaped fatigue sample and (b) flat bone-shaped fatigue sample after spark erosion.

the samples were wrapped in tantalum foil (99.9 % purity, 0.03 mm thickness, Good-Fellow, UK) that absorbs residual atmospheric gases in the carefully evacuated quarz tube. The samples were encapsulated in quartz tubes (Ilmasil PN, QSIL AG, Germany) with an inner diameter of 1.2 cm and an outer diameter of 1.5 cm using a blow torch. The encapsulation procedure involved several alternations of rinsing with argon (Ar) and evacuation.

The tube was closed on one side. After inserting the wrapped sample the tube was reduced to about 1 cm outer diameter about 5 cm away from the sample position. The quartz tube was attached to a vacuum system consisting of primary and secondary pump (Pascal, Alcatel, France) using adapter fittings (SD KF adapters, Swagelok, Sweden) with teflon washers. The quartz tube and the tube connected to the Ar bottle were evacuated down to about 10^{-3} mbar and left at this pressure for 10 minutes. Then the tube was filled up to atmospheric pressure with high purity Ar gas (RT Argon UHP X50S, Airproducts, France). The quartz tube was evacuated again and then gently heated with the blow torch to about 100 °C to facilitate the desorption of molecules adsorbed on the surface. After rinsing with Ar a second time and evacuating a third time the tube was sealed under vacuum at the position of reduced diameter.

Heat Treatment The heat treatment was carried out in the furnace L3S manufactured by the Nabertherm company, Germany. The heat treated titanium sheets were never bigger than 10 mm x 20 mm x 1.6 mm, so the rates of air cooling and quenching with water at room temperature were correspondingly high. In both cases the quarz tubes were opened only after the samples reached room temperature.

Spark Erosion All fatigue samples were machined by spark erosion, the cylindrical ones by VASA tools, Roskilde, Denmark, the rectangular ones by Ateliers Peyronnard, Champ-sur-Drac, France.

Embedding The samples were embedded in the resin Mecaprex MA2 (Presi, Brié-et-Angonnes, France).

Grinding The samples were ground consecutively with 320, 800 and 1200 silicon carbide (SiC) grinding paper. Between each step the grinding machine and the sample were cleaned from remaining grinding particles in an ultrasonic bath.

Polishing Two types of polishing were performed. The fatigue samples with the cylindrical gage region were polished by hand first using 2400 grit SiC paper and then by holding them to a rotating felt disc that was soaked with a suspension containing 17 μm SiC particles. The polishing of all samples with flat surfaces was done for 45 minutes using an OP-S suspension (commercial colloidal silica suspension) compatible polishing cloth (NT, Presi). As polishing reagent a mixture of 90 vol% OP-S suspension (Struers) and 10 vol% H_2O_2 (30 % solution) was added dropwise.

Focused-Ion Beam Machining The FIB notches were machined with Ga-ions by STMicroelectronics, Crolles, France and Université Libre de Bruxelles, Service Matières et Matériaux, Brussels, Belgium respectively, at a current of 9 nA and a tension of 30 kV.

Etching Etching was carried out during 45 seconds using Kroll's reagent: 17 ml distilled H_2O, 0.9 ml HNO_3 (65%) 0.5 ml HF (40%) and a few drops of H_2O_2 [Petzow, 1978; Leyens and Peters, 2003].

Sample Extraction The samples were extracted from the resin by letting it swell for several minutes in acetone. The resin residues were cleaned from samples of up to 500 μm thickness using an ultrasonic bath. At these thicknesses there is no risk of plastic deformation by oscillation of the sample at its resonance frequency in the bath. Small acetone islands after drying can be avoided by a subsequent cleaning step with alcohol.

3.5 3DXTSM

3.5.1 Introduction to Synchrotron Imaging Experiments

Synchrotrons accelerate charged particles (typically electrons or positrons) using synchronized magnetic fields. The particle beam is injected into the so-called storage ring, where it is forced on a closed trajectory and where it is used to produce a continuous spectrum of intense electromagnetic radiation, called synchrotron radiation. The flux and brilliance of electromagnetic radiation obtained with such particle accelerators

is many magnitudes higher than what can be produced with any laboratory source. For most experiments this means drastically shorter measurement times or accordingly drastically increased accuracy since even if the beam is highly monochromatized still enough flux is present for the experiment.

In practice, the charges are pre-accelerated in a linear accelerator, followed by acceleration close to the speed of light in the so-called booster synchrotron and finally inserted into a storage "ring". The latter is, on closer examination, a polygon with a bending magnet (BM) on each polygon corner. The magnetic fields of the BMs change the propagation direction by a few degrees (accelerate the particles into a different direction). Since accelerated electric charges emit electromagnetic radiation [Jackson, 1999] at each bending magnet synchrotron radiation is emitted with which experiments can be done. The X-ray emission results in an energy loss of the particle beam which is restored during passage of radiofrequency cavities along the beam trajectory.

A bending magnet bends the beam only once. More electromagnetic radiation can be obtained using insertion devices (ID) which consist of a series of strong magnets of alternating character. Those bend the beam several times in the straight sections between two BMs and coherent superposition of the wavefields from successive undulations can produce orders of magnitude higher intensity than BMs. The maximum energy of the charged particles is proportional to the diameter of the storage ring. The larger the storage ring the higher the maximum photon energies. Experiments with photon energies up to about 20 keV can be done at various national synchrotron sources. High energy photons are currently only available at a few, large synchrotron facilities worldwide (ESRF, APS, Spring 8, Petra III). Depending on the type of experiment the emitted electromagnetic radiation passes several optical elements like collimators, focussing optics, filters or monochromators. For the diffraction (DCT) and imaging experiments (PCT) described in this work, the beam is monochromatized by crystal or multilayer optics, respectively. The size of the beam is adjusted to the sample size and scattering background is reduced by two sets of slits. This preconditioned beam then arrives in the experimental hutch where it interacts with the sample that is mounted on a high precision sample stage having the rotational and translational degrees of freedom required for acquisition of tomographic scans. The experiment is operated by remote control from a control room, which is shielded from the electromagnetic radiation in the experimental hutch. The control electronics enables precise synchronization of camera exposure times during the scan acquisition procedure. A fast X-ray shutter blocks the beam during camera readout. Figure 3.5 schematically shows the setup of the imaging beamline ID19 at the ESRF where most of the experiments for this study were done. The sample-to-detector distance x is the distance between sample rotation axis and scintillator. For many experiments a monochromatic incoming beam is required. Monochromatization is achieved by crystal or multilayer optics, based on diffraction as described by Bragg's law

$$n\lambda = 2d\sin(\theta), \tag{3.1}$$

with n being an integer, λ the wavelength, d the inter-lattice spacing and θ the diffraction angle. For an incoming polychromatic beam hitting a single crystal at a certain angle

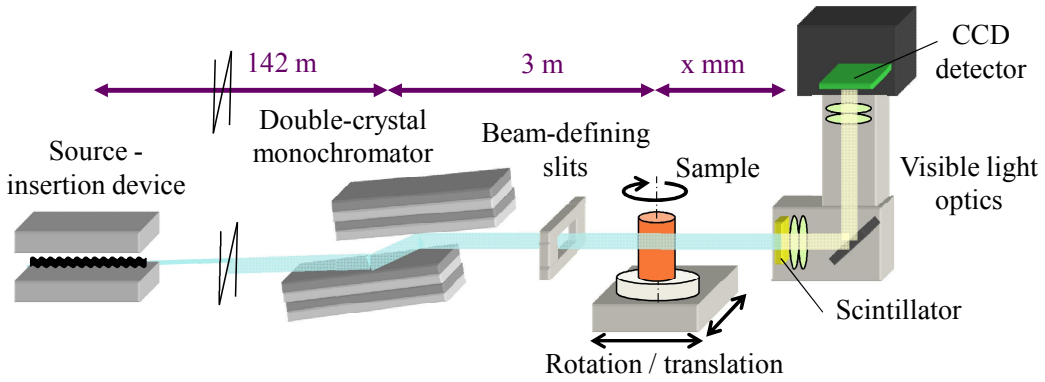

Figure 3.5: Principal components of the imaging beamline ID19 at the ESRF

only a certain wavelength and its whole-number multiples are diffracted. Two types of monochromators were used for this study: a Si 111 double crystal monochromator (Bragg case) and a (single bounce) multilayer monochromator. The Si double crystal monochromator yields a relatively high energy resolution $\Delta E/E$ of $1.4 \cdot 10^{-4}$, required for the diffraction experiments. However, a high $\Delta E/E$ of the monochromator means also that only a small fraction of the incoming spectrum is diffracted and the intensity available for the experiment is low. For conventional tomographic imaging experiments monochromaticity is less important than intensity. Multilayer monochromators are designed to fulfill those demands. They consist of a thin stack of about 100 layers of alternating high and low electron density materials (e.g. W / B_4C) deposited on the surface of a flat Si substrate. Those layers act on the incoming beam like a thin crystal with a lattice spacing equal to the periodicity of the multilayer (40 nm in our case). As described by the laws of kinematic diffraction, reducing the crystal thickness increases the acceptance (in terms of energy bandwidth and incidence angle). The multilayer monochromator used for high spatial resolution absorption and phase contrast imaging experiments at ID19 has an energy resolution of 10^{-2} and about 100 times more flux than the double crystal monochromator.

After the beam passed the sample it arrives on a transparent luminescent screen, a material which transforms X-rays into visible light [Martin and Koch, 2006]. The thicker the active layer of the screen, the higher the probability for a X-ray photon to be absorbed within it and therefore the higher is its light output. But during interaction with the material, the incoming X-ray photons will cause secondary radiation (electrons, X-rays) which scatters in random directions. The thicker the active layer of the screen, the higher is the probability that those events are captured inside the active layer and contribute to the creation of visible light photons at increasing distance from the point of incidence. This obviously leads to a loss of spatial resolution and hence a compromise between absorption efficiency and spatial resolution has to be accepted. Once produced by the scintillator the visible light image is magnified by conventional microscope optics and captured on a charge-coupled device (CCD) detector [Labiche et al., 2007]. Figure

3.5 shows the setup of the imaging beamline ID19 (the setup at the second beamline, ID11, used for this work is very similar). One of the differences is that ID19 is optimized for high lateral coherence of the beam, while ID11 is optimized for high energy photon flux.

3.5.2 Introduction to Tomography

Tomography is derived from the Greek words "tome" (section) and "graphein" (drawing, describing) and summarizes imaging techniques whose output is the inner structure of a 3D object, in form of a stack of slices. It is therefore also called cross-sectional imaging [Langer, 2008]. The two types of tomography used in this study (phase (PCT) and diffraction contrast tomography (DCT)), have a similar experimental setup (figures 3.9, 3.5) but exploit different contrast mechanisms. Both methods have in common that the sample is illuminated by an extended monochromatic synchrotron X-ray beam which is captured on a high resolution imaging detector behind the sample, that the sample is rotated while a set of radiographs is taken and that from those images the 3D sample volume is reconstructed by means of algebraic or arithmetic reconstruction techniques [Kak and Slaney, 2001].

Propagation Based Phase Contrast Tomography

Propagation Based Phase Contrast Tomography (PCT) exploits two contrast mechanism; the absorption and the phase shift of X-rays while they propagate through the sample. The absorption in governed by the line integral of the attenuation coefficient of the material and can be described by the Beer-Lambert law: $I = I_0\, exp\{-\int \alpha dx\}$, where I_0, I are the intensities of the incident, and transmitted beam, respectively, α is the attenuation coefficient and x the sample thickness. In order to perform Absorption Contrast Tomography (ACT) no particular X-ray beam requirements are needed. (Quantitative reconstruction of the attenuation coefficient requires a monochromatic beam [Baruchel et al., 2000]). However, PCT requires an incident beam with partially coherent wave properties. This can be achieved via the combination of a high energy resolution, a small X-ray source size and a long source to sample distance. In these conditions the incident beam can be approximated by a plane monochromatic wave. Where the refractive index of the material is higher the X-rays will propagate slower, this causes a phase shift of the transmitted beam and produces interference fringes at the boarder between areas of high and low refractive indices. As the detector is moved away from the sample, the fringes become more pronounced and wider. The contrast increases but at the same time the spatial resolution decreases (see figure 3.6). Phase contrast makes boarders between high and low electron density objects visible that aren't visible with ACT. For example the size of the smallest detectable hole in an up to 4 mm thick sample at 25 keV is about 20 μm using ACT and 0.05 μm using PCT [Cloetens, 1999]. For the current study this means that crack parts that are almost closed are only visible with PCT.

Although PCT has an additional contrast mechanism the principle of reconstructing

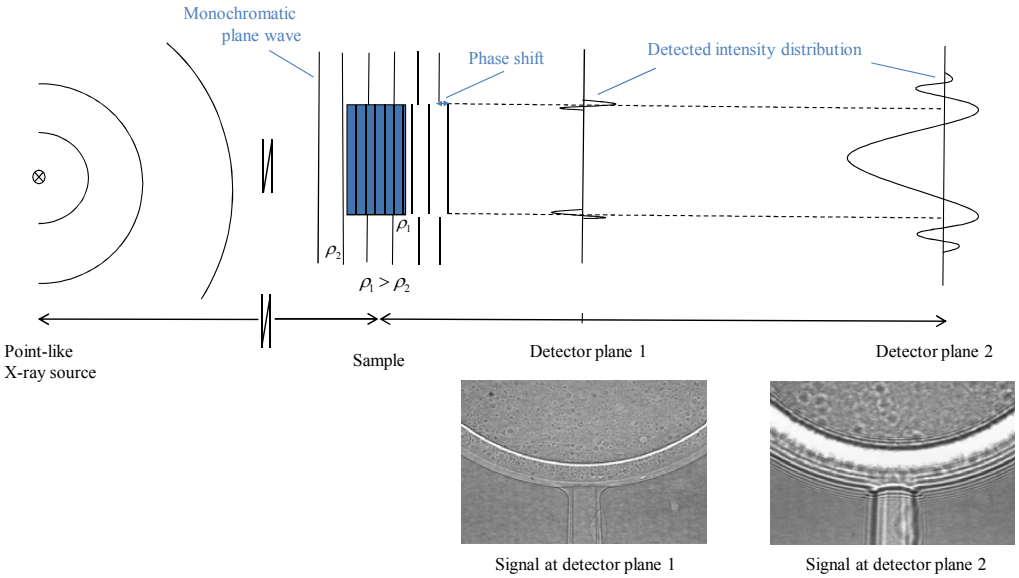

Figure 3.6: Propagation based phase contrast occurs due to the phase shift induced by the different propagation velocities in high and low electron density objects [Cloetens, 1999].

the PCT 3D volumes remains, at least for the case of moderate propagation distances (so-called "edge-detection regime"), the same as that of ACT [Cloetens et al., 1997]. The setup used for this study justifies the assumption of a parallel beam geometry which simplifies the 3D reconstruction to a series of 2D reconstructions. Each slice, that is each row of the detector, is reconstructed separately. As shown in figure 3.7 the intensity in a given point on the detector is equal to the sum of the image values along the ray that goes in beam direction and hits this pixel of the detector. By back-projecting the intensity profiles of a whole line of pixels on the detector along the direction of the incident beam and superimposing these back-projections, a slice can be reconstructed. The more projections are used the more precise becomes the reconstruction (figure 3.8a). A reconstruction approach called filtered back-projection [Kak and Slaney, 2001] is used to reconstruct the distribution of the X-ray attenuation coefficient inside the sample (figure 3.8b).

Diffraction Contrast Tomography

DCT is a synchrotron imaging technique based on Bragg diffraction of grains in a crystalline sample: when a single crystal is rotated in an extended monochromatic X-ray beam it will diffract every time it runs through Bragg diffraction alignment condition with the incoming beam. A detector, larger than the direct beam and closely mounted behind the sample, will capture a part of these diffraction events. In the transmitted beam the intensity diffracted out of the direct beam will be visible as a dark "extinction

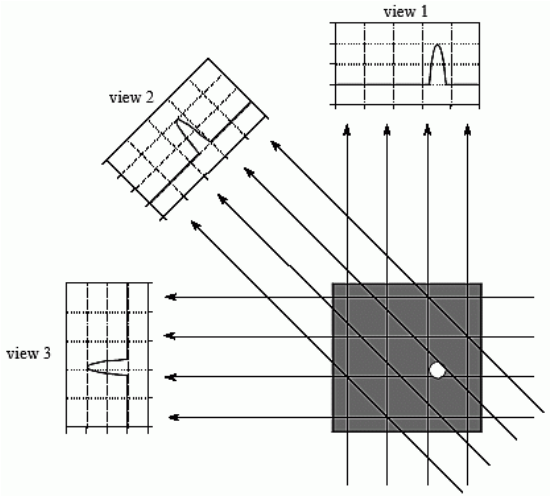

Figure 3.7: Acquisition of radiographs during a tomography experiment [Smith, 1997].

spot", and the diffracted beam forms a bright "diffraction spot". Assuming kinematical diffraction and negligible orientation and strain gradients within the grain, the intensity distribution inside the extinction and diffraction spots correspond to parallel projections of the 3D grain volume. From the shape and intensity distribution of the diffraction spots, the single crystal's 3D shape can be reconstructed using Algebraic Reconstruction Techniques (ART) [Gordon et al., 1970]. The orientation of the grain can be inferred from analysis of the diffraction vectors associated to the observed reflections. DCT applies this principle to polycrystals (figure 3.9) where an additional algorithm has to be used to identify which diffraction spots belong to which grain. The 3 main steps of the semi-automated sample reconstruction procedure from diffraction spots involve [Ludwig et al., 2009b]

- Spot matching: Friedel pairs of diffraction spots (hkl and $\bar{h}\bar{k}\bar{l}$ reflection) from the same grain, observed at sample rotation angles ω and $\omega + 180°$ are identified. Each spot pair determines a diffraction vector in the sample coordinate system.
- Indexing: the pairs of diffraction spots are sorted into sets belonging to the same grain. This is done by applying a combination of real space and crystallographic constraints.
- Reconstruction: the individual grain shapes are reconstructed using 3D ART and assembled into the common sample volume.

During reconstruction, each grain is assigned a grain number. The output of DCT is, first, a volume where all voxels belonging to one grain have the value of its grain number (grain map), second, a list relating each grain number to a crystallographic orientation and third, the "DCT absorption volume", reconstructed from the contrast in the center region of the DCT radiographs (figure 4.3).

The grain orientations are described in the form of Rodrigues vectors $\vec{r}$ [Rodrigues, 1840]. This vector representation of orientation space is a format commonly used for

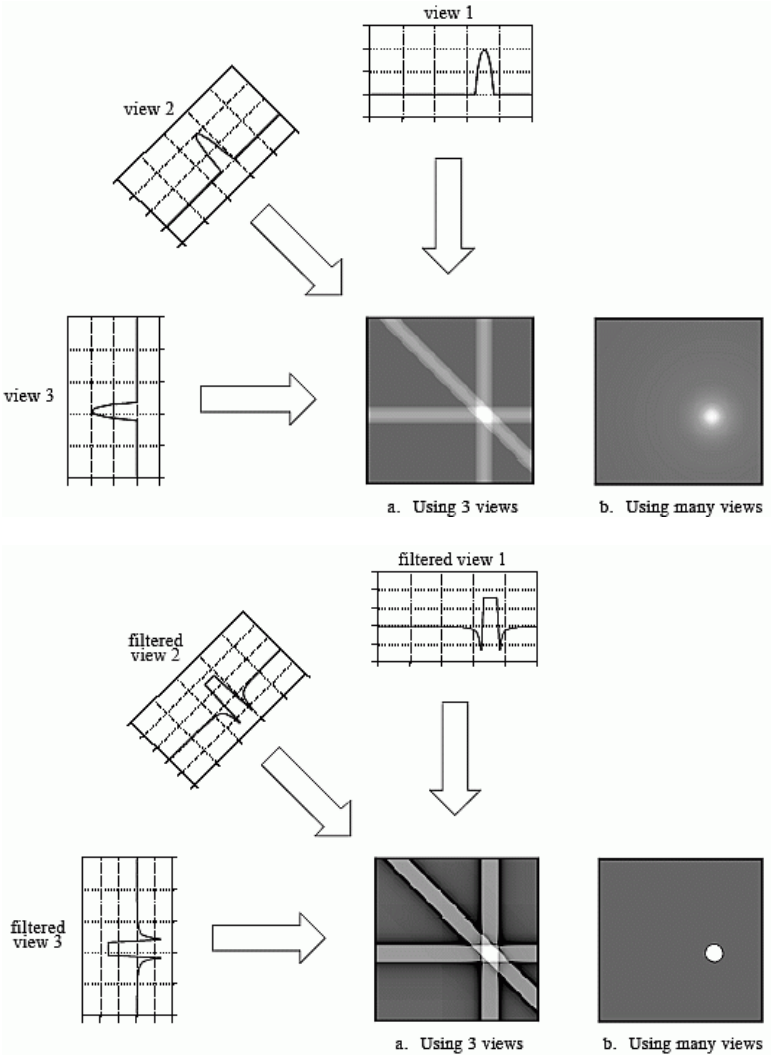

Figure 3.8: Image reconstruction by back-projection of radiographs. Top: Unfiltered back-projection, Bottom: filtered back-projection. [Smith, 1997]

cubic, hexagonal, tetragonal and orthorhombic crystals [Heinz and Neumann, 1991]. It can be converted into the 3x3 orientation matrix g by the formula given in [Poulsen, 2004]

$$g_{ij} = \frac{1}{1+\vec{r}^2}[(1-\vec{r}^2)\delta_{ij} + 2r_i r_j - 2\epsilon_{ijk} r_k] \tag{3.2}$$

with ϵ_{ijk} being the permutation tensor. In the case of a cubic system g is an orthonormal matrix ($g^{-1} = g^T$) where each row is a unit vector, representing the [100], [010] and [001] crystallographic direction of the grain, respectively. Using g, it can be calculated to which crystallographic orientation $\vec{v}_c$ in a given grain an orientation in the physical

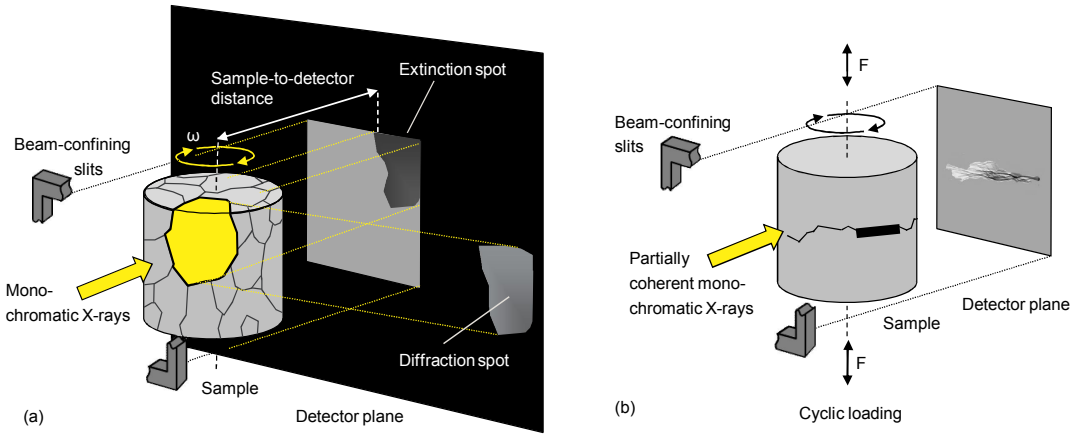

Figure 3.9: (a) Principle of DCT: 360° rotation of a polycrystalline sample in an extended, monochromatic X-ray beam. The detector is larger than the direct beam. Each grain runs through diffraction alignments several times. Grain position, shape and orientation can be reconstructed from the diffraction position and intensity distribution. (b) PCT: 180° rotation of sample in an extended, monochromatic and partially coherent X-ray beam. The detector has the same size as the direct beam. Successive tomographic scans are recorded at regular intervals during the interrupted in-situ test.

coordinate system (sample coordinate system) $\vec{v}_s$ corresponds to:

$$\vec{v}_c = g \cdot \vec{v}_s \tag{3.3}$$

The indexing procedure has proven to be robust and applicable to sample volumes containing up to a few thousand grains. The typical size of the illuminated area (500x500 pixels on a 2048x2048 pixel detector) and the requirement to have sufficient spatial sampling of the diffraction spots for 3D shape reconstruction ($>$ 20x20 pixels per spot) result in some typical boundary conditions concerning maximum sample size and minimum grain size (both expressed in terms of detector pixels). Consequently, a large range of physical sample and grain sizes can be investigated by appropriate choice of beam energy and pixel size of the detector system (energies between 15 and 50 keV and resolutions between and 1 μm and 20 μm have been explored so far for different material systems). For the Beta21S sample containing 1000 grains in the region exposed to the beam, about 80,000 diffraction spots were captured on 7200 images during continuous sample rotation over 360°. The semi-automated reconstruction of such a volume takes about 1 day using a cluster of 50 computers.

Limitations and Requirements The simultaneous, extended beam illumination of a large number of grains requires some conditions in terms of deformation state, texture and grain size of the material to be fulfilled to make it amenable for this type of characterization:

- Intragranular orientation spread: The presence of orientation gradients inside a grain leads to the violation of the parallel projection approximation and may result in distortion and breakup of diffraction spots. The inverse reconstruction procedure outlined in [Ludwig et al., 2009b] cannot correctly handle such cases. For this reason DCT works best for microstructures exhibiting only limited levels of intragranular orientation spread (typically below 1°).

- Defect density: Defects like dislocations change the d-spacing locally and result in blurry diffraction spots. A highly plastically deformed material would thus have to be recrystallized. Of great importance is also that surface damage due to sample machining is removed, for example by mechanical polishing.

- Subgrain boundaries: Despite the high angular resolution provided by the DCT indexing approach for similar reasons to the ones mentioned in the previous paragraph, it can be problematic to accurately reconstruct grains which are divided into subgrains by small angle grain boundaries with low misorientation values ($<$ 2 degrees).

- Texture: If some adjacent grains have similar orientations there is a high probability that the diffraction spots overlap which makes it impossible to use them for further analysis. Those diffraction spots have to be removed from the dataset. With increasing level of such overlaps the quality of the reconstructed grain map will become worse.

- Sample shape: The sample shape should ideally be cylindrical for constant attenuation at all sample rotation angles.

- Attenuation: The imaging performance of detectors decays at high energies. For a given mamximum energy, the sample diameter has to be adjusted such that the X-rays aren't completely absorbed. When working at 40 keV on a cylindrical sample, the maximum diameter would be about 700 μm for a titanium and about 270 μm and 250 μm for a pure copper or nickel sample, respectively.

- Grain shape: Highly complex grain shapes as usually found in cast alloys (e.g. dendrites) result in less accurate reconstructions.

Although this list of requirements is normally not fulfilled in the case of industrial alloys (which often exhibit a complex multiphase microstructure) the method is very valuable for the study of phenomenons that concern the 3D microstructure of simpler model systems that fulfill the above mentioned requirements.

In practice it is usually best to test the suitability of a potential material candidate prior to the real DCT experiment. A simple, plate-like sample geometry is sufficient for such initial diffraction tests at a synchrotron. Otherwise the suitability can also be investigated using EBSD.

3.5.3 DCT Experiments

The DCT experiments were performed at the European Synchrotron Radiation Facility (ESRF) in Grenoble, France, using Bragg-Bragg Si {111} double crystal monochromators. The combined absorption and diffraction images were recorded on a high resolution detector system consisting of a transparent luminiscent screen (20 μm of active layer of Eu-doped $Gd_3Ga_5O_{12}$ on a 150 μm thick substrate) screen [Martin and Koch, 2006], visible light optics and a Frelon camera (2048x2048 pixels) [Labiche et al., 2007]. Using an effective pixel size of 1.4 μm, approximately 500 μm high sub volumes of the fatigue samples containing the notch were reconstructed.

Beta21S The experiment was performed on beam line ID11 at an energy of 40 keV. The distance between the sample rotation axis and the scintillator (sample-to-detector distance) was 5.5 mm, the exposure time was 8 s, the overall scan time for a set of 7200 images was 20 hours. The reconstructed volume contained about 1000 grains.

VST55531 The experiment was performed on beam line ID19 at an energy of 35.3 keV. The sample-to-detector distance was 4 mm, the exposure time was 5 s, the overall scan time for a set of 7200 images was 13 hours[1]. The reconstructed volume contained about 400 grains.

3.5.4 PCT Experiments

The PCT experiments were performed at the ESRF, on beam line ID19. This beam line offers a small source size and a long distance between source and sample (150 m, see figure 3.5) which results in partially coherent illumination at the sample position. Interference fringes at the boundary between low and high electron density objects enhance visibility of objects smaller than the actual image resolution and enable the detection of the crack in regions where the crack opening is below the sub-micron pixel-size, as detailed in section 3.5.2 [Cloetens et al., 1997]. The interrupted fatigue tests were performed using a dedicated fatigue machine which can be directly mounted on the synchrotron imaging setup (figure 3.10) [Buffière et al., 2006]. The central part of this fatigue machine, working in tension-tension, consists of PMMA (polymethylmethacrylat) which is almost transparent at the X-ray energies used. This makes it possible to perform the PCT scans without removing the sample from the machine, which saves a lot of time that would mainly be needed for the realignment of the sample in the beam after reinstallation. The downside of the machine is its size that limits the minimum sample-to-detector distance to 49 mm which causes artifacts (see section 6.3.2). Constant amplitude tests were performed at room temperature (frequency =

[1] VST55531 was scanned at ID19 which is installed on a low beta section and has a long source to sample distance and therefore is is supposed to have less flux than ID11. The exposure and total scan time was nevertheless shorter for VST55531 because the experiment was done 2 years later and technological advances on undulators, optics and detectors increased the overall efficiency. A state of the art DCT experiment on aluminum samples at ID19 at 17 keV takes nowadays about 2 hours.

25 Hz) with a tensile cyclic load ranging from 10 to 320 MPa (R = 0.03). Scans were taken under maximum load in order to minimize the contact areas due to crack closure effects and to enhance the accuracy of crack detection. The voxel size was 0.7 μm. The scans were taken during a 180° rotation. Since PCT does not require high monochromaticity, the interrupted in-situ crack propagation measurements were performed with a large bandwidth multilayer monochromator, providing two orders increase in photon flux compared to the double crystal monochromators used in the DCT experiments.

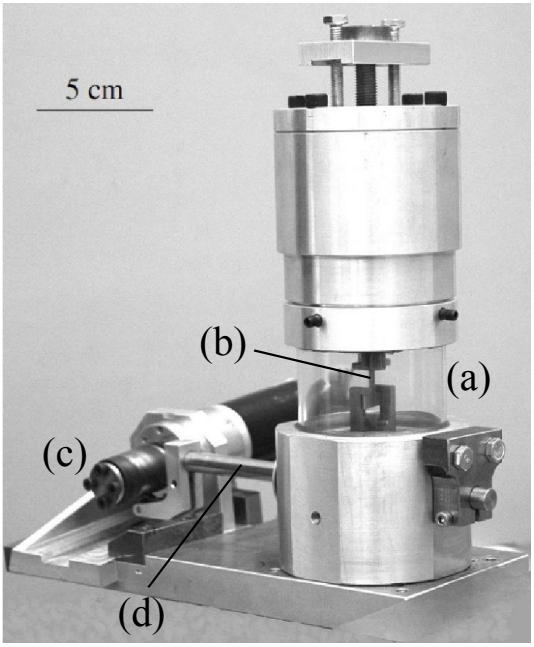

Figure 3.10: Fatigue Machine [Buffière et al., 2006] enabling (interrupted) in-situ measurements. (a) PMMA central part, (b) sample, (c) rotating ellipsoid that actuates the lever (d) which is connected to the bottom of the sample.

Beta21S 26 propagation stages between 45 k (45,000) cycles (first signs of growth at the notch root detected) and 75.5 k cycles were characterized at an energy of 38 keV and a sample-to-detector distance of 49 mm. At an exposure time of 1 s, a single scan of 1000 projections took 20 minutes.

VST55531 The sample was measured under improved imaging conditions as discussed in section 6.3.2. The energy was 52 keV and the sample-to-detector distance 53 mm. At an exposure time of 0.5 s, a single scan of 1500 projections took 26 minutes. Although 140 propagation stages between 28 k and 110 k were measured this work uses only the final stage, viz. only information about the fracture surface and not about crack propagation has been analyzed. For the Beta21S volume the 3D registration of the 26 volumes was done manually - a time consuming task. For the VST55531 volumes the registration procedure must be automated. Establishing an automatization procedure is still in progress, so the results couldn't be included in this work.

3.6 Evaluation of DCT

The Beta21S 3DXTSM sample was heat treated for 24 hours at 790 °C in order to make the grain boundaries visible in PCT (see figure 3.11, left). That way the accuracy of the grain boundary positions as reconstructed with DCT could be evaluated [Ludwig et al., 2009b]. The experiment was done at ID19 at an energy of 40 keV, an exposure time of 1.5 s, 0.56 μm pixel size a sample-to-detector distance of 150 mm.

Image Processing and Segmentation The PCT dataset showing the grain boundary precipitation can be used as a reference to assess the accuracy of grain shapes in the DCT grain map. However, it does not produce a perfect grain boundary map because during the second heat treatment a small fraction of grain boundaries are not decorated with the precipitated phase, and a certain amount of unwanted intra-granular precipitation occurs. These features must be corrected before it is possible to extract the complete boundary network required for automated, quantitative comparisons. A processing route, incorporating some prior knowledge from the DCT map, has been developed to determine an accurate grain map from the PCT data. All measurements and image processing steps were done using the commercial software MATLAB® and the free (for non-commercial users) matlab toolbox DIPimage. An explanation of the image processing terms used is given section 4.1.

Prior to processing, the DCT volume was scaled (oversampling by a factor 2.5) to give the same effective voxel size of the PCT volume, and the two datasets were registered.

Initial Segmentation The PCT data was de-noised using a median filter, and its contrast enhanced using contrast-limited adaptive histogram equalization [Russ, 2003]. A region growth algorithm was performed using VGStudio MAX to segment the grain boundaries as regions of interest (ROI). After a morphological closing of the ROI very small, isolated regions (mostly intra-granular precipitates) were excluded by applying a size filter in MATLAB®. Intra-granular precipitates still erroneously assigned the ROI were excluded manually using the non-commercial software ImageJ. Decorated grain boundaries not belonging yet to the ROI were included manually in the same way.

Restoration of Boundaries The resulting network of boundaries still contained some gaps due to the presence of non-decorated boundaries (figure 3.11, top). As illustrated in fig. 3.11, bottom, those gaps were filled with the help of a 3D watershed algorithm, using the DCT grain map as markers to avoid over-segmentation. The network of grain boundaries from the PCT data and the DCT grain map had to be modified in order to serve as a good ridgeline and marker map, respectively. The PCT network of grain boundaries was reduced in thickness to give accurate final grain outlines. The markers (derived from the DCT map after postprocessing) should be as big as possible to attain good results, but must not overlap with the network of grain boundaries. Due to the remaining inaccuracy of the DCT map, the latter condition is

not fulfilled everywhere and optimization of the marker map was done by performing the watershed algorithm without markers on the slimmed network of grain boundaries from the PCT data, yielding a closed but slightly wrong network of grain boundaries due to over-segmentation. This network was applied to the DCT grain map, dividing DCT grains which overlapped with the network of grain boundaries. The marker map was created out of the biggest sub-volume of each DCT grain. This marker map was used to obtain a final grain boundary map. Note that it is the ridgeline map which determines the boundary network shape, and the marker map only affects how non-visible grain boundaries are restored. Therefore it is valid to the resultant boundary map to assess the DCT map.

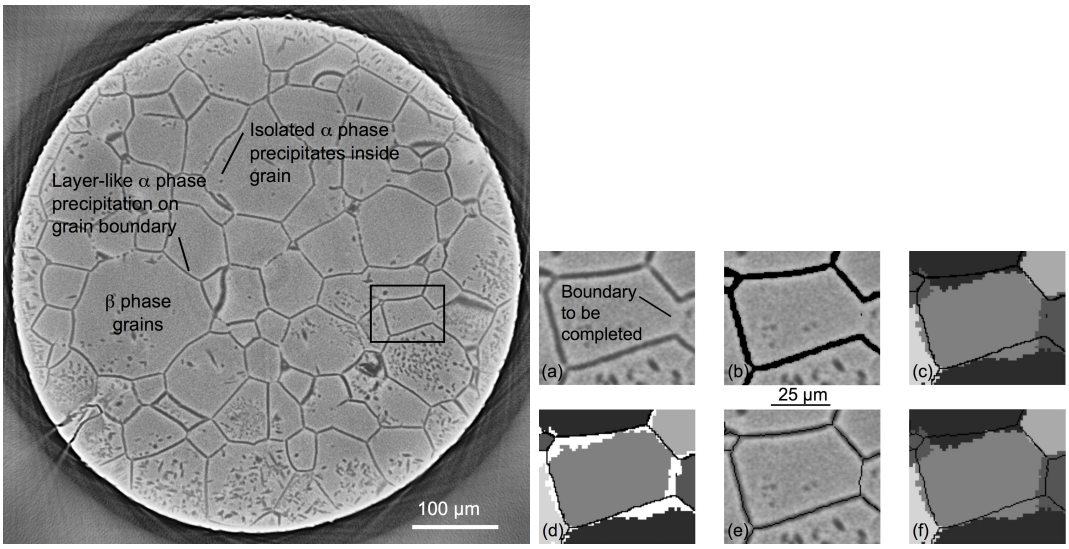

Figure 3.11: Left: Cross-section through the Phase-Contrast Tomographic (PCT) reconstruction. The α-phase appears dark. It precipitated during a heat treatment for 24 hours at 790°C performed after the 3DXTSM experiment. The rectangle marks the area on which the image processing for the completion of grain boundaries is illustrated. Right: Image processing steps for the completion of the grain boundaries not visible in PCT. (a) Shows the original PCT image after median filtering and contrast enhancement. One grain boundary is not visible and shall be completed. First, the grain boundaries are labeled semi-automatically as far as visible (b). The overlay of the slimmed labeled grain boundaries with the DCT image (c) shows that some DCT grains extend over the grain boundaries. Those parts have to be removed (d) before the DCT image can be used as marker image for the watershed algorithm. The missing grain boundary was completed (e). Note that the originally labeled grain boundaries remain unaffected by the algorithm. The accuracy of DCT was determined from the completed network of grain boundaries and the DCT data (f). (The average error for the grain shown in this Figure is 4.1 voxels or 2.3 μm).

3.7 SEM, EBSD

SEM and EBSD observations were performed on a Zeiss DSM982, at the Centre des Matériaux, Evry. Images were taken before and after a fatigue experiment in order to investigate the crack morphology and to reveal indications for stress-induced martensitic transformation (SIMT). The sample was fatigued at 25 Hz and 42-420 MPa using an INSTRON electropulse fatigue machine with a Dynacell load cell. After 36 k cycles several fatigue cracks had initiated at different places from the rough side, left from spark erosion into the polished surface. All EBSD images shown in figure 5.17 were acquired at an acceleration voltage of 20.0 kV, a working distance (WD) of 19.0 mm, a tilt angle of 70.0° and an exposure time of 20 ms. For (a) and (b) the signal was integrated over a surface of 2.0x2.0 μm^2, for (c) and (d) over 0.5x0.5 μm^2. The EBSD detector model UF-300 and the software were both by Nordif.

3.8 FESEM

For figure 5.16(①,②,③) the field emission scanning electron microscope (FESEM) Zeiss Gemini Ultra 55 was used. The field-emission-gun technology provides a stable electron source and a higher resolution (up to 0.8 nm) as compared to normal SEM. The experiments were done at the Max Planck Institute for Metal Research in Stuttgart, Germany.

3.9 XRD

As additional test for the occurrence of SIMT a synchrotron X-ray powder diffraction (XRD) experiment was performed at the ESRF on beam line ID31. A Beta21S sample, pre-fatigued at 25 Hz between 10 and 320 MPa for 440 k cycles was used for this experiment. The sample containing a crack at the notch of about 40 μm was rotated at 120 rounds per minute around the loading (cylinder) axis. The vertical beam size was reduced by slits to 30 μm. At a wave-length 0.3999 Å and a 2θ range between 0 and 35° one scan took 26 minutes. A single scan was donein the polished sample shoulder and a set of 30 scans were acquired across the notch with a spacing of 30 μm.

3.10 IXS

In order to perform crystal plasticity simulations on Beta21S several material constants have to be known; the Young's modulus; the isotropic and kinematic hardening behavior and the single crystal's elastic constants. Reid and al [Reid et al., 1973] measured for the pure beta alloy Ti-40Nb at room temperature C_{11} = 156.5 GPa, C_{12} = 111.6 GPa and C_{44} = 39.6 GPa. But according to Kuroda and Fréour [Kuroda et al., 1998; Fréour et al., 2005] these constants depend on the nature and concentration of the beta stabilizing alloying elements. Therefore, it was decided to measure our elastic constants

via inelastic X-ray scattering (IXS) using synchrotron X-rays. The experiment involves the transmission of a single grain in a thin foil with an X-ray beam.

The moduli are obtained via the sound velocities V as derived from the initial slope of the acoustic phonon branches along specific, mostly high-symmetry, directions, and Christoffel's equation [Auld, 1973]. The IXS experiment was performed on beamline ID28 at the European Synchrotron Radiation Facility. The instrument was operated at 17794 eV and provided an overall energy resolution of 3.0 meV full width half maximum (FWHM). The dimensions of the focused X-ray beam were 250x60 μm^2 (horizontal x vertical FWHM). The direction and size of the momentum transfer were selected by an appropriate choice of the scattering angle and the sample orientation in the horizontal scattering plane. The momentum resolution was set to 0.2 nm^{-1} and 0.7 nm^{-1} in the horizontal and vertical plane, respectively[2].

More details about this characterization method can be found in [Bosak et al., 2006, 2007]. The experiment and the calculation of the elastic constants were done by Alexei Bosak, ID28, ESRF.

[2][Bosak et al., 2006]

Chapter 4

3DXTSM Data Processing

4.1 Introduction to Digital Imaging

4.1.1 Pixels / Voxels

2D digital images are rectangular arrays of *pixels*. To each pixel one or three values are assigned which normally represent a gray tone or a color, respectively. But those values can actually represent any arbitrary content like, for example, a scalar or a vector field. In our case the gray value indicates that this pixel belongs to a given grain (DCT) or a given attenuation coefficient (ACT, PCT). Digital image processing involves reading in an image and producing a modified version of it. One of the most basic procedures is *thresholding*. A threshold value is selected and all pixels containing values above / below are set to 0 / 1. The output image is a *binary image*. In general, all processes producing an output image that contains only two different values are called *binarization*. More advanced image processing routines involve not only considering the value of a single pixel but also taking into account its relation to the values of its neighbors. A *mean filter* for example replaces a pixel value by the average value of its surrounding pixels and smoothens thereby the image. The next level of image processing involves not only taking the values of neighboring pixels into account but also geometrical features. Based on these principles features like edges can be highlighted, in the Fourier space high or low frequency patterns can be filtered, an image can be sharpened, the contrast enhanced...

More or less all of those principles can be also applied to three dimensions. A 3D image is simply a stack of 2D images (figure 4.1). What is called pixels in 2D is called *voxels* in 3D. The next level of complication would involve tracking of features that evolve in time. A 3D image that alters in time constitutes a 4D data set. It is important to mention that the computational effort of image processing increases exponentially with the dimension of the dataset. In practice one could expect that any information visible in an image by the human eye could be extracted automatically. But the less visible the features are the more demanding the extraction gets.

Further important image processing terms used for this work are explained in the

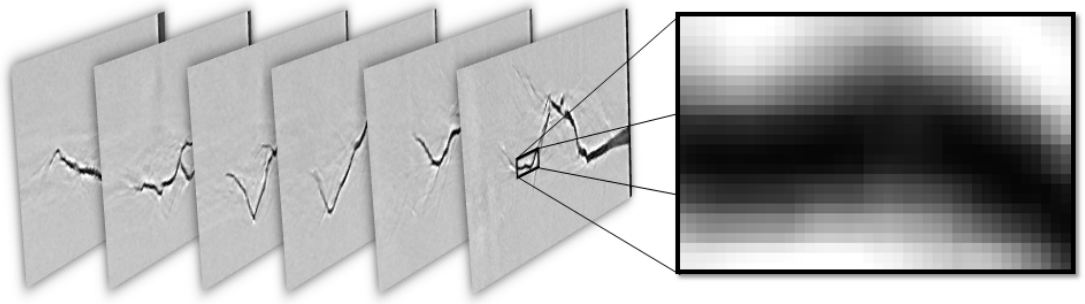

Figure 4.1: 3D images are stacks of 2D slices. The zoom into a subregion of a slice illustrates that those are are built up of pixels.

following list.

- *Segmentation* is the general term for processes that subdivide an image into segments. One way to segment a volume into two different areas is thresholding.
- The output of a segmentation is called segmented, *labeled* or binarized image (the latter if the output image contains only two different values) and means that all pixels belonging to the same segment (e.g. a grain) have the same value.
- The median of a list of numbers can be found by arranging all the values from lowest to highest and selecting the middle one. A *median filter* replaces the value of each pixel by the median value of its own and its neighboring pixels. The algorithm is suited to remove salt and pepper noise (pixels with very high or very low gray values) which is common in tomography raw volumes. The algorithm thereby smoothens the image but blurs strong color transitions (gradients) like edges less than a mean filter would do.
- A *region growth* algorithm finds and segments interconnected voxels within a certain gray value range.
- Morphological *dilation / erosion* involves adding / removing layers of pixels to / from the boarder of a segmented array.
- The sequential execution of a morphological dilation and erosion by the same value can be used to fill gaps in a segmented area. Such an operation is called *morphological closing*.
- The *distance transform* algorithm works similar to the dilation algorithm, but each added layer of pixels receives a successively increasing value. The inverse of the thereby produced image can be used as input data for *watershed* algorithm [Beucher and Lantuéjoul, 1979]. The algorithm considers the distance transform output as a topographic relief. It places a "water source" from which the relief is "flooded" in each regional minimum and builds barriers in the regions where

different sources are meeting. The subsequent use of distance transform and watershed can be used to complete for example a grain boundary network containing holes.

- The *isosurface* algorithm finds the outline of all segments having the same gray value and converts it into a surface mesh that can then be visualized.
- A *minimum intensity projection* involves finding the minimum values of each column of a 3D volume along a certain direction and writing them into a 2D image.
- *Sampling* is a vocabulary used in signal processing and describes the reduction of a continuous signal to a discrete signal. *Resampling* transforms discrete in other discrete values. *Oversampling* in 3D image processing means that the voxel size for a volume is reduced. This goes along with an exponential increase of the image size. Oversampling a volume by a factor 2 means that the new volume contains 8 times more voxels and needs 8 times more memory. Oversampling using interpolating algorithms reduces noise and smoothens the image.
- *Image registration* is the process of transforming different sets of data into one coordinate system. It is for example necessary if two complimentary data sets of the same object were taken from a different perspective and have to be made coinciding (like a DCT and a PCT data set).

4.1.2 Surface Meshes

Every surface mesh consists of one or more *patches*. A patch is a cluster of *faces*. A face is normally a triangle but it can also be a polygon of higher order. The corners of a face are called *vertices* (singular: vertex). Some of the imaging processing routines can also be also applied to surface meshes. It is for example possible to find the neighboring triangles around a triangle cluster and thereby perform a dilation or a distance transform on the mesh. In order to be able to code such algorithms the method used for describing the mesh must be known. A common way (e.g. used by MATLAB®) is shown in figure 4.2. Each patch is described by two arrays called "faces" and "vertices". The vertical index of "faces" is the face number (the number that identifies the face). The vertex numbers, that is the identification numbers of the corners that comprise that face, are noted horizontally. In "vertices" the vertex number is the vertical index. Horizontally the coordinate of each vertex is noted.

A triangle's orientation can be represented by a color. This is usually done by creating a hemisphere of radius one where each point has a unique color and calculating at which point the triangle's normal encounters the hemisphere. The thereby created colormap associates each triangle orientation to a unique color. In order to show this colormap in 2D it is normally projected on a plane. Doing a standard stereographic projection improves the visibility of the regions of the hemisphere which are highly inclined with respect to the projection plane. Due to the symmetry of crystal lattices many orientations are equivalent. Therefore, for crystallographic applications

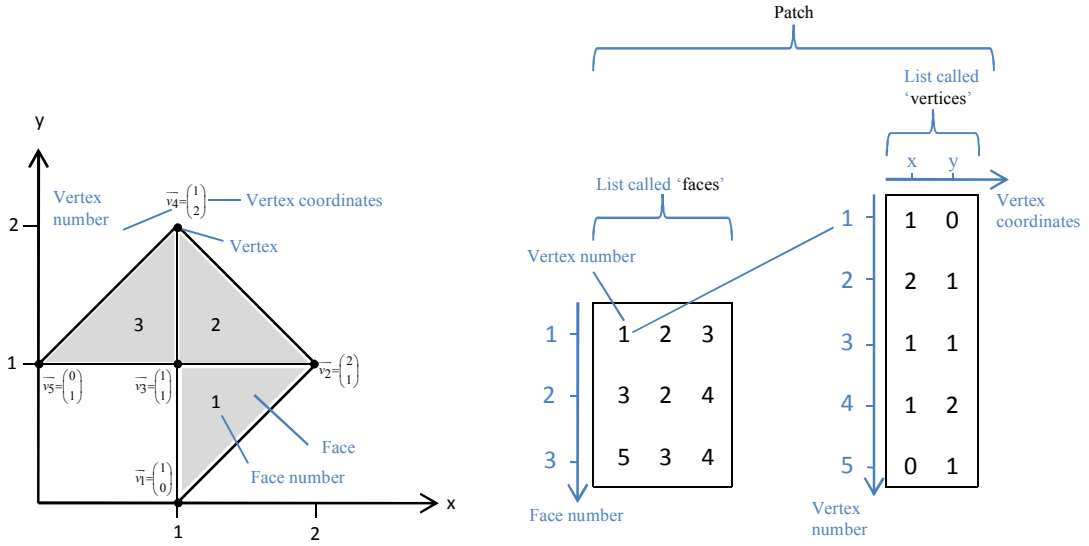

Figure 4.2: Surfaces meshes are commonly described by two arrays called "faces" and "vertices".

often only a subregion of the hemisphere, called standard stereographic triangle (SST), which contains all possible non-equivalent orientations is depicted. In crystallography a crystallographic plane normal is normally called "pole" and a standard stereographic projection commonly pole figure.

4.2 Overview

The following section describes the state of the art data processing routine needed for the 3DXTSM method starting from the reconstructed DCT and PCT volumes. The data processing involved in the reconstruction of DCT and PCT volumes is found elsewhere [Cloetens, 1999; Kak and Slaney, 2001; Ludwig et al., 2009b]. The processing was mostly done using Matlab and its image processing toolbox and the non-commercial Matlab plug-in DIPimage [Hendriks et al., 2010], but also involved using the commercial softwares Avizo® and VGStudio MAX.

A general challenge in 3D imaging (4D if time is considered) is that the datasets obtained contain tremendous amounts of information. This is even more important for orientation maps. In our case we deal with a seven dimensional dataset, since each point in the 3D space contains three variables for the grain orientation and one additional variable describing if the crack is present or not after a certain number of cycles. Developing appropriate ways of visualizing these different aspects of material properties and mechanical behavior is therefore one of the crucial tasks.

Broadly, the routine described here consists of the registration of the volumes, the creation of a surface mesh that represents the crack in the final PCT volume, creating a

single volume that contains all information on crack propagation, and unifying all this information in a data structure from which all aspects can easily be extracted and visualized. The data processing routine described here has been shown to work, but there is certainly room for improvement. For example, the registration of volumes that was done manually could be automatized. Details concerning different processing routines and the optimization of parameters as well as recommendations for improvements can be found in the discussion. The whole procedure was only performed on the Beta21S dataset. For VST55531 only the final growth volume was processed, so no information on the chronological evolution of the crack is available.

4.3 Registration

The DCT and PCT volumes have to coincide perfectly. Only then is it possible to find out to which grain each crack voxel corresponds. If the sample moves between two scans, then the reconstructed volumes are no longer congruent. The smaller the samples, or the features of interest, the less absolute movement can be tolerated. In our case the samples are so small that the vibrations during the fatigue experiment are enough to make registration of the PCT volumes necessary. Between the DCT and the PCT volumes there is an even greater difference in orientation because the sample has to be manually mounted into the fatigue machine after the DCT measurement. This setup change is necessary because the DCT experiment requires a very short sample-to-detector distance ($\approx$5 mm) that is not possible when the sample is in the fatigue machine (figure 3.10).

Altogether a 3DXTSM dataset consists of two DCT volumes, that is a grain map reconstructed from the diffraction spots and a volume reconstructed from the direct beam ("DCT absorption volume"), and of one PCT volume for each crack propagation stage scanned. The two DCT volumes coincide perfectly after accounting for different coordinate systems used in the reconstruction algorithms[1], since they are reconstructed from the same scan. Figure 4.3 summarizes the misorientations between the DCT and the PCT volumes in an exaggerated way.

The registration procedure consists in rotating and shifting all PCT volumes so that they coincide with the DCT volumes. The orientation of the DCT volumes was left untouched to avoid having to modify the grain orientations.

The first step is to register the PCT volume before fatigue (PCT 0 k volume) with the DCT absorption volume. Both volumes depict the sample in exactly the same condition which is not the case for any other combination of DCT and PCT volumes. Since only the center of the detector is used to capture the direct beam during DCT the DCT absorption volume has a lower resolution than the PCT volumes. The corresponding scaling factor can be determined by thresholding and comparing the surface area of a slice at the same position in the two volumes. Using this scale factor, the DCT absorption volume is resampled to the size of the PCT volumes. The DCT volume is

[1] The x and y axis of the DCT absorption volume must was permuted and the z axis inversed to make it coincide with the grain map.

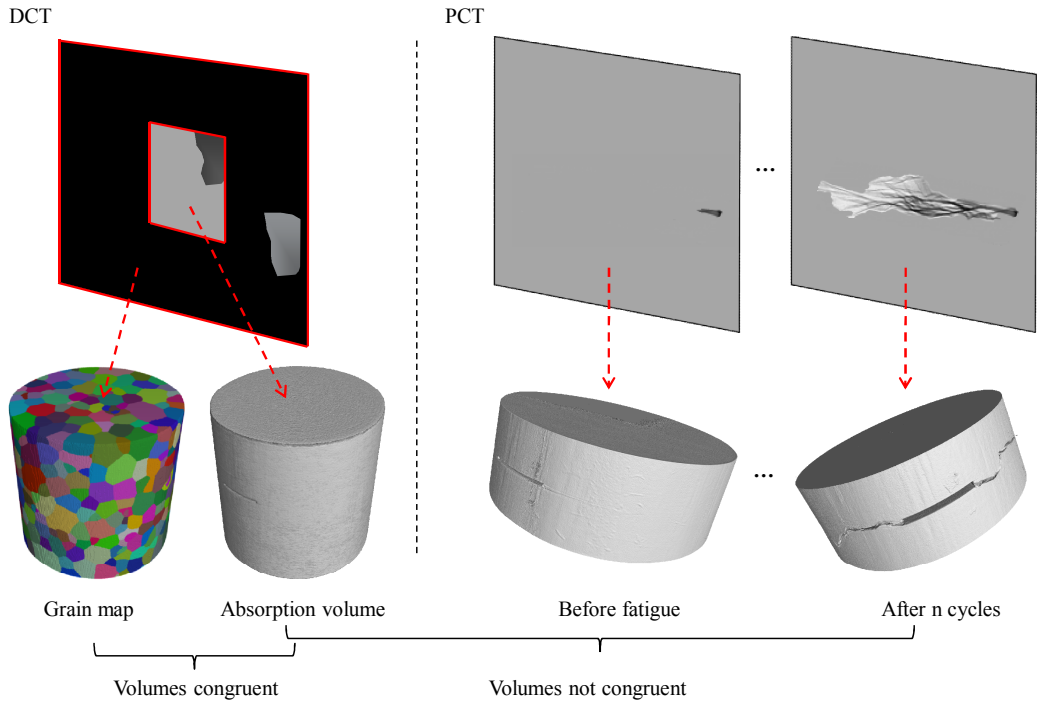

Figure 4.3: Misalignment between volumes from DCT and PCT

upscaled because this allows the higher resolution of the PCT volumes to be exploited, and only one volume needs to be resampled. Next, the misalignment in rotation around the z axis (vertical axis) was determined by performing a minimum intensity projection along z. In this projection both, notch and sample outline are clearly visible. By rotating, shifting and subtracting the projections the right parameters can be found manually. After applying these parameters to the whole volume the procedure was repeated in x and y direction, in which much smaller rotations are expected.

The PCT 0 k volume is then registered with the DCT absorption volume. Next, this registration procedure was applied to all other PCT volumes. All of them were registered with the PCT 0 k volume since the contrast between two PCT volumes differs less than between a PCT and the DCT absorption volume what makes the registration easier.

4.4 Creation of the Mesh

In order to analyze orientation relations between grains and crack, the local normal to the fracture surface needs to be determined. Therefore, the outer layer of voxels belonging to the crack in its final stage is transformed into a surface mesh composed of triangles. Once such a mesh is created, the local surface orientations can be calculated, and all other information such as the crack plane orientation, grain boundary positions, and crack growth rate can be visualized as colors on the mesh. The surface mesh

was extracted from the final PCT volume (showing the crack in the last growth stage measured).

Oversampling In order to loose as little information on the crack morphology as possible when converting the raw data into a surface mesh, the final PCT volume was oversampled by a factor of three using an interpolating algorithm. The effect of this procedure is discussed in section 6.3.3.

Segmentation The final stage of the crack was segmented by applying sequentially a 3D median filter to reduce noise in the reconstructed image (8 bits coding), segmentation using a region growth algorithm, and a manual removal of artifacts using the commercial software VGStudio MAX.

Meshing The mesh was created from the crack in its final stage using the isosurface and smoothing algorithms of the commercial software Avizo©. As isosurface algorithms extract the hull of labeled objects our surface mesh describes the outline of the segmented crack. It has therefore an upper and a lower surface, separated by the crack opening which is about 15 μm at the notch. Coding an algorithm that extracts the mean plane from these surfaces is one task to be done for the future. Four iterations of surface smoothing (each time ten repetitions, smoothing parameter $\lambda = 0.7$) were performed and the number of triangles halved, to remove the stairway-like features from the mesh which arise from the voxelated data (see section 6.3.4). The final number of triangles was about 1,000,000 for a crack size of 0.14 mm^2 in the case of the Beta21S sample.

4.5 Conditioning of the Remaining Data

Creation of Propagation Volume So far a mesh was created from the final PCT volume. Now all other PCT volumes (termed "residual PCT volumes" in this paragraph) are segmented and merged into a single volume that will be termed the "propagation volume". The segmented final PCT volume was undersampled back to the size of the residual PCT volumes to simplify their segmentation. The search for voxels belonging to the crack in the residual PCT volumes was restricted to the subvolume belonging to the segmented crack in the final stage. Within this subvolume simple thresholding was enough to segment the crack. Small gaps in the thresholded crack volumes due to artifacts were filled by morphological closing. The segmented cracks in the residual PCT volumes were dilated vertically to fill the mesh. This is necessary because the mesh was created from the crack in its final state, in which it was the longest and the crack opening displacement the biggest, meaning that the segmented cracks in the residual volumes were thinner, laying inside the mesh. All voxels belonging to the crack in each volume were given their corresponding cycle number. All segmented cracks were sequentially copied into the empty propagation volume, starting with the last stage and ending with the first, always overwriting the voxels which are already occupied by

the crack in a later state. That way a labeled volume was created in which all parts that formed during a certain interval are labeled with the cycle number at the end of this interval. By comparing triangle positions of the mesh and voxel positions in the propagation volume, a number of fatigue cycles can be assigned to the crack surface.

Oversampling the Grain Map The grain map was oversampled with the same resampling factor as used for the DCT absorption volume (see section 4.3). A non-interpolating algorithm must be used to maintain the correct grain labels in the volume at each position.

4.6 Creation of a Data Structure Summarizing all Information

After having created the mesh, the propagation volume, and having upscaled the grain map, everything is prepared to create a data structure which summarizes all information and from which different aspects of the whole data set can be extracted and visualized easily. After importing the mesh into Matlab the vertices were divided by a factor three to rescale the mesh to the size of the PCT volumes. The data structure consists so far of a list of faces and vertices describing the fracture surface as explained in section 4.1.2 and a list relating grain numbers to orientations. Four further parameters are assigned to each triangle of the mesh by comparing triangle positions in the mesh and voxel positions in the grain map and the propagation volume, respectively.

- Physical orientation: surface normal of triangle in the sample coordinate system, calculated by taking the cross product of the vectors that make up the edges of a triangle.
- Grain affiliation: the grain to which the triangle is affiliated. If not all triangle vertices are contained in a single grain of the grain map, then it is labeled as belonging to a grain boundary.
- Crystallographic orientation: surface normal of triangle in the crystal coordinate system of the grain to which the triangle is affiliated. The coordinate transformation is done by multiplying the physical orientation with the matrix describing the grain orientation as formalized in equation 3.3. A second set of crystallographic orientations was used for the symmetrical equivalent of the crystallographic plane orientation, lying in the standard stereographic triangle.
- Propagation stage: the number of fatigue cycles after which this part of the crack appeared. If not all vertices are contained in the same propagation stage of the propagation volume it is labeled as belonging to a crack front.

Additionally the Schmid factor and the local crack growth rate per grain were added to the data structure.

- In order to calculate the Schmid factor the slip plane normals and slip directions were transferred into the physical coordinate system by multiplying them with g^{-1} (see equation 3.3). For all grains a purely vertical load (along the z-axis) was assumed. This procedure treats the grains as isolated single crystals, neglecting all local stress modifications arising from the anisotropy of neighboring grains or the crack.

- In order to calculate the local crack growth rate from the crack fronts an algorithm was developed that is capable of measuring growth rates on cracks with complicated morphologies like branchings. Starting from one crack front and ending at the next one (figure 4.4a) the algorithm successively finds sets of adjacent triangles and labels them according to the iteration in which they were found (figure 4.4b). That way, the labels of the last row of triangles before the next crack front (figure 4.4c) represent the local growth distance. The scaling factor between those label values (number of dilation steps) and the real growth distance da was calibrated at the notch, since it represents a flat part where the real distance can be easily measured.

- The average growth rate per grain was determined by calculating the average of all growth rates on all crack fronts intersecting each grain.

4.7 Visualization

Most of the data was visualized on the 3D rendered image of the crack. Potentially this can be done working with either voxelated or meshed data. A mesh is advantageous since it intrinsically has an orientation. However, some of the illustrations that don't deal with orientation relations (figure 5.2) are based on voxelated data for the simple reason that in those cases software can be used with which visualization is very simple. The color of each triangle of the mesh was calculated from its normal as detailed in section 4.1.2. The content of a 3DXTSM dataset is too manifold to be illustrated in a single image. Using the created data structure makes it easy to plot the combination of information that emphasizes a certain aspect of interest. The fracture surface can be shown from different perspectives (figures 5.5 (b-d)), either the physical (figures 5.5) or the crystallographic orientation (figure 5.6) can be shown, grain boundaries or crack fronts can be added to the figure (figure 5.7a), the crack can be shown at different points of times (figure 6.13), only subregions like certain grains of the mesh can be depicted (figure 6.11), text like grain numbers can be added (figure 5.4), semi-transparent slip planes can be added (figure 6.10b) and videos can be created showing several aspects in motion (see supplement video in online publication [Herbig et al., 2011]).

Statistics on orientations were done using pole figures. A simple version, plotting a symbol for each pole, is used to compare slip plane activation and the fracture surface orientation distribution in a given grain (figure 5.10). A more sophisticated version

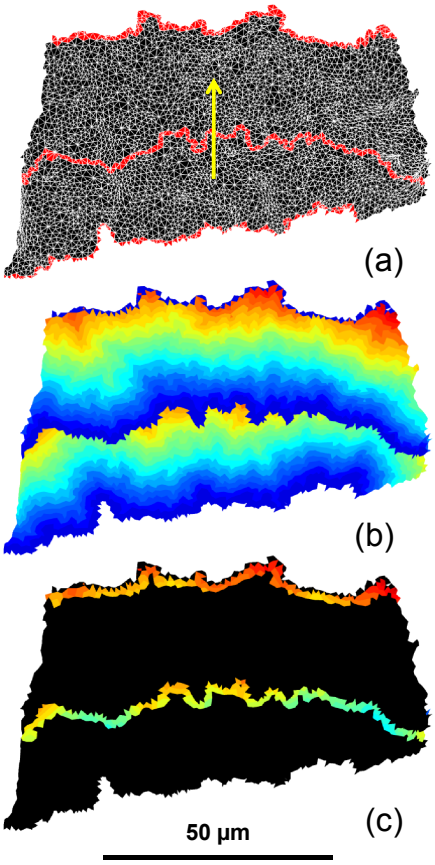

Figure 4.4: Principle of the algorithm measuring the local crack growth rate shown on the fracture surface within a single grain. (a) The outlines of the triangles making up the surface mesh are labeled in white. The red lines mark the crack front at given numbers of cycles, the yellow arrow the direction of crack growth. (b) Starting from one crack front and ending at the next the algorithm successively finds arrays of adjacent triangles. (c) The last row of triangles before the next crack front contains the information on local crack growth distance as a number of triangles.

showing the pole density is used to plot the texture (figure 5.12) and the pole density distributions (figure 5.11).

Chapter 5

Results

5.1 3DXTSM

Table 5.1 summarizes the conditions for the two 3DXTSM experiments. Two in-situ experiments were performed but only the Beta21S dataset was completely analyzed. The crack in VST55531 was scanned at 140 propagation stages up to 110 k cycles in order to provide accurate time resolution. Automatizing the registration procedure of these 140 volumes is work in progress. That is why only fracture surface in the final growth state in the VST55531 sample was analyzed, and not its propagation.

Alloy name	VST55531	Beta21S
Alloy type	Near β-titanium alloy	Metastable β-titanium alloy
Composition	Ti-5Al-5V-5Mo-3Cr-1Zr	Ti-15Mo-3Nb-3Al-.2Si
Heat treatment	2 h at 843°C, air cooled	2 h at 850°C, quenched in water
Average grain size	65 μm	55 μm
Fatigue conditions	uniaxial tensile loading, 10-320 MPa, 25 Hz frequency	
PCT scans	single growth state (110 k cycles)	26 states (45 k - 75.5 k cycles)

Table 5.1: Overview of the two 3DXTSM experiments done.

5.1.1 Grain Size Distribution

The average grain sizes given in table 5.1 were calculated using the grain maps. Knowing the voxel size and the number of voxels each grain is composed of, the grain size distributions depicted in figure 5.1 were calculated. The size of each individual grain was assumed to be the diameter of a sphere having the same volume as the grain. The grain size distributions in both material systems can be described by log-normal distribution functions. The average grain size for Beta21S and VST55531 was 55 μm and 56 μm, respectively.

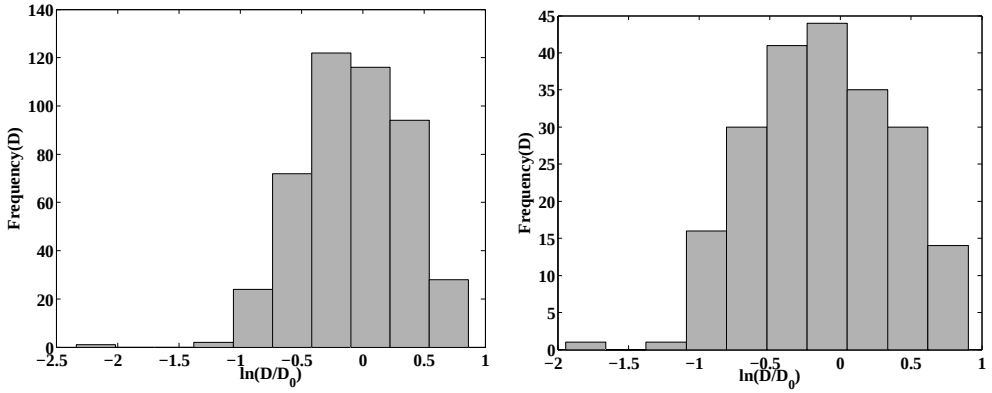

(a) Beta21S (b) VST55531

Figure 5.1: Grain size distributions in the two alloys investigated, where D and D_0 are grain size and average grain size, respectively.

5.1.2 Voxelated Data

The depictions based on voxels shown in figure 5.2 illustrate the information on grain shape, crack morphology (and crack propagation if the corresponding video published online [Herbig et al., 2011] is taken into account) but orientation relations between crack and grains are not visible. The figure also shows a 3D rendition of the morphology of the crack in Beta21S at the end of the experiment. The crack initiates at the FIB notch and grows until about the middle of the sample. On average, one tomographic scan was recorded every 1000 cycles but this number was decreased to 500 to account for the faster growth rate towards the end of the experiment (an animation showing the different stages of crack growth as well as the grains intersecting the fracture surface can be viewed as supplementary material linked to the online version of the article [Herbig et al., 2011]). Although the fracture surface appears macroscopically perpendicular to the loading axis, it can be seen from figure 5.2a that the crack morphology shows pronounced branchings and deviations. This behavior is typical of SFC and most likely due to the presence of grains as the typical scale of deviations (a few tens of micrometers) tend to indicate. On figure 5.2b only part of the grains intersecting the fracture surface have been made visible. As a first approach, figure 5.2c and d show the crack path on planes clipped within the volume as they would appear on observations made by sectioning the sample. In some cases strong deviations of the crack are clearly correlated with the presence of grain boundaries (figure 5.2c) but some deviations can also be observed within a grain (e.g. arrow on figure 5.2d).

5.1.3 Unlabeled Fracture Surface

Figure 5.3 shows a rendering of the 3D surfaces of the segmented cracks in the last propagation state measured. Those surface meshes composed of triangles will be referred

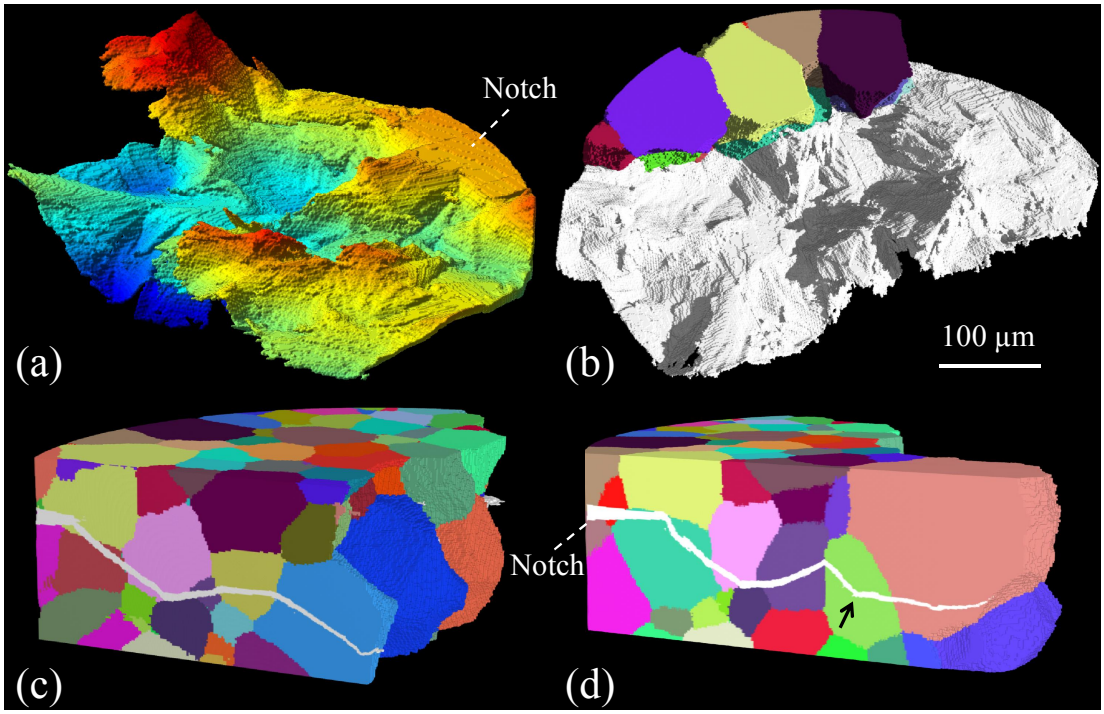

Figure 5.2: 3D rendition of the fatigue crack after 75.5 k cycles in Beta21S (the fatigue load is applied vertically). a) the colors represent the vertical crack position: blue = 0 μm, red = 180 μm. b) 3D rendering of the crack together with some grains in proximity to the notch. Each grain is given a different color. c) and d) "classical" 2D views of the crack path on different planes cut in the bulk of the sample. Changes in direction of the crack can be correlated with the presence of grain boundaries (c) but can also be observed within a grain (arrow in d).

to as fracture surfaces in the following. Figure 5.3 shows the meshes in an unlabeled state, that means without taking any information on grains or crack propagation into account. The variations in intensities represent the reflections casted by a virtual light source. The visualization algorithm used for this purpose is available in most surface visualization programs; it is a good way to reveal the 3D surface morphology. An eyecatching feature of VST55531 is that the crack propagated during 110 k cycles only on one side of the notch.

5.1.4 Grain Identification

Figure 5.4 shows the same fracture surfaces, this time with labeled grains. For both materials transcrystalline cracking was observed. Each intersection point between fracture surface and a grain boundary is labeled in black. All parts of the fracture surface that intersect the same grain are given the same color. Above the center of gravity of all triangles belonging to a grain the corresponding grain (identification) number is plotted.

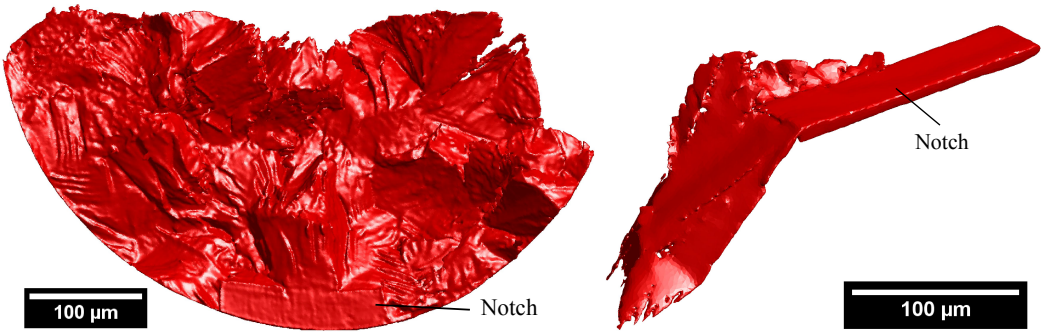

(a) Beta21S (b) VST55531

Figure 5.3: Unlabeled fracture surface meshes of (a) Beta21S after 75.5 k cycles in top view and (b) VST55531 after 110 k cycles in side view perspective. In both cases the fatigue load was applied perpendicularly to the notch.

For reasons of simplicity all grains discussed in the following will be given letters.

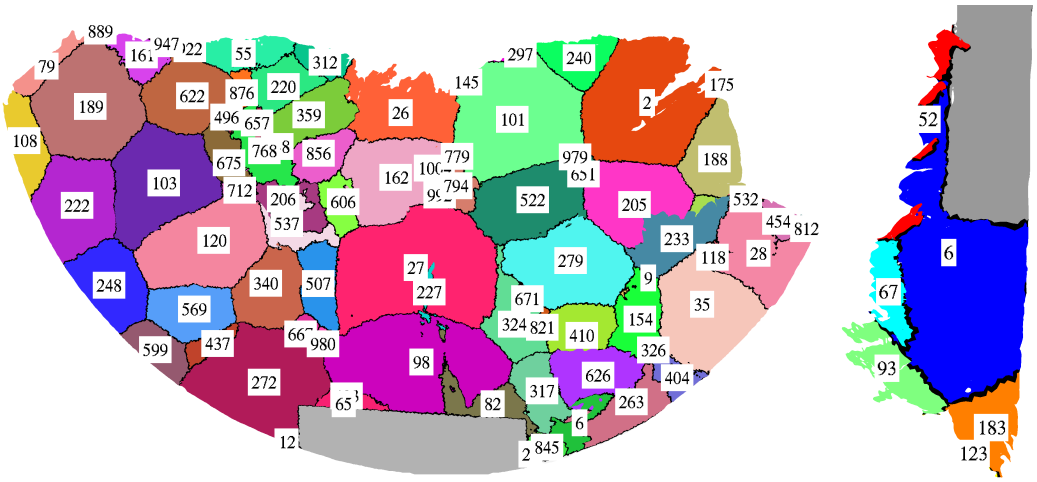

(a) Beta21S (b) VST55531

Figure 5.4: Top view on the fracture surfaces. The labels correspond to the grain numbers of the grains intersecting the fracture surface.

5.1.5 Physical Orientation of Fracture Surfaces

Figure 5.5 shows the fracture surface with a color map representing the orientation of the surface in the sample coordinate system. The good accuracy obtained during alignment of the DCT and the tomography images is shown by the correlation between strong orientation/color changes with the presence of grain boundaries (grain a and b for example). By looking closely at figure 5.5a, however, one can see that the crack

can sometimes cross grain boundaries without being deflected (e.g. grain b and c). In some cases changes in the orientation of the fracture surface can also be observed within a single grain with a regular pattern of short spatial wavelength (grain d) or on distances comparable to the grain size (grain e). A remarkable feature of figure 5.5 is that color changes within individual grains occur less often in the case of VST55531 compared to Beta21S. In VST55531 the fracture surface seems to be more planar. The crack stays mostly on a single plane within one grain and changes its direction at each grain boundary. The arrows in figure 5.5d mark almost coplanar, displaced facets that are only connected at their origin.

Using the data obtained from DCT, it is possible to further analyze such deflections with respect to the local crystallography. This can be done by applying the crystallographic color coding to the fracture surface as shown in the next paragraph.

5.1.6 Crystallographic Orientation of Fracture Surfaces

Figure 5.6 shows a 3D rendering of the crystallographic orientation of the fracture surface. Each triangle has been assigned a colour corresponding to the equivalent orientation in the standard triangle of the local crystallographic coordinate system. A striking feature in the case of Beta21S is that the surface mesh contains many other colors than those corresponding to the "classical" bcc slip planes, i.e. {101}, {112}, {213} [Honeycombe, 1984] while in the case of VST55531 almost all visible colors can be related to bcc slip planes. At the spatial resolution achieved in this study, it appears therefore, that the crack in Beta21S is propagating on slip planes only in rare occasions as e.g. in half of grain e where the fracture surface is parallel to a crystallographic {101} plane.

5.1.7 Chronology of Crack Growth in Beta21S

Figure 5.7a shows successive crack fronts as observed during the in-situ propagation experiment, projected onto the 3D fracture surface. It can be seen on this figure that the growth of the crack is nearly continuous throughout the test except for a few places (arrows on figure 5.7a). The left and middle arrows on this figure show enclosed areas which get smaller and smaller with each fatigue cycle. As the crack front position is determined automatically on the images, this indicates that the crack was detected later by the algorithm, either because the material was indeed un-cracked in this region, or because the crack was too tightly closed to be detected by PCT. The right arrow marks a continuous region which represents an uprising crack branch that covers the parts below. The left side of this branch is a good example for the variance of the crack growth rate which is locally very low compared to the rest of the crack after the same number of cycles.

For a given number of cycles, a range of growth rates can be found along the crack front, especially in the first stages of growth. Parts of the crack front close to the free surfaces tend to grow faster, (especially on the left hand side of the specimen) and some variations can be correlated with the presence of grain boundaries (e.g. grain g,

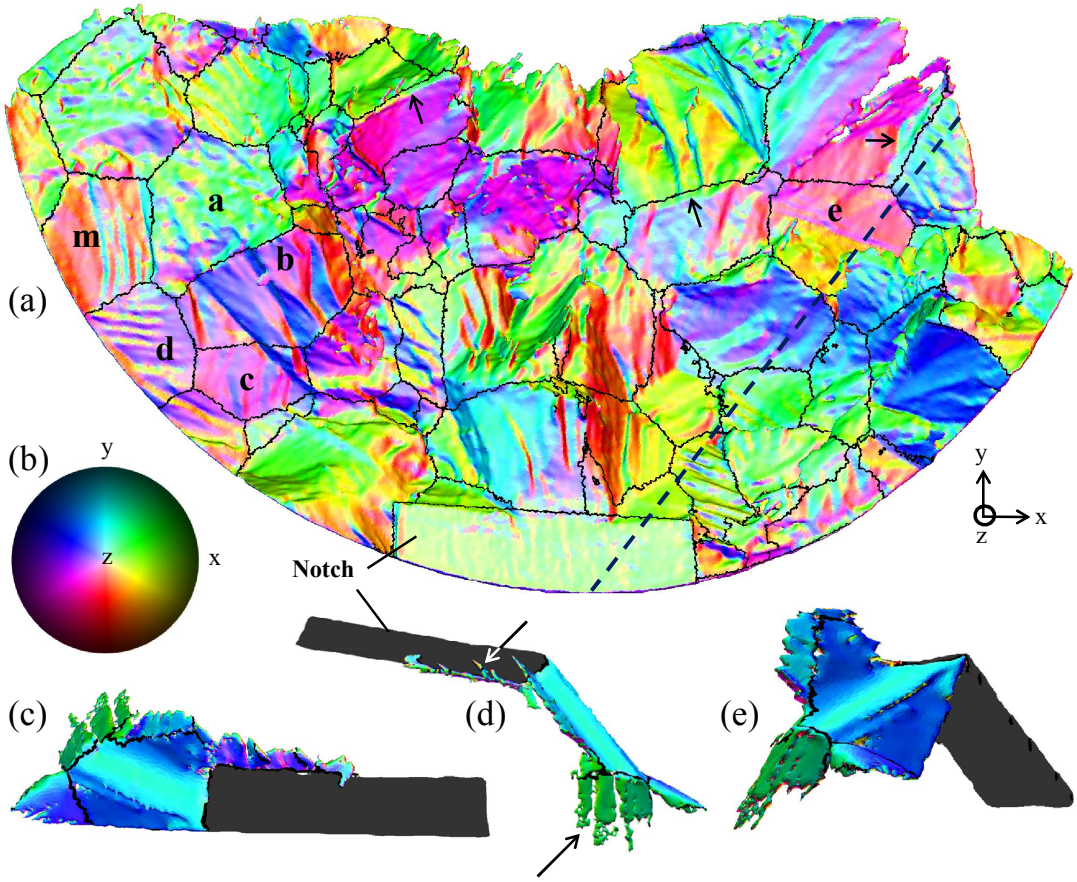

Figure 5.5: (a,c) View along the loading axis on the fracture surface of Beta21S and VST55531, respectively. Black lines indicate intersections of the crack with the grain boundaries. The triangle colors represent the orientation of the fracture surface in the sample coordinate system (*physical orientation*). The color map (b) is the standard stereographic projection of an orientation hemisphere. (d-e) Two further perspectives on the fracture surface of VST55531 that emphasize how a change in color corresponds to a change of the physical crack plane. The dashed line corresponds to the cross-section shown in figure 5.2d. The coordinate system shown to the right relates the orientation of Beta21S to the texture plot in figure 5.12.

h, i and c). Some grain arrangements seem quite effective in delaying crack growth (e.g. grain j or g) . The case of the grains labeled j, k and e on figure 5.7b is worth being described in detail as it shows how the crack front adapts itself to variations in cracking resistance. Slow growth rates are observed in j with a fracture surface which is not parallel to a specific crystallographic plane (see figure 5.6). Meanwhile, the crack propagates faster in the neighboring k where the crack is oriented close to a {112} plane. This induces a rotation of the crack front towards grain k. The crack

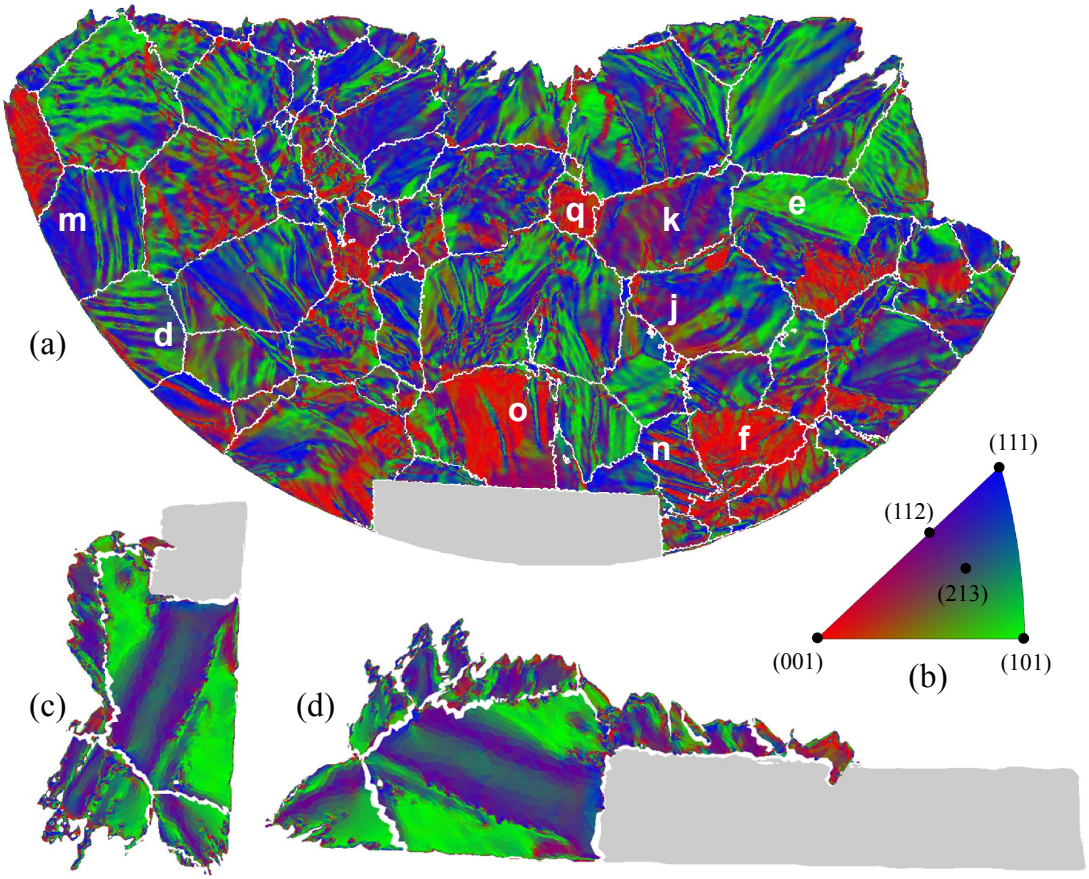

Figure 5.6: (a,d) View along the loading axis on the fracture surfaces of Beta21S and VST55531, respectively. White lines indicate intersections of the crack with the grain boundaries. The triangle colors represent the *crystallographic orientation* of the fracture surface in the corresponding grain as defined on the color map/stereographic triangle (b). The positions of the slip planes reported for bcc {101}, {112}, {213} are labeled. (c) Additional perspective on the fracture surface in VST55531.

finally enters grain e from the two above mentioned grains (j and k) and the part of the crack front coming from grain k enters grain e along a favorably aligned {101} plane and forces the part of the crack front coming from j to eventually propagate on that plane. The result of this complex process is an acceleration of crack growth within grain e (figure 5.7b), when the crack plane changes from non crystallographic to crystallographic. The crack further accelerates when it enters the next grain (l) where cracking also occurs on two crystallographic {112} and {101} planes. It is worth mentioning that the change in direction observed in e (figure 5.5) and explained in the previous paragraph corresponds to the intragranular change in direction highlighted by an arrow on figure 5.2. This illustrates clearly why the details of the interactions of short

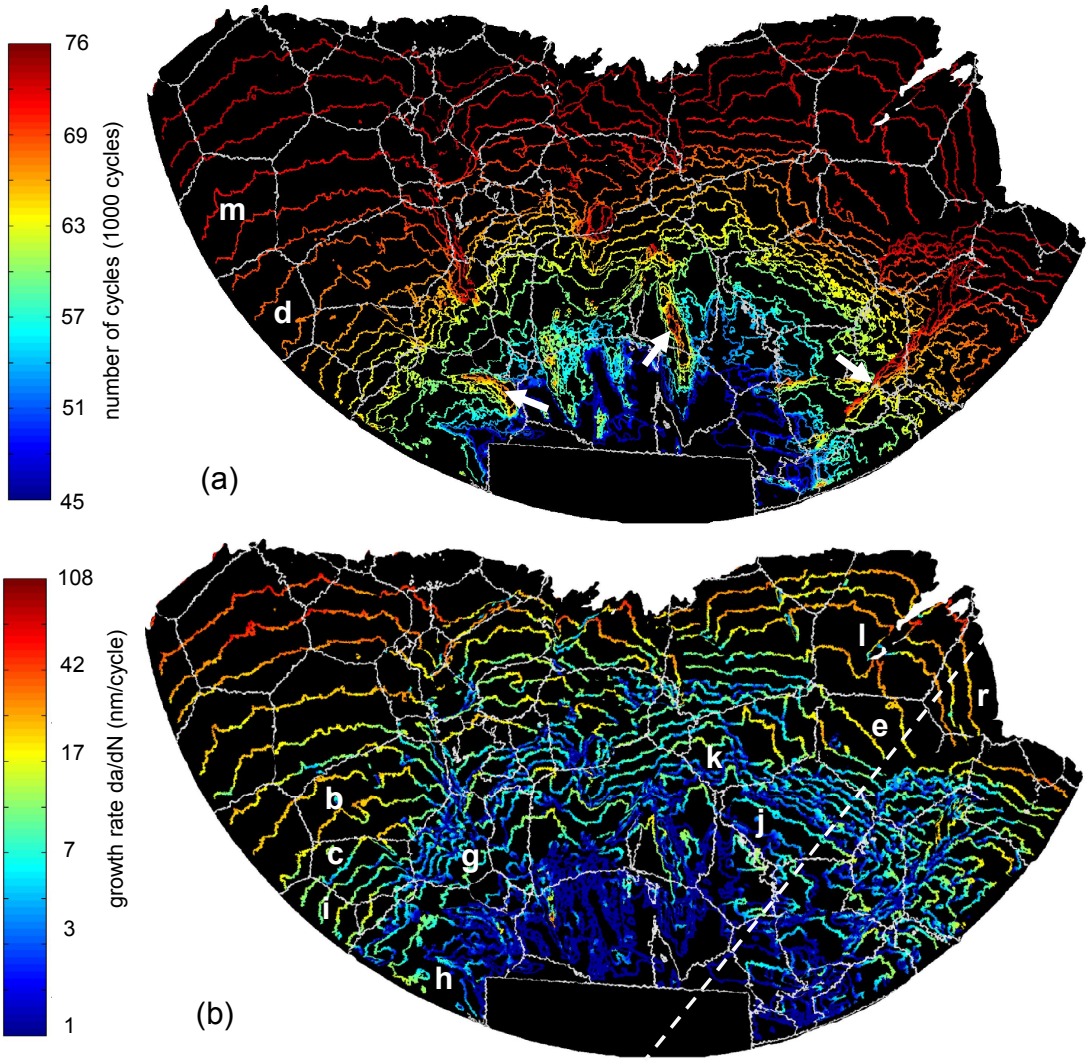

Figure 5.7: 3D rendering of the crack evolution within the Beta21S sample during the fatigue test. The grey lines indicate intersections of the crack with grain boundaries. a) Position of the various crack fronts with a color code varying with the number of fatigue cycles. b) Local growth rate da/dN shown with a logarithmic color code. Along the dashed line the 2D growth rate visible in figure 6.14 was plotted.

cracks with grain boundaries cannot be fully elucidated unless the temporal evolution of the 3D crack front can be analyzed together with the surrounding grain structure.

The data shown on figure 5.7b can be used to produce a map of the average crack growth rate for each grain crossed by the crack, as shown in figure 5.8. It clearly shows that the crack globally accelerates as it moves away from the notch. For the latest stages of growth observed, the crack front crosses around ten grains but the crack growth rate

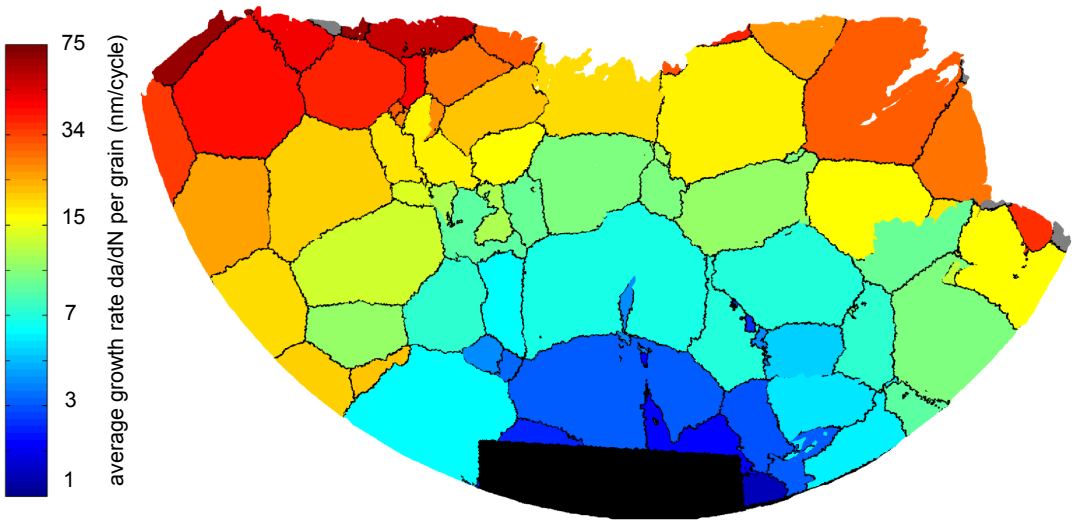

Figure 5.8: Average crack growth rate for each individual grain crossed by the crack, which was grown at a constant load amplitude.

is still not uniform and varies from 6 nm/cycle to 82 nm/cycle. It also appears, when looking at figure 5.8 that, for a given crack length, the average crack growth rate on the left hand side of the specimen is higher than on the right hand side.

The dependence of the mean crack growth rate on the mean crack length is shown in figure 5.9. The mean da/dN represents the average of the local growth rate at a given propagation stage N or mean crack length a. The mean crack length was calculated by first, calculating the average growth distance during each growth interval measured, and second, successively summing up these average growth distances up to a certain propagation stage. The linear plot makes it possible to compare scatter directly. Figure 5.9a shows that relative fluctuation of the average growth rate tend to decrease with increasing crack length. However, the standard deviation of the growth rate at a certain crack length increases with increasing crack length. Plotting the mean growth rate over the crack length on a double logarithmic scale (figure 5.9b) shows, despite of the scatter, an almost linear relation between the values.

5.1.8 Pole Figures

Schmid Factor Figure 5.10 compares the distribution of the poles of grain e in figure 5.6 with the calculated Schmid factors as detailed in section 4.6. Around the $(0\bar{1}1)$ slip plane that has by far the highest Schmid factor no particularly high density of poles is visible. However, around the (101) plane whose calculated Schmid factor is half as high a significant accumulation of poles is visible. This missing correlation between calculated activity of a slip plane and crack plane is the general case, meaning that the number of cases where the most activated slip plane (as calculated) corresponds to the

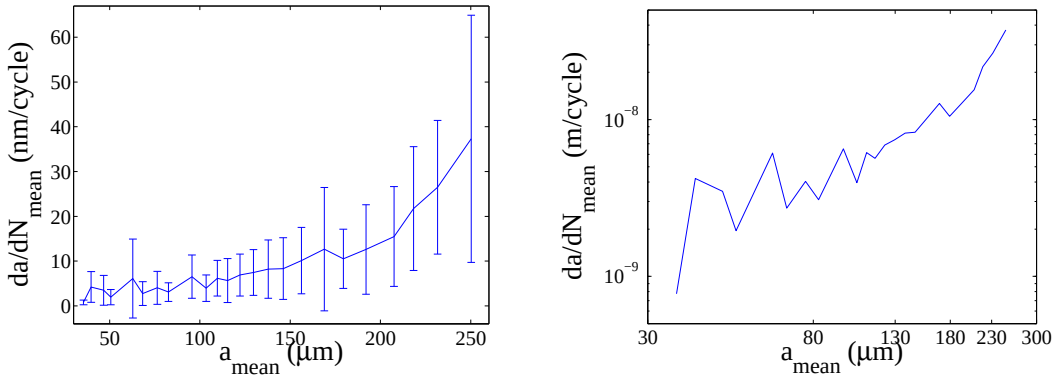

(a) (b)

Figure 5.9: Plot of average growth rate $\frac{da}{dN}$ over the average crack length a. (a) Linear scale with standard deviation represented by error bars. (b) Same data plotted on double logarithmic scale.

crack plane is smaller than the number of cases where there is a match.

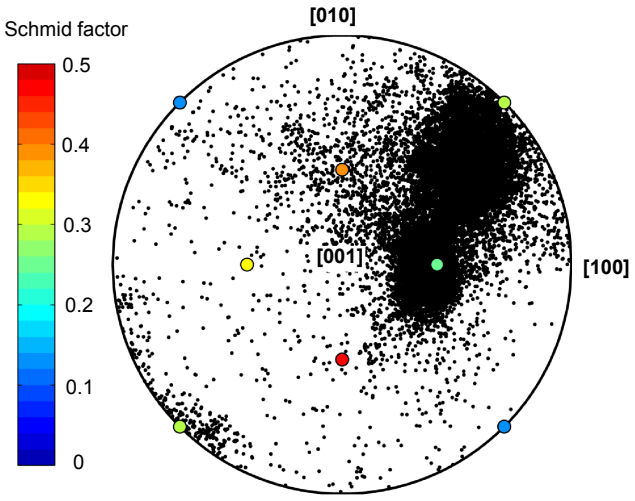

Figure 5.10: Pole figure showing the distribution of the crystallographic normals of the fracture surface observed within grain e (see figure 5.6). Values of the Schmid factors for the different {101} planes are given with a color scale indicated on the left, assuming an uniaxial stress state in the grain. The Schmid factor plotted is in each case the higher one of the two slip systems belonging to the plane.

Pole Density Distribution In order to create figure 5.11 a more advanced tool was used to plot not only the distribution, but also the density distribution of the crystallographic poles of the fracture surface. Several differences between the two alloys are immediately visible. In the case of Beta21S the poles are more homogeneously spread. The lowest density measured is about 0.75 the highest 1.6 while the poles in VST55531, where the densities vary between 0 and 4.5, are much more concentrated on certain planes. Apart from the densities the distribution patterns are also completely different in the two samples. VST55531 shows a peak close to (101) and a higher

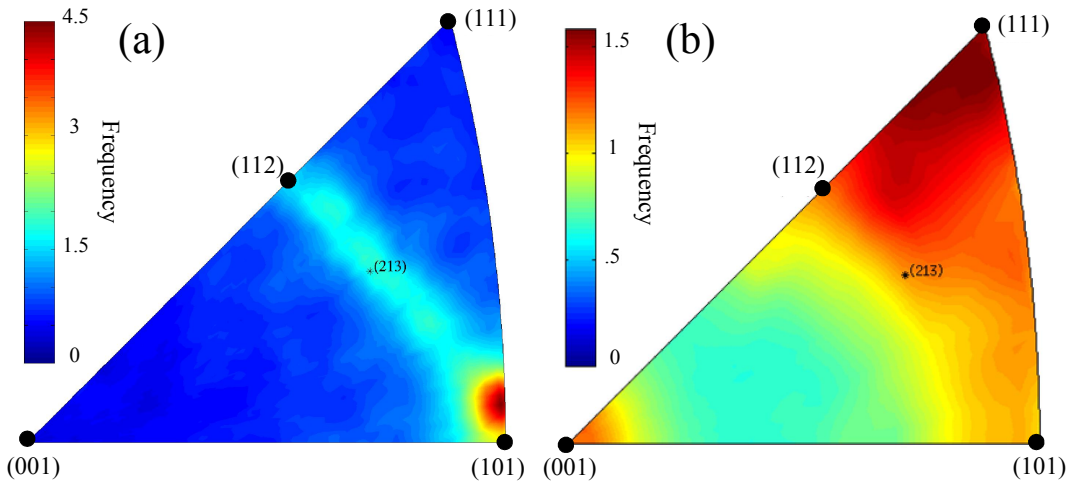

Figure 5.11: Crystallographic pole density distributions of the whole fracture surface in (a) VST55531 and (b) Beta21S.

concentration on a line between (101), (213) and (112). Beta21S exhibits only moderate pole density around (101). The highest measured densities are in a triangle between (111), (112) and (213). Another significant peak in density is visible around (001).

Micro Texture The pole figures shown in figure 5.12 demonstrate a further information that can be accessed from a DCT dataset. The same tool that was used for the pole density distributions was used, this time applied to visualize the density distribution of the {100}, {101} and {111} poles of the about 1000 grains in the Beta21S sample. The poles were not weighted by the volume of their corresponding grains. The micro texture of VST55531 being based on about 400 grains shows too much scatter to be meaningful.

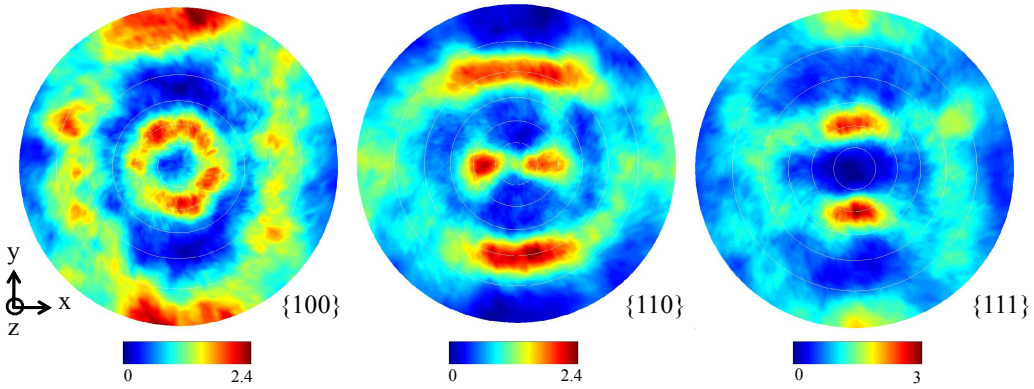

Figure 5.12: Pole figures showing micro texture of Beta21S [King et al., 2010].

Grain boundary orientations The pole density distribution plots can also be used to investigate grain boundary orientations [King et al., 2010]. The 3D grain boundaries can be converted into a mesh and their crystallographic orientation can be plotted in a pole figure. The comparison of the orientation of grain boundaries as reconstructed from DCT (using the state of the art reconstruction) with the more precise grain boundaries as extracted from the PCT volume was evaluated and showed that the currently achievable accuracy of DCT reconstruction is not precise enough (deviations of up to 15°) to give reliable information on local grain boundary curvature and orientations (see figures 5.13 and 5.14).

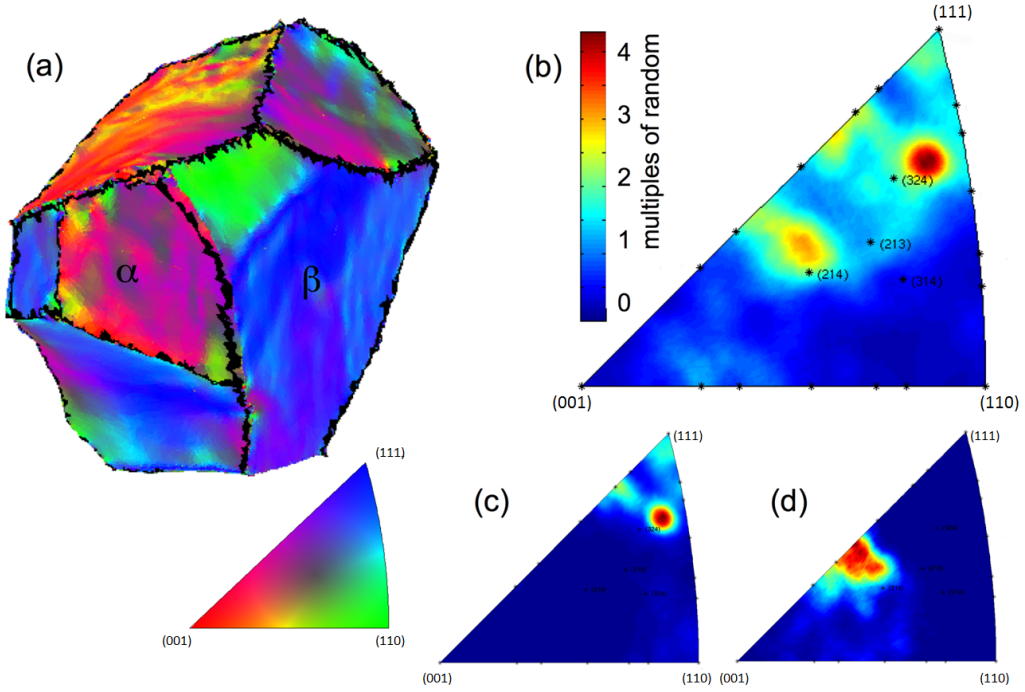

Figure 5.13: (a) Grain colored according to crystal plane of boundary. (b) Pole figure of crystal plane of boundary for whole grain. (c and d) Pole figures from single grain boundaries marked α, β in (a).

5.2 SEM, FESEM

The SEM characterization was performed on both alloys. In the case of Beta21S additionally FESEM was performed in order to investigate features that were below the resolution of the SEM. The comparison between figure 5.15a and b shows that the fatigue crack in Beta21S deviates much less from the plane perpendicular to the loading axis than in VST55531. On the SEM micrographs the crack in VST55531 appears much more faceted than in Beta21S. In the region ① of figure 5.15a the crack seems to grow

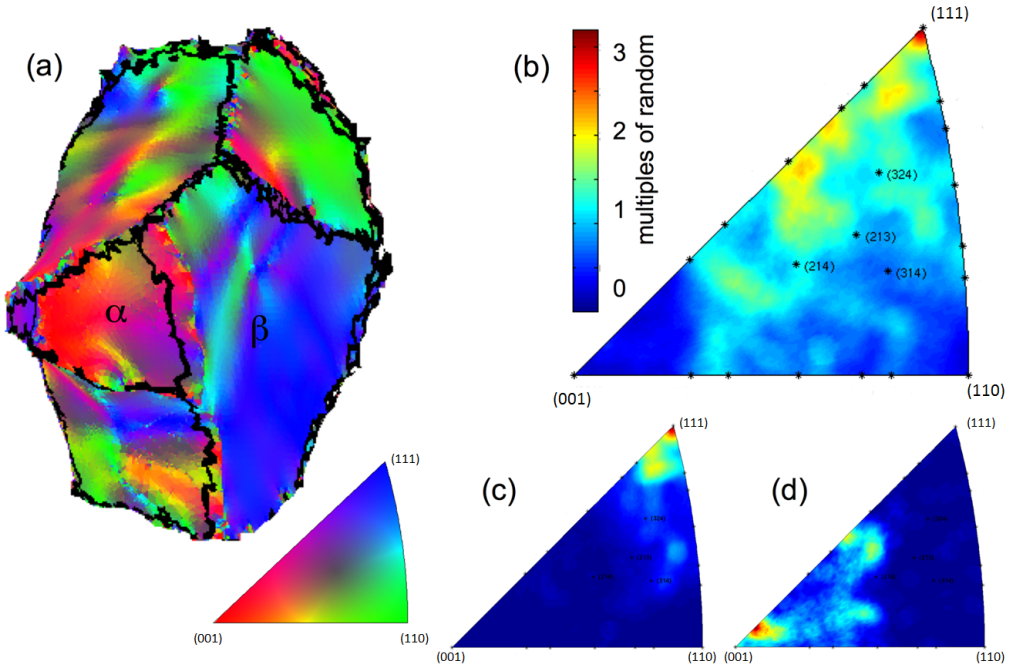

Figure 5.14: As for figure 5.13, but using the grain shape determined from PCT data.

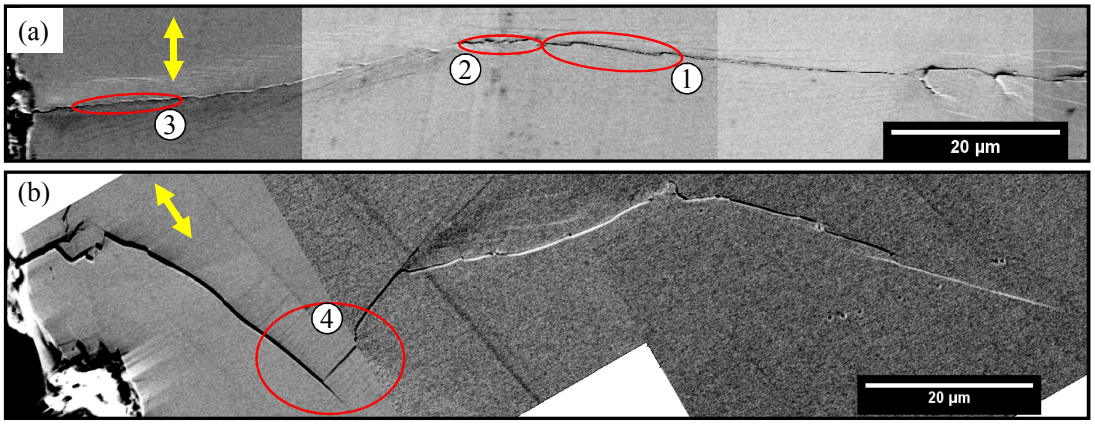

Figure 5.15: SEM micrographs of a fatigue crack in (a) Beta21S and (b) VST55531. The yellow arrows mark the loading direction. The images were acquired at an acceleration voltage (EHT) of 5.00 kV and a working distance (WD) of 9 mm.

on two alternating planes, in region ② it seems to do smooth undulations and in region ③ it seems to grow almost straight. The FESEM magnifications shown in figure 5.16 confirm in the case of ① that the crack propagates on two alternating planes. ② shows that what was thought to be smooth undulations are combinations of straight lines

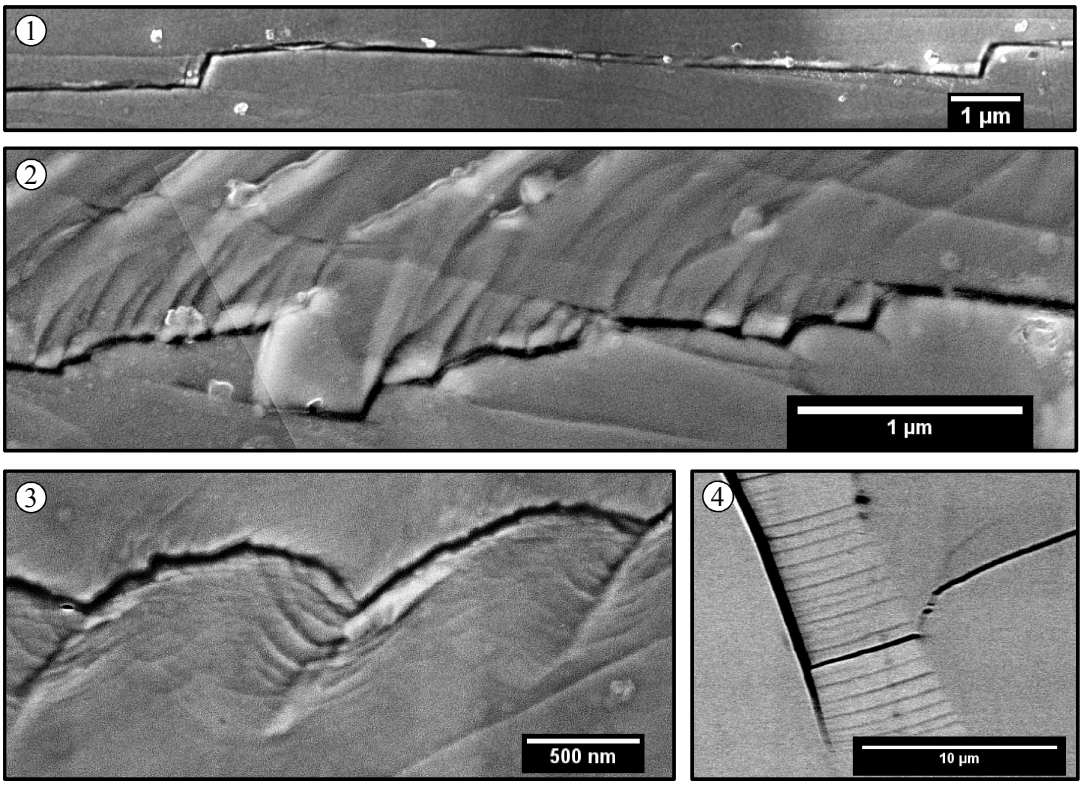

Figure 5.16: ①-③ FESEM micrographs showing magnifications of 3 positions of the crack in figure 5.15a (Beta21S). ④ SEM micrograph showing a magnification of a position in 5.15b (VST55531). ① and ② were done at an EHT of 5.00 kV and a WD of 4.6 mm, ③ was done at an EHT 2.00 kV and a WD of 4.0 mm, ④ was acquired at an EHT of 5.00 kV and a WD of 9 mm.

and sharp kinks at higher resolution. The magnification of ③ indicates that growth probably still occurs on a combination of planes but even at this resolution the facets cannot clearly be resolved. The FESEM magnifications reveal that the crack is faceted in both alloys but the changes of the crack plane are more frequent in Beta21S than in VST55531. The magnification shown in ④ gives a good example for the slip lines on two different slip systems that are typical for stage I.

5.3 EBSD

The inverse pole figures of the Beta21S sample before and after the fatigue experiment are shown in figure 5.17. At the angular and spatial resolution achieved in this measurement no color gradient and no isolated points of different orientation can be detected within the grains. That means that within the grains there is no strong orientation gradient and that there is no different phase then β above the resolution (2.0x2.0 μm^2).

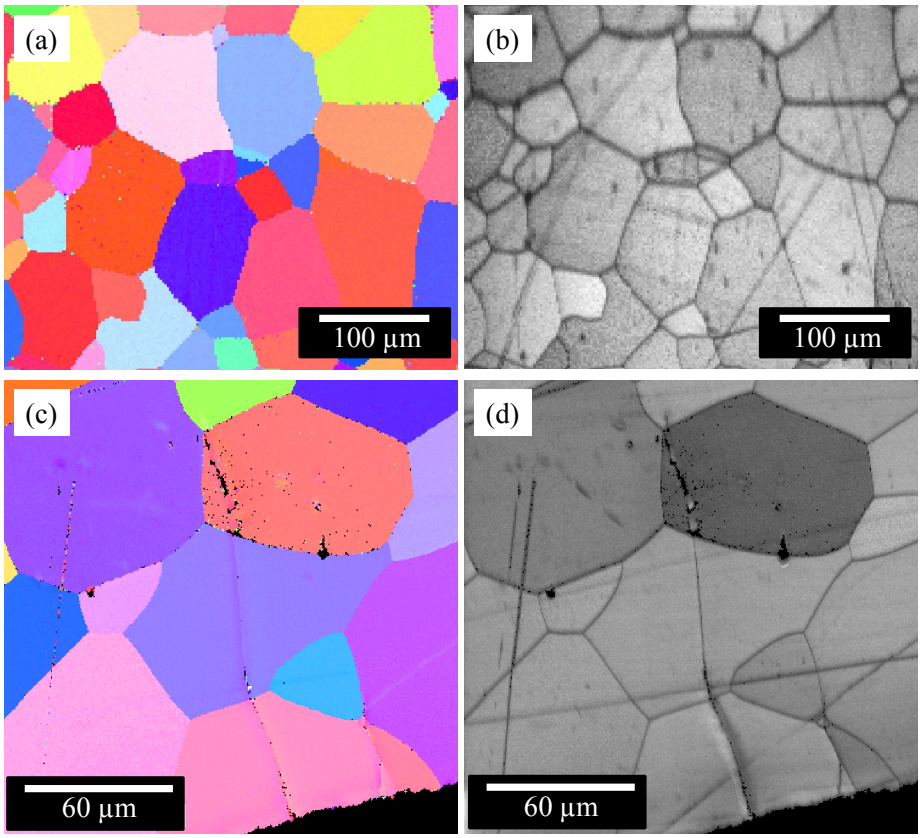

Figure 5.17: EBSD micrograph of Beta21S before (a,b) and after the fatigue experiment (c,d). (a,c) Inverse pole figure coloring, (b,d) image quality maps. The crack in (c,d) is the same as depicted in figure 5.15a.

The image quality map (figure 5.17 b, d) is bright what indicates that all points measured could be accurately assigned to an orientation. Also after the fatigue experiment no martensite could be detected in proximity of the crack (figure 5.17 c,d) at a resolution of 0.5x0.5 μm^2.

5.4 XRD

Figure 5.18 shows two diffraction patterns measured on the same sample of Beta21S after a fatigue experiment, once at the position of the notch, containing a 40 μm crack and once at a polished part on the shoulder of the fatigue sample where cracking did not occur. At the notch the pattern clearly contains additional peaks at about 2, 3.5 and 14 degrees (2θ). However, these additional peaks do not correspond to peaks observed in previous studies of stress induced martensite [Duerig et al., 1982; Kim et al., 2007; Yang et al., 2009]. These peaks can possibly be attributed to the formation of a gallium

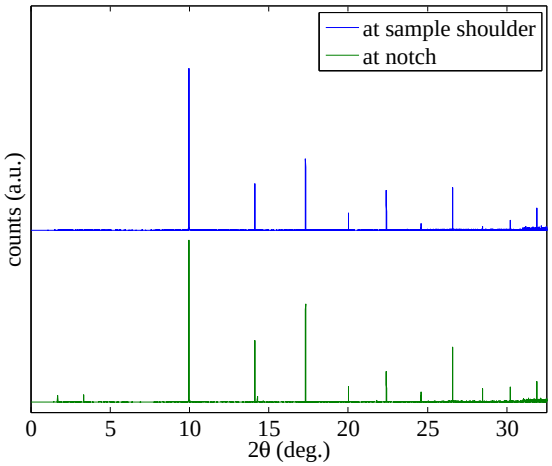

Figure 5.18: Synchrotron X-ray powder diffraction pattern of Beta21S collected at λ = 0.3999 Å

phase, created during the FIB milling of the notch, as detailed in the discussion.

5.5 IXS

The elastic constants as calculated from the inelastic X-ray scattering experiment on Beta21S were C_{11} = 153 GPa, C_{12} = 101 GPa and C_{44} = 57 GPa. The resultant directional dependence of the Young's modulus is illustrated in figure 5.19. The density used for the calculations was 5.236 g/cm^3. The equivalent compliance constants are S_{11} = 1.38 x10^{-2} GPa^{-1}, S_{12} = -0.55x10^{-2} GPa^{-1} and S_{44} = 1.75x10^{-2} GPa^{-1}. From those values the calculated poisson number ν and Young's modulus E are 0.33-0.35 and 104-119 GPa, respectively, depending on the model used for the calculation (Voigt, Reuss or Hill) [Collings, 1986].

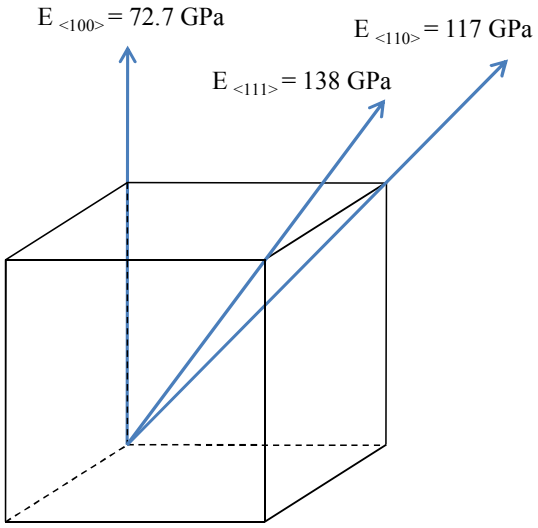

Figure 5.19: Directional dependence of Young's modulus in Beta21S

Chapter 6

Discussion

6.1 Material Choice

The aim of this study was to investigate the interaction of SFCs with grains in 3D. DCT is a particularly well suited technique as it provides the 3D shape and orientation of polycrystalline aggregates in a non destructive way. At the time the 3DXTSM experiment on Beta21S was performed, the accuracy of 3D grain boundary maps produced by DCT was still unknown. In order to be able to evaluate this uncertainty the metastable beta Ti alloy Beta21S was selected. In this material a heat treatment can be performed to decorate grain boundaries with alpha (hcp) precipitates. Those precipitates can be visualized in 3D using PCT [Dey et al., 2007] and this can be used to precisely map the position of grain boundaries. Thereby, the method DCT could be evaluated and for the case that the position of the grain boundaries would have been incorrect, only the grain orientation could have been taken from DCT, while the exact grain boundaries should be taken from the PCT data set. For this reason the rather complicated alloy Beta21S[1] was used for the first investigations. A comparison between the shape of grains obtained by DCT and by PCT carried out on the specimen after the fatigue test, showed that the average error in the grain boundary position determined by DCT was of the order of 2-3 micrometers, for an average grain size of 55 μm (section 6.3.1). This accuracy was deemed satisfactory and the high resolution PCT validation data, although slightly more accurate, were not used for the analysis carried out here.

The second material system VST55531 was selected for reasons of comparability and to simplify data interpretation. By choosing a near beta titanium alloy the microstructure is as similar as possible while the occurrence of stress-induced martensitic transformation (SIMT) can be very likely excluded, as detailed in section 6.2. By air cooling the omega precipitates are in the right size to cause pronounced planar slip. And increasing the grain size gives the crack the possibility to stay longer on a slip plane, creating bigger facets that can easier be resolved.

[1] possibility of SIMT

6.2 Stress-Induced Martensitic Transformation

Haicheng and Shujuan [Haicheng and Shujuan, 1990] reported that a heat treatment for 2 hours at 850 °C with subsequent quenching in water makes the metastable beta titanium alloy Ti-10V-2Fe-3Al sensitive to SIMT . They describe that in this condition the SIMT causes a crack closure effect and branchings and tortuosities of the fatigue crack. A very similar heat treatment was done with the metastable alloy Beta21S in order to adjust the grain size for this study. SIMT is reported to already happen at stresses as low as 150 MPa [Welsch et al., 1994]. Our fatigue experiments were done at tensile loads between 10 and 320 MPa. Due to stress concentration the local stress at the crack tip will be even higher. We can therefore not exclude that this transformation also occurs in the case of our Beta21S sample. The volume change of about +0.7 % which goes along with the transformation from β to α" (values for Ti-10V-2Fe-3Al [Duerig et al., 1982]) would cause a local compressive stress. A strong local change in the stress field would influence the crack growth direction and would unnecessarily complicate simulations on the data set.

SIMT is reported to happen on very different length scales. Haicheng describes structures [Haicheng and Shujuan, 1990] that cross grains of about 200 μm grain size and are clearly visible as tilted planes in an optical microscope. Li [Li et al., 2008] observed 50 nm thick α" martensite plates using TEM. The occurrence of SIMT is influenced apart from the applied stress by at least two further parameters:

- Material's composition: SIMT happens only in systems with a martensitic start temperature M_s near room temperature [Duerig et al., 1982].[2] It is a material constant only dependent on the composition. Neelakantan et al. [Neelakantan et al., 2009] give a formula to calculate M_s for beta titanium alloys in Kelvins.

$$\begin{aligned} M_s = \; & 1156 - 150\ Fe_{wt:\%} - 96\ Cr_{wt:\%} - 49\ Mo_{wt:\%} \\ & - 37\ V_{wt:\%} - 17\ Nb_{wt:\%} - 7\ Zr_{wt:\%} + 15\ Al_{wt:\%} \end{aligned} \tag{6.1}$$

- Cooling rate: The SIMT is enhanced by rapid cooling and the triggering stress for SIMT is lowered.[3]

The occurrence of SIMT was only investigated for Beta21S. In the VST55531 material system used here SIMT does not happen for two reasons. First, because according to

[2] M_s is the temperature to which an alloy has to be quenched in order to develop 1 % martensite [Gottstein, 2007].

[3] Solid state thermal phase transformations require diffusion when the phases have different elementary compositions, which is the normal case for alloys. These phase transformations can be impeded by rapid cooling which leaves the atoms not enough time for diffusion. A phase is called metastable when it exists at a certain temperature although another phase is thermodynamically preferred. The further away an alloy is from its thermodynamic equilibrium the higher is its driving force for a martensitic phase transformation [Gottstein, 2007]. The higher the cooling rate, the less diffusion can occur, the less stable is an alloy, the higher is its driving force for martensitic transformation, the more likely it is that martensite develops during cooling and the lower is the triggering stress for SIMT after cooling.

Plane	{101}	{020}	{002}	{111}	{021}	{112}	{022}	{200}	{130}
2θ (°)	8.92	9.36	9.89	10.2	10.5	13.4	13.6	15.2	16.0

Table 6.1: 2θ values of the α" phase in the Ti-10V-2F-3Al [Duerig et al., 1982] for $\lambda = 0.400$ Å.

formula 6.1 and the compositions given in table 5.1 VST55531 has a M_s of 241°C which is about 100°C further away from room temperature than the one of Beta21S (142°C). And second, because Beta21S was water quenched while VST55531 was air cooled. For these reasons the driving force for SIMT will be lower in VST55531 than in Beta21S and we can (very likely) exclude the occurrence of SIMT in our VST55531 samples.

Duerig and Bhattacharjee [Duerig et al., 1982; Bhattacharjee et al., 2005] investigated the occurrence of SIMT on the surface of Ti-10V-2Fe-3Al. After a tensile test with 5% strain the phase transformation is visible in light microscopy micrographs as long, mostly parallel stripes crossing the whole grain. But proving that SIMT happens during such tensile tests doesn't prove that it happens during a high cycle fatigue tests where the strain is much smaller. Since the triggering stress for SIMT might only be exceeded at the crack tip this region must be investigated more locally. EBSD measurements were performed around the crack tip before and after a fatigue experiment on Beta21S. The results of this study are illustrated in figure 5.17.

The beam size of the EBSD measurement for figures 5.17 (c,d) was only 0.5x0.5 μm^2; the SEM images indicate no morphology change of the surface around the crack (figures 5.15 and 5.16). This seems to indicate that no α" phase bigger than 1 μm is present around the crack.

Since the EBSD experiments exclude macroscopic α" but not the occurrence of very fine α" an XRD experiment was performed. This technique has been used by other researchers to evidence SIMT [Yang et al., 2009; Kim et al., 2007].

All the peaks in the diffraction pattern visible in figure 5.18 in the sample shoulder can be assigned to β titanium [Burgers and Jacobs, 1936]. The additional peaks in the XRD pattern measured around the notch at about 2°, 3.5° and 14° 2θ can't be assigned to that phase. No correlation could be found between the additional peaks and the 2θ angles of α" given in table 6.1. Also the slightly different angles for α" measured by [Yang et al., 2009; Kim et al., 2007] in different metastable β titanium alloys don't match our pattern. In general the lattice parameters of α" titanium seem to change only moderately with the alloy's composition so we can exclude that the additional peaks measured around the notch can be related to α". The pattern also can't be identified as α titanium [Szanto, 1955]. That leads to the assumption that the additional peaks in figure 5.18 measured around the notch represent pure Ga or phases containing Ga. Ga was used to FIB mill the notch. We know that the phases are crystalline since they produce sharp lines in the diffraction pattern. The ion implantation itself can't be expected to produce a crystalline phase. But the elevated temperatures during FIB milling might have given the atoms enough mobility for the formation of a crystalline phase by diffusion. However, the additional peaks neither correlate with the XRD pattern of pure Ga [Sharma and Donohue, 1962] nor with the ones of GaTi [Schubert

et al., 1962]. We cannot identify the additional phase at the notch but we can conclude that it is not α".

To conclude, the occurrence of SIMT in Beta21S can be excluded at macroscopic length scales. Although Beta21S should contain at least some thermal martensite since it was quenched to below M_s no evidence for that could be found. Neither the XRD nor the EBSD or FESEM measurement showed evidence for the existence of martensite. An additional phase at the notch could not be identified. It could still be that there are α" in quantities below the resolution and sensitivity limit of the methods used. However, such small quantities can not be expected to have significant influence on the crack propagation behavior.

6.3 Method Optimization and Evaluation

6.3.1 Accuracy of DCT

Fig. 6.1 shows a section through the DCT grain map with the boundaries segmented from the PCT volume (heat treated for visibility of the grain boundaries, see section 3.6) as an overlay. The accuracy of the 3D grain shapes determined by DCT was quantified by comparing the volumes on a grain-by-grain basis. First, a 3D Euclidean distance transform was applied on the grain outline of a PCT grain. Then, this volume was multiplied with the binary outline of the same grain from the DCT map. The values of this intersection represent the closest distance between the two outlines, or alternatively the error of DCT. The average error in the DCT grain outlines was found to be 2.6 μm (4.7 voxels in the PCT map, corresponding to 1.9 voxels in the DCT grain map). Some of the large errors appearing in figure 6.1 might correspond to grain boundaries being oriented almost parallel to the 2D cross-section. For those grain boundaries small shifts normal to the grain boundary plane will be visible as strong deviations in the 2D section.

The validation of the DCT grain map by this method relies on the precision of the grain boundary network segmented from PCT. Errors in this segmentation will influence the result of this validation. Even when considering the errors from the acquisition and reconstruction of the PCT volume to be negligible, the errors due to the image processing have to be discussed. During the alignment and scaling of the volume some aliasing errors are introduced due to the voxelated nature of the data, but the effect of these errors should be small. Error sources of probably higher impact are the non-decorated grain boundaries, which were not segmented due to the absence of precipitates, and the grain boundaries close to the surface that were hardly visible because their contrast was superimposed by the strong phase contrast between sample and surrounding air. These invisible boundaries are restored by the watershed algorithm and represent less than 5 % of the total boundary area. Therefore errors introduced are not expected to have a significant effect on the final results.

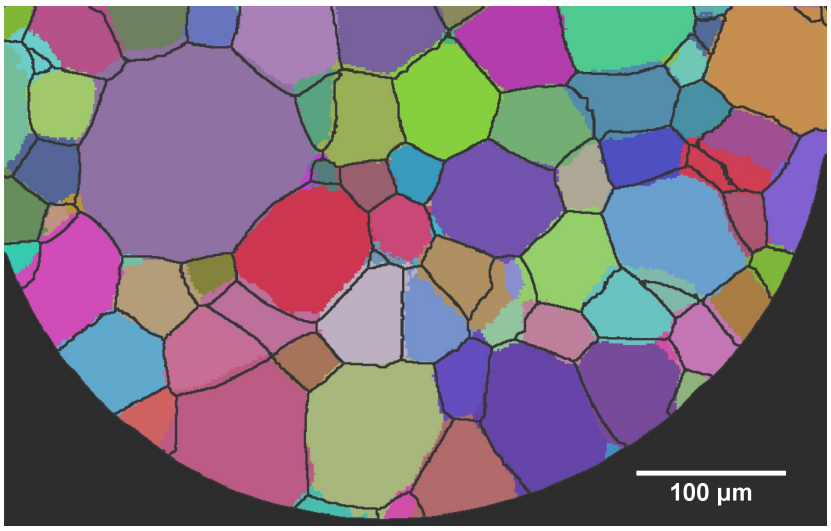

Figure 6.1: Cross-section through the DCT grain map showing the grain boundaries as extracted from the heat-treated PCT volume in black.

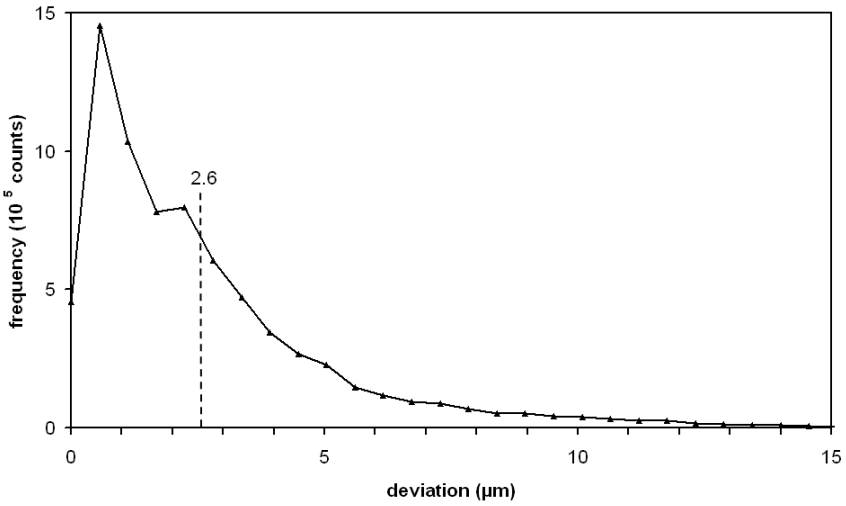

Figure 6.2: Histogram of the deviation in the grain boundary locations between the PCT and DCT data.

6.3.2 Optimization of Imaging Conditions

Figure 6.3 illustrates the effect of several imaging parameters on the image quality as measured on the VST55531 sample, mounted in the fatigue machine.

Number of projections The number of projections, i.e. the number radiographs used for image reconstruction, has a significant influence on the crack visibility. A

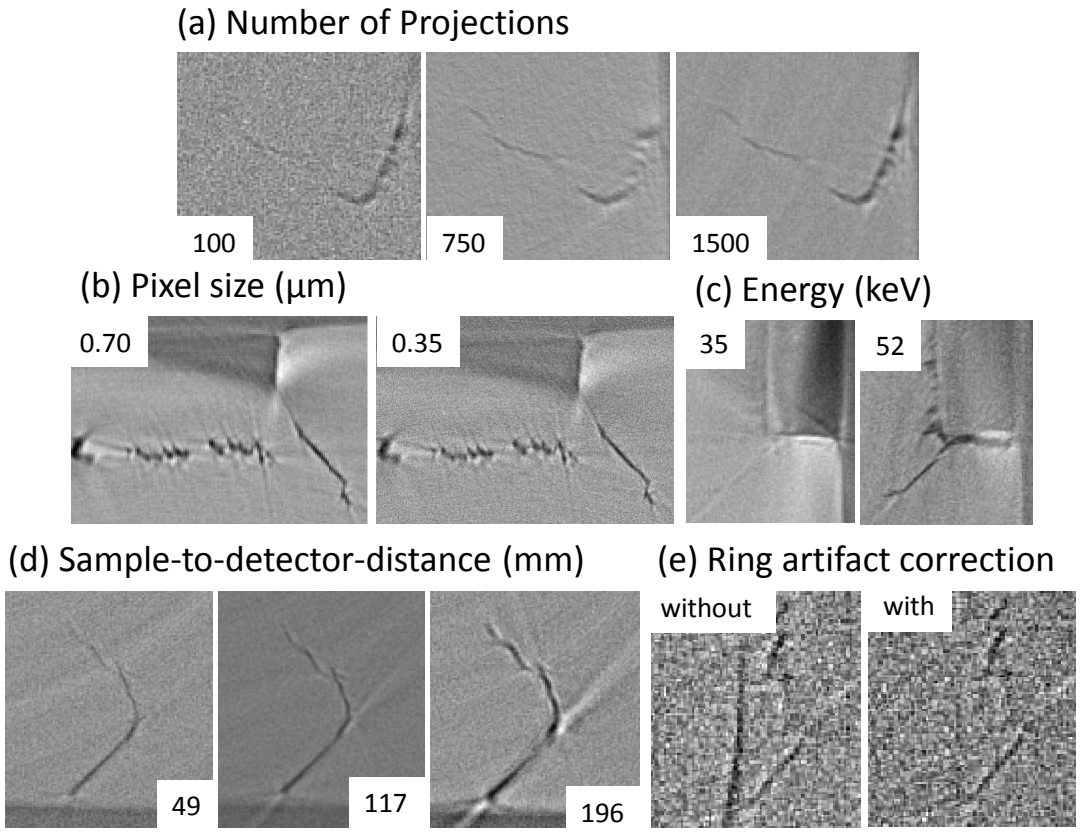

Figure 6.3: Influence of different imaging conditions, reconstruction types and image filters on the image quality. Each time only one parameter is varied.

rule of thumb [Kak and Slaney, 2001] states that the necessary number of projections $N_{projections}$ is related to the number of the detector elements (number of pixels on the detector) N_{pixels} in the following way:

$$N_{projections} \geq \frac{\pi}{2} \cdot N_{pixels}. \tag{6.2}$$

A lower number of projections will result in a poor visibility of the crack and in more reconstruction artifacts. A higher number doesn't yield much further improvement of the image quality, so numbers above the optimum value result in unnecessary long measurement times and produce unnecessary amounts of raw data. As visible in figure 6.3a at least 1500 projections are necessary to resolve the crack measured at 0.7 μm pixel size acceptably.

Pixel size According to equation 6.2 halving the pixel size (which means increasing N_{pixels} by a factor of four), goes along with doubling the number of projections needed. Further, the exposure time per radiograph has to be increased by a factor of four

since the number of photons per pixel scales with the square of the pixel dimension. Decreasing the pixel size by a factor of two means therefore increasing the measurement time by a factor of eight. When reconstructing 3D objects the size of the reconstructed volumes V is related to the pixel size p by a power law: $(\frac{1}{p})^3 \propto V$. Measuring the same object at half the pixel size means increasing the size of the reconstructed volume by a factor eight. Correspondingly, data storage, handling and processing will involve more effort. Therefore, the pixel size should only be reduced when really necessary. Figure 6.3b shows the reconstruction of the crack at a distance of 49 mm at 52 keV using 3000 projections once reconstructed using 0.35 μm and once using 0.7 μm pixel size. Not much additional information can be gained in the case of VST55531 using the higher resolution. Very likely the mechanical inaccuracies of the rotation stage limit the 3D resolution in this case. The weight of the fatigue machine (5 kg) is a problem since it increases the wobble. A small diameter, light weight fatigue machine would improve this. With the current hardware it is not worth the effort to work with a pixel size smaller than 0.7 μm. Another factor that limits the image quality and thereby makes the segmentation less accurate seem to be reconstruction artifacts (black and white lines). Part of them are caused by a too pronounced phase contrast and might slightly be improved by increasing the number of projections. In cases like the one encountered for Beta21S, where the crack stays less long on a plane the gain using a smaller pixel size could potentially be significant. For such cases it should be considered in future to measure at least the final volume where the mesh is created from at a higher resolution, for example by means of X-ray projection microscopy [Mayo et al., 2002; Mokso et al., 2007].

Energy The energy (and accordingly the wave-length) of the incident monochromatic beam influences mainly three things: the absorption, the phase contrast and the resolution. At higher energies the beam is less absorbed which means that it also interacts less with the sample and the exposure time has to be correspondingly increased to obtain the same signal to noise ratio. Additionally, the phase contrast gets less pronounced at higher energies. This can be compensated by increasing the sample-to-detector-distance. Further, using higher energies will widen the point-spread-function[4] of the detector system, because the path length of secondary electrons and X-ray photons in the scintillator increases, which blurs the image (decreases the resolution). The reconstruction in figure 6.3c was obtained using 750 projections and a pixel size of 0.7 μm at a sample-to-detector distance of 49 mm, which is the minimum possible with the fatigue machine. When measuring at 35 keV the phase contrast is too strong and creates artifacts because the fringes from different objects superimpose. Increasing the energy to 52 keV is necessary to reduce the artifacts but involves an increase of the exposure time from 0.15 s to 1 s per projection ($\approx$ a factor of seven). As visible in figure 6.3c the influence of the energy on crack visibility can be tremendous. This particular example might be mostly explained by vanishing values of the contrast transfer function

[4]The point-spread-function describes the measured intensity distribution created by a point-like photon source.

for specific ratios between distance and energy.

Sample-to-detector-distance Figure 6.3d illustrates the effect of the sample-to-detector distance x, as defined in figure 3.5, on resolution and phase contrast. The images were recorded at 52 keV, 0.7 pixel size using 1500 projections. The shorter the distance, the higher the resolution but the less the phase contrast. The artifacts caused by too strong phase contrast are clearly visible at 196 mm and 117 mm. A distance of 49 mm strongly reduces such artifacts but they are still strong enough to cause problems during segmentation. There is a compromise to be found between visibility of the crack and strength of artifacts.

Ring artifact correction Variations of the beam profile (mainly due to the thermal drift of the multilayer monochromator) and a non linear behavior of the scintillator (due to scratches or dust on it) cause ring-shaped artifacts in the reconstructed images. Those can be removed using ring-removal algorithms as shown in 6.3e. An impact on the contrast of the crack was not visible. Since the algorithm involves a high computational effort it should only be used in cases where strong ring artifacts superimpose with the crack. This can usually be avoided by shifting the sample to a position with homogeneous beam profile.
The picture created at a pixel size of 0.35 μm shown in 6.3b shows the best image quality we could achieve when scanning the sample in the fatigue machine. The artifacts are still strong. Ideally, we should have used a shorter distance at 35 keV and 0.35 μm pixel size. The artifacts are the limiting factor if the sample shall be measured at a higher resolution. If they were reduced also the segmentation of lower resolution data would be more reliable and easier. The artifacts that are caused by too pronounced phase contrast could be reduced and the contrast homogenized by phase retrieval algorithms like the one by Paganin [Paganin et al., 2002] or holotomography [Cloetens et al., 1999; Guigay et al., 2007; Langer et al., 2010]. But those also blur the image by at least one pixel which doesn't help to increase resolution. Another promising approach for the future to reduce artifacts when the sample-to-detector distance can't be reduced is using a phase removal algorithm [De Witte et al., 2009].

However, the most effective solution would be the use of a smaller fatigue machine, allowing for shorter sample-to-detector distances. Like this it would be possible to adjust the amount of phase contrast. The energy could be reduced to an optimum of the contrast-transfer-function at this new minimum distance which would reduce exposure time. A reduced weight would decrease the wobble of the sample. This increases spatial resolution and reduces the artifacts in the reconstructed images.

A good compromise between measurement time, resolution and contrast when measuring the sample mounted in the fatigue machine are 1500 projections, 0.7 μm pixel size, 49 mm sample-to-detector distance and an energy of 52 keV.

6.3.3 Oversampling

Figure 6.4a shows a cross-section through the PCT reconstruction of Beta21S. Segmenting the crack in this condition will produce a coarse binary volume which does not preserve all the morphological features that are visible for the human eye in the gray-scale volume (figure 6.4b). This is because the size of the features that can be preserved is limited by the voxel size. This loss of information during segmentation can be reduced by artificially decreasing the voxel size (oversampling) using an interpolating algorithm. Figure 6.4c shows figure 6.4a after oversampling by a factor three. Although the picture looks smoother it contains no additional information. It doesn't contain any features that were below the resolution of the experiment. Nevertheless, segmenting the crack in this condition will much better preserve fine morphological features (figure 6.4d).

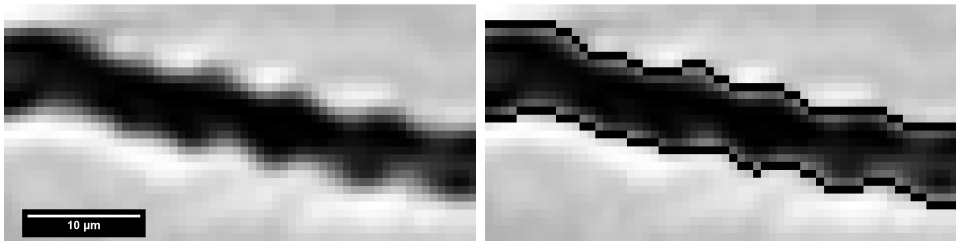

(a) original (b) original with segmentation outline

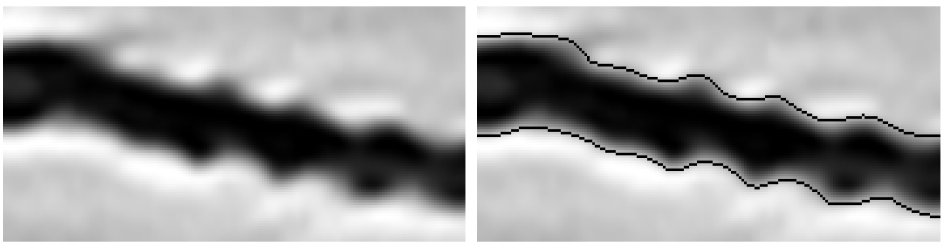

(c) oversampled (d) oversampled with segmentation outline

Figure 6.4: Influence of oversampling (factor 3) on the preservation of the surface morphology during segmentation.

The impact of oversampling on the fracture surface in 3D is illustrated in figure 6.5. (a) and (b) show the voxelated, segmented crack, once in its original condition, once oversampled. (c) and (d) show the corresponding surface meshes. Coarse features are well preserved also without oversampling. But features close to the resolution will only be preserved by oversampling. The same is valid for the surface meshes.

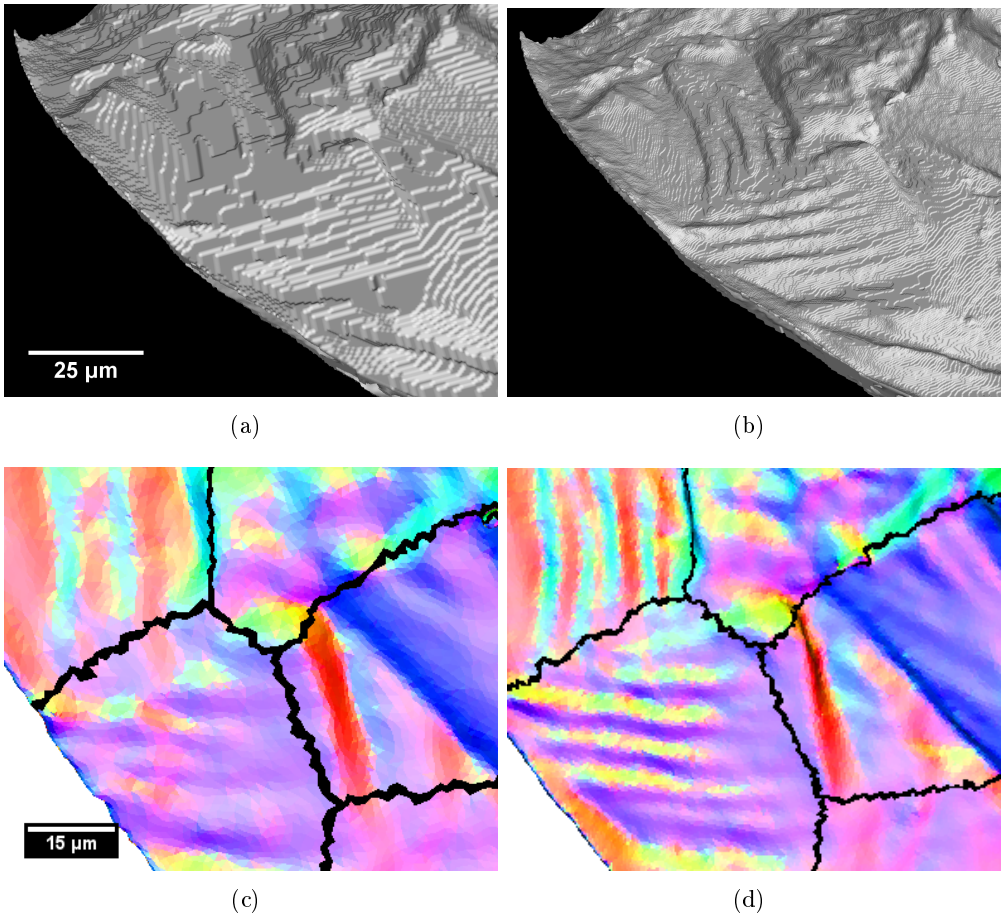

(a) (b)

(c) (d)

Figure 6.5: Isosurface rendition of segmented crack without (a) and with (b) oversampling. Comparison of surface mesh created from the segmented crack in physical color coding without (c) and with (d) oversampling.

6.3.4 Smoothing of Mesh

Figure 6.6a shows the surface mesh as received when applying an isosurface algorithm to the oversampled and segmented crack. The problem with the mesh in this condition is most clearly visible at the sample boarder in the bottom of the image, which is in reality smooth and round. The isosurface algorithm preserves the shape of the voxels and creates a stairway-like surface. In this condition of the surface mesh the triangles' orientations represent the orientation of the voxel cubes and not the one of the fracture surface.

This stairway-like pattern must be removed by smoothing. On the other hand the wave-like features on the surface represent the crack morphology and must be preserved. This can be achieved by the alternating application of an algorithm that smoothens the surface by changing the positions of the vertices and another one that reduces the

number of mesh elements (triangles). A positive side effect of the reduction of the number of elements is that the calculation and visualization effort when working with the mesh is reduced. Figure 6.6b shows the mesh after four iterations of smoothing and halving the number of elements. The stairway pattern is almost completely removed as visible on the sample boarder. Further smoothing is not necessary and will gradually reduce the information on the surface morphology.

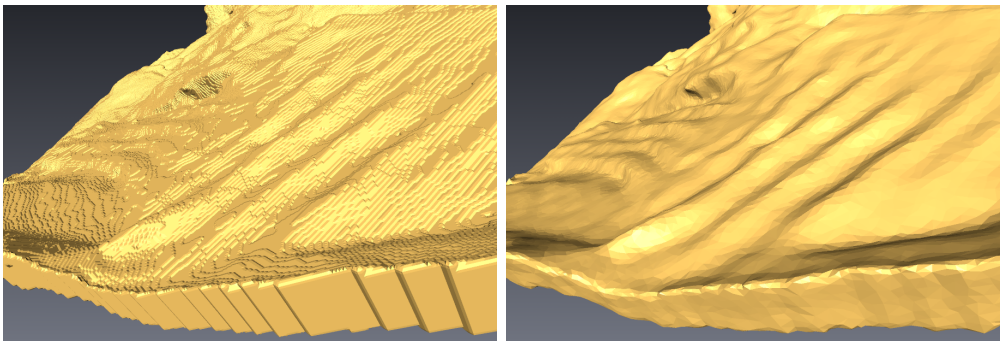

(a) 16 million elements (b) 1 million elements

Figure 6.6: Effect of alternating smoothing and reduction of the number of elements (triangles) on the surface mesh morphology.

Oversampling also has a positive effect on the results of the smoothing procedure. By reducing the voxel size the smallest surface morphology features captured are not at the length scale of the voxels anymore. That means that the smoothing necessary to remove the sharp stairway-like voxel artifacts only moderately affects the fine surface features.

6.4 Interpretation of Fracture Surface

Before being able to interpret the crystallographic aspects of the fracture surface the reliability of the information obtained and in how far the cracks are in stage I have to be discussed. There is no doubt that the crack in VST55531 propagates in stage I since all of the visible planes can clearly be indicated as crystallographic slip planes (figure 5.6c, d). In the case of Beta21S doubts arise from figure 5.6a where many parts of the measured fracture surface do not correspond to crystallographic slip planes; instead large areas of the fracture surface are parallel (within a few degrees) to {001} and {111} planes which are at least 19.4° off from any of the "classic" slip planes {101}, {112} and {123} reported for bcc metals [Honeycombe, 1984].

In how far could this be caused by measurement errors induced for example by the DCT grain reconstruction, the registration of DCT and PCT volumes, the segmentation and the smoothing operations? The error in the orientation as measured by DCT is directly linked to the orientation spread inside the grain of interest: the current DCT processing route assigns an average grain orientation to all voxels belonging to the same

grain and neglects the presence of intragranular orientation spreads. For both materials used in this study the intragranular orientation spread is below 0.2°, justifying the use of these average orientation values. The DCT and PCT volumes were registered using the sample outline and the notch as registration surfaces. The error introduced by a misalignment of the datasets is of order of the pixel size in all directions and its impact on orientation accuracy is expected to be below 0.5°. In several cases, the deflection of the crack coincides well with a grain boundary, as visible in figure 5.5. This indicates that i) misalignment between the datasets must be quite low and ii) wrong orientation assignments due to inaccuracies of the grain map only affect small regions close to the grain boundaries. The surface mesh used for this study describes the outline of the segmented crack. It has therefore an upper and a lower plane that are separated by the crack opening which is up to 15 μm at the notch (see section 4.4). Because the real plane would be in the middle between these planes an error is introduced. In the case of Beta21S with a final crack length of 250 μm the angular errors introduced were up to $\pm 1.7°$ at the notch. But also the combination of all those errors cannot explain the difference between the measured planes and the "classic" bcc slip planes of 19.4°.

We conclude that the measurement errors are not high enough to explain the high amounts of {001} and {111} planes in Beta21S. This brings up the question whether the crack might be a stage II crack. Its fracture surface doesn't show the striations at distances representing the crack advance during one cycle and the crack also doesn't grow on a plane perpendicular to the loading axis as typical for stage II. On the contrary: the crack shows pronounced vertical deviations which are mostly correlated with grain boundaries until the last stage measured. In other words: the crack in Beta21S behaves like a typical stage I crack.

From the SEM/FESEM images (figures 5.15, 5.16) it can be seen that the cracks in both materials seem to grow on facets and that the main difference is that the crack in Beta21S stays less long on a plane. This might be due to the athermal ω precipitates that are reported to form during cooling in β titanium alloys. They should be bigger in VST55531 due to the lower cooling rates and might therefore localize the dislocation movement more effectively, causing a more pronounced planar slip behavior (see section 2.4). When investigating how long the crack stays on one plane (the period of undulations) in Beta21S then values between tens of μm down to a few nm can be found (figure 5.16①-③). The spatial resolution of the PCT images is in the order of twice the voxel size, i.e. close to 1.5-2 μm, what means that most of those events couldn't be resolved in the tomographic experiment. This leads to the assumption that also in Beta21S the crack propagates until the end in stage I. However, since this crack changes its plane on large areas at a frequency beyond resolution in those regions not the real but an effective surface orientation is measured. Figure 6.7 illustrates the possibility to create a macroscopic {001} fracture surface composed of two alternating {101} slip planes. Following this idea the occurrence of a (111) plane on the measured crystallographic fracture surface could for example be explained as being composed of (123) and (321), or (110) and (112).

Several facts make the interpretation of the measured crystallographic fracture sur-

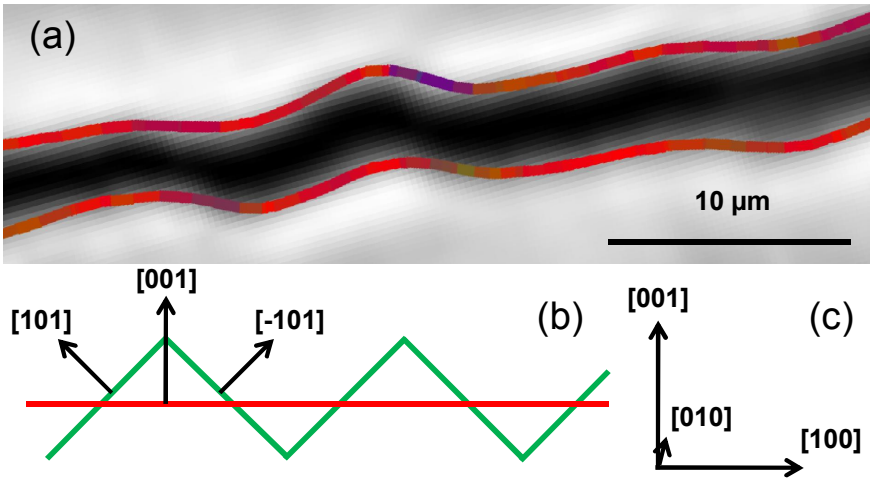

Figure 6.7: a) Superposition of the crack in f (figure 5.6) after 75.5 k cycles as reconstructed from PCT (grey) with the cross-section through the mesh (color) at the same position with applied crystallographic color coding as shown in figure 5.6. The PCT reconstruction shows only smooth undulations indicating that sharp kinks might have been lost at the resolution used. The good correlation between crack and mesh shows that no substantial error was introduced by the meshing procedure. The red color of the cross-section through the mesh represents a surface orientation close to {001}. b) Schematic drawing showing how a macroscopically measured {001} fracture surface (red) can be composed on the microscopic scale of alternating {101} planes (green). c) Common reference system for a) and b).

face orientation difficult in Beta21S. The fact that alternate slip between two planes does not have to occur in equal amounts is clearly visible in figure 5.16①. If the crack propagates in a repetitive way longer on one plane than on the other on a scale below the resolution then the normal of the measured surface will be a linear combination of the normals of the participating slip planes. The crystallographic fracture surface of Beta21S shows in many cases differently colored patches within one grain. We know by now that a green or purple patch means that the crack stays a long distance on a single slip plane. If it is blue or red the crack undulates between two planes. That means even within a single grain the crack doesn't only stay on one plane or on one combination of planes. The combination of planes can even vary locally. Another complication arises from the fact that the period of plane changes is not constant for the system. In cases like grain e in figure 5.6 the crack stays a long distance on a single plane, in cases like grain d it changes its plane at a higher frequency so that a striped pattern is visible, in cases like grain f the frequency is so high that no more traces of the individual slip event can be seen. Figure 5.16③ even indicates that the growth length on each of the participating planes can change continuously, creating arc-like patterns. The combination of all those possibilities leaves so many degrees of freedom for the interpretation

of the crystallographic fracture surface orientation in Beta21S that it can only be analyzed in detail in the few regions where the crack stays a long distance on a single slip plane. This also implies that in order to be able to properly analyze the data, the ratio between the frequency of plane changes of the crack and tomography resolution is extremely important. It determines how far the measured fracture surface orientation represents the real orientation and thereby influences the interpretability of the data in a significant way. If the crack stays a long distance on a single slip plane then the measured plane will correctly represent the real plane. An intermediate frequency of plane changes is visible as "stripes"[5]. Those stripes for example visible in grain d, m, or to the left of grain n, differ from the ones of stage II by at least two factors (see section 6.7): their relative length compared to the crack front and their periodicity. The stripes in stage I are confined to one grain and have a spacing not related to the crack advance during one cycle.

The crack in Beta21S that appears to be composed of smooth undulations at low resolution (figure 5.15②) is visible as being composed of sharp kinks at higher resolution (figure 5.16②). Also various other authors report fatigue cracks that change their planes on very small length scales [Zhai et al., 2000; Ro et al., 2007; Holzapfel et al., 2007]. Schäf [Schäf et al., 2011] even reports crack undulations at less than 100 nm period. The smallest possible distance might be equal to the inter-atomic distance. When taking a closer look at the bcc slip planes it can be seen that at the atomic scale a (112) plane can always be decomposed into two alternating (011) and (101) planes as illustrated in figure 6.8. Accordingly, the (123) plane would be composed of a repetitive combination of 1 part (101) and 2 parts (011). Following this idea of slip at different proportions on 2 alternating planes in a repetitive manner in bcc growth on arbitrary planes containing the <111> direction are possible, a phenomenon that has also been observed and is called "pencil glide" [Penning, 1976]. So since all bcc slip planes of higher order can be decomposed into combinations of {101} planes on the atomic scale there is no reason why the change of slip planes shouldn't go down to the atomic level. As it is hard to draw precise conclusions about the mechanisms of short fatigue crack propagation when the crystallography of the fracture surface is not precisely known, the materials investigated with 3DXTSM should have big grains and a pronounced planar slip character.

Let's assume that our interpretation of the crystallography of the fracture surface is correct and that bigger homogeneous green and purple areas represent crack growth on only a single slip plane, that a striped pattern within a grain represent areas where the crack changes its plane at an intermediate frequency and homogeneous red and blue areas represent high frequency plane changes. As visible in figure 5.6a there are red areas in grain o and f close to the notch. Further away (chronologically later, see figure 5.6) there are grains of homogeneous green and purple color (grain k and e). But in the grain q right next to them the fracture surface is completely red. At about the same distance from the notch a striped pattern is visible in grain m. There seems to be no correlation between crack length and the frequency of plane changes. The crack can

[5] In order to avoid confusions the term "striations", as used for the description of the stage II growth pattern is avoided.

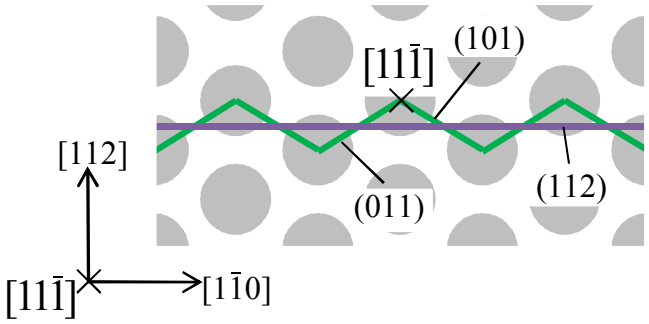

Figure 6.8: View on the atoms of a bcc lattice along [11$\bar{1}$]. On the atomistic scale each {112} plane can be decomposed into alternating {101} planes.

change back and forth between high and low frequency plane changes. There also seems to be no law for what frequencies are possible. This lack of correlation might indicate that the crack in Beta21S is everywhere controlled by the same growth mechanism, and that the local frequency of plane changes is only a "symptom" of this mechanism.

SFC growth at very low frequencies of plane changes (in particular the extreme case of frequency 0) corresponds to what is often termed "single slip" in the literature [Krupp, 2007]. Crack growth along a surface composed of two alternating slip planes is often called "double slip". This would correspond to crack growth at higher frequencies in our case. Using these terms our results mean that there is no fundamental difference between single and double slip. This would support the classification of Düber et al. [Düber et al., 2006] who assign both growth modes to stage I of SFC growth (stage Ia, Ib). But other than Düber et al. we can't draw a clear line between the two modes and therefore suggest to describe the short fatigue growth mode during stage I in terms of frequency of plane changes (e.g. low/middle/high frequency stage I crack growth).

6.5 Crack Propagation

6.5.1 Dependence on Fracture Surface Crystallography

The few areas which appear to be parallel to slip planes in figure 6.9 are clearly the minority of the facets observed. In some cases such areas are correlated to a higher crack growth rate. The crossing of j, k, l and e detailed in section 5.1.7 is quite illustrative of this effect. When the crack front enters e after being delayed in j, it clearly accelerates when cracking occurs on a {101} plane which becomes the dominant plane for the rest of the grain.

The overall crack growth rate on the left side of the crack seems to be higher than on the right (figure 5.7, 5.8) although the left side doesn't show a higher density of areas oriented closely to slip planes (figure 6.9). This might be either explained by the lack, on the left wing, of pronounced barrier effects due to grain misorientations such as the transition between j and e or, by a higher load on the left side due to a slight tilt of the

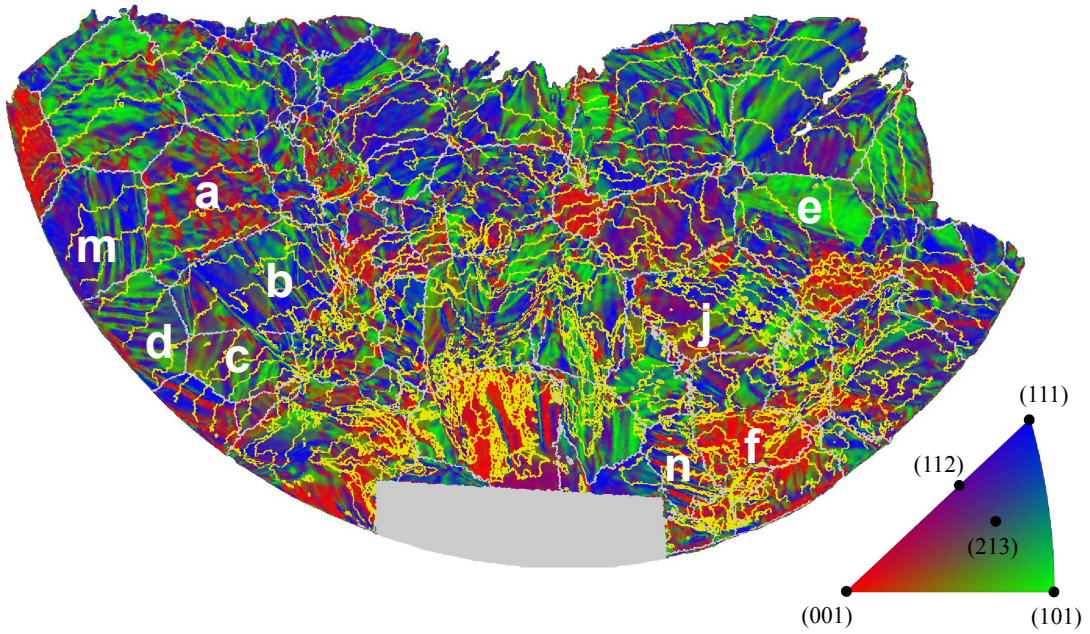

Figure 6.9: Overlay of crack fronts (yellow) and crystallographic orientation of the fracture surface.

sample in the fatigue machine.

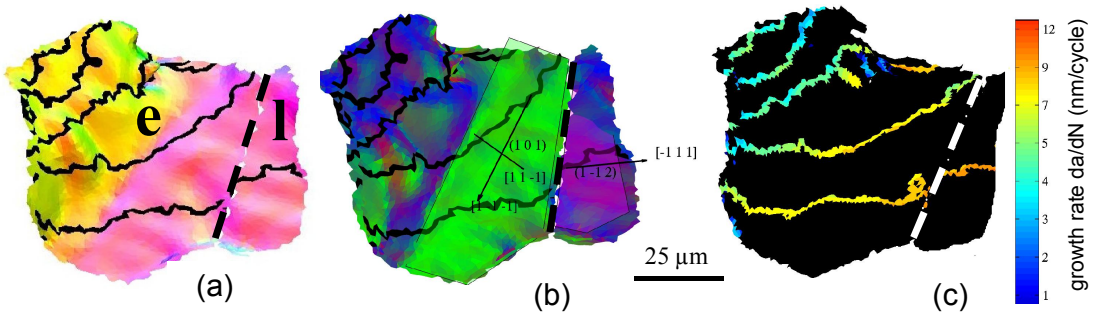

Figure 6.10: Grain e and a part of grain l. The grain boundary is marked by the dashed line. (a) physical, (b) crystallographic color coding and (c) with depicted growth rates. In (a,b) the crack fronts are labeled in black.

Figure 6.10 shows a good example in what depth each grain of a 3DXTSM dataset can be analyzed. It depicts grain e and a part of grain l in Beta21S from a side-view perspective in three different color-codings. As visible by the almost homogeneous pink colour in the physical color-coding the crack plane on the right of grain e and the one in grain l have almost the same orientation. The crystallographic color-coding reveals the pink part of grain e as being closely oriented to a (101) plane. The exact (101) plane is

shown as semi-transparent overlay together with the corresponding slip directions. The crack plane in grain l can be identified as $(1\bar{1}2)$ plane. Obviously in terms of orientation the two planes are compatible. This correlates well to the measured crack fronts. The crack is not retarded at the grain boundary. On the contrary, it seems to propagate faster to the right than to the left, as can be interfered from the rotation of the crack front. The different growth rates can be quantified using the growth rate color-code. The maximum measured growth rate to the right is about 10 nm/cycles while to the left at the end of the pink plane it is about 7 nm/cycles. This retardation to the left-hand-side might be explained by the growth behavior. To the left of the pink plane the crack plane cannot clearly be identified. There seem to be bumps in the fracture surface; an indication that the crack propagates locally on different planes/ combinations of planes. This means that there is a certain resistance to crack propagation to the left, since the bumps represent additionally created fracture surface compared to a straight plane. The strong variation of colors to the left also mean that the crack changes its plane beyond the resolution. This implies that the real fracture surface is higher than the measured one. The measured growth rates are correspondingly lower than the real ones in such cases. This means that microscopically the crack to the left might propagate on combinations of planes as fast as to the right (might create as much fracture surface per time). However, macroscopically the crack fronts take bigger steps and the measured growth rates are higher to the right. So, the resolution affects also the measured growth rates.

A few more things can be learned from figure 6.10 and should be pointed out. A stage I crack can alter the frequency at which it changes its planes abruptly right in the middle of a grain. A low frequency stage I crack has no constant growth direction in polycyrstals. This also implies that there is no direct relation between its growth direction and a specific slip direction of its growth plane. It might be, that the growth direction can be any linear combination of the slip directions of a slip plane.

6.5.2 Formation of Stripes During Stage I Growth

Let's try to further investigate the crack growth mechanism in Beta21S by analyzing the orientation of the stripes visible on the fracture surface like in grain d and m in figure 6.11. Since the colors in our depiction represent surface orientations those patterns represent a corrugated fracture surface. An eye-catching feature of figure 6.11b is that there seems to be no orientation relation between crack fronts (growth direction, respectively) and stripes. If one assumed that the patterns were created by "double slip" according to the Neumann model this is surprising, since Neumann, Fuhlrott and Vehoff [Neumann et al., 1977, 1979], seem to have always conducted their experiments in such way that the crack fronts were parallel to the lines along which the crack switched its planes. This brings up the question if the mechanism investigated by Neumann, Vehoff and Fuhlrott on single crystals is at all possible in polycrystals. The requirements necessary for such a pure growth mechanism can hardly be fulfilled in several grain simultaneously. First, because in a polycrystal out of an anisotropic material no homogeneous stress field can be created. Second, because the compatibility of the system consisting of

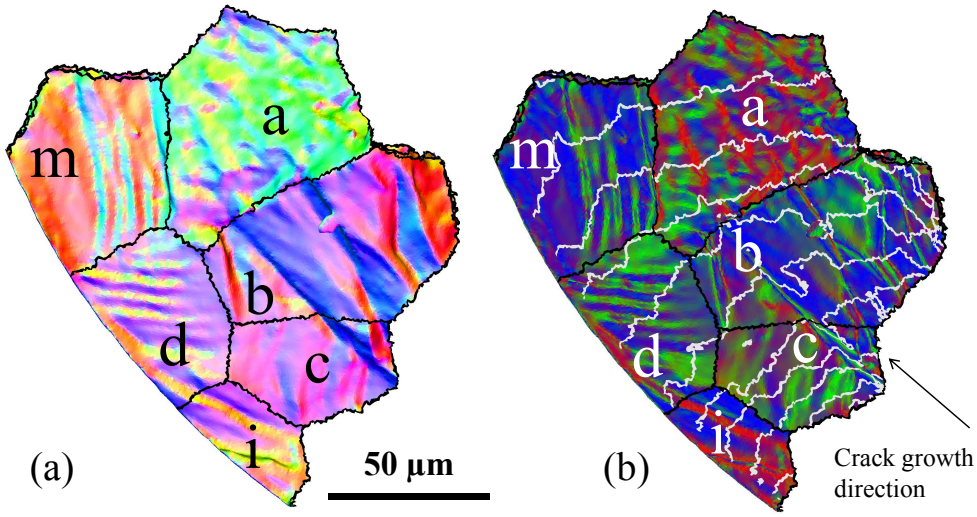

Figure 6.11: Magnification of a subregion of figures 5.5 and 6.9 showing (a) the physical color-coding and (b) the crystallographic color-coding with overlayed crack fronts.

crack plane, grain boundary and slip plane in the adjacent grains have to be taken into account. In a material with little texture the chance for compatibility is already low if the crack only propagates on one plane in each grain. Propagation on two alternating planes in each of the adjacent grains would require that twice as much planes have to be compatible, which is even less probable. So, in terms of probability the pure growth mechanism as described by Neumann will always be restricted to individual grains. At least at the grain boundaries there should be some ductile rupture involved. This was also experimentally confirmed by e.g. [Hornbogen and zum Gahr, 1976].

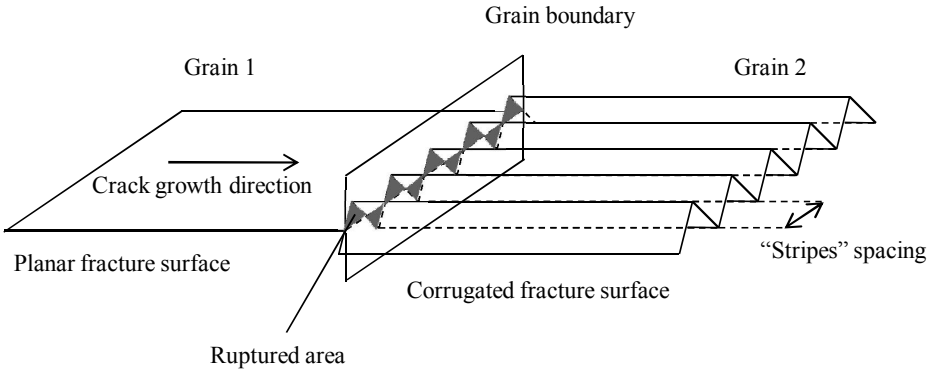

Figure 6.12: Growth mechanism that could possibly explain the corrugated patterns (stripes) visible on the fracture surface of Beta21S.

Figure 6.12 illustrates schematically a growth behavior as observed by Schäf [Schäf

et al., 2011] using FIB tomography. The area that has to rupture along the grain boundary for the crack to proceed as proposed by Zhai [Zhai et al., 2000] is labeled in gray. Schäf evidenced that a stage I crack, propagating on a single slip plane, can change into a corrugated fracture surface, composed of alternating slip plane facets, after having passed a grain boundary. This was the case when there was no compatibility between incident slip plane and the combination of grain boundary and slip planes in the next grain. Schäf observed "stripe spacings" of less than 100 nm.

What seems to happen when the crack does not find a compatible slip plane behind the grain boundary is that it selects a path composed of alternating slip planes. Like this it is possible to create a macroscopic crack plane that fits to the crack front at the grain boundary. The smaller the spacings between the plane changes of the corrugated pattern the lower the fracture surface that has to be created along the grain boundaries. Schäf [Schäf et al., 2011] measured a slower crack propagation in the region of the corrugated pattern and relates this to increase of fracture surface that must be produced per crack length.

The experiments of Schäf were mostly done on bicrystals and the crack growth rate could only be observed on the surface. The crack in the Beta21S sample is a more complicated case but this also means that it contains more information. The case shown in figure 6.12 seems to happen when the crack enters grain d coming from grains b and c (figure 6.11b). After having passed the grain boundary the crack continues in a corrugated way, visible by the stripes on the surface. The stripes do not start abruptly at the grain boundary but this might be explained by inaccuracies of the method. The physical view (figure 6.11a) confirms that the crack is about on the same plane along the grain boundary between grain b, c and d.

Coming from grain d the crack enters grain m. Here another corrugated pattern is visible. Although the method's accuracy is not high enough to be sure, it seems like for each of the stripes visible in grain m, there is a corresponding stripe in grain d (figure 6.11a). The stripes seem to continue across the grain boundary but in another direction. This could mean that a crack arriving in a corrugated way on a grain boundary also tries to find matching corrugated slip planes in the next grain. For the model shown in figure 6.12 this would mean that the plane in grain 1 would have to be replaced by a corrugated surface. The orientations of the corrugated patterns in the two grains may be different.

From the different colors of grains m (mainly orange) and d (mainly purple) (figure 6.11a) we can see that the principal physical orientations of the fracture surfaces in the two grains are different. For our model in figure 6.12 this means that the principal planes of the corrugated patterns might be tilted with respect to each other. Further from our dataset can be learned that there is no direct correlation between crack growth direction and the orientation of the corrugated pattern. The crack fronts in grain d are inclined by about 45° to with respect to the stripes, while the inclination angle is about 90° in grain m (figure 6.11b).

With the mechanism described above it would be possible to explain the whole measured fracture surface in Beta21S by assuming that the spacing between the "stripes"

(the frequency of plane changes) can vary in a wide range. Stripes like in grains m and d (figure 6.11) are only visible for an intermediate frequency of crack plane changes. As mentioned before, an effective surface orientation will be measured if the frequency of crack plane changes is too high to be resolved, what could explain the measured (001) orientation in grains f and q in figure 5.6. Where there is compatibility at the grain boundaries like in the case e and l in figure 6.10 the crack stays a long distance on a single slip plane.

Due to the lack of spatial resolution, the crystallographic orientations of the planes of the corrugated patterns in grains d and m in figure 6.11b cannot be trusted since the crack only stays for less than 5 μm on one plane. Also the crack fronts were not measured precisely enough to be able to take a closer look at the mechanism of the formation of the corrugated patterns in Beta21S.

However, the VST55531 sample might give a closer insight into the formation mechanism of the corrugated sheets if the experiment is continued. At the last growth stage measured the crack formed several parallel but displaced planes behind the grain boundary (arrows in figure 5.5d). Cross-links between those planes are not yet visible although they already have a considerable length. But the material between the planes must be split in order for the crack to proceed. This indicates that there are no favorable oriented slip planes between the "fingers". It might be that a single or a combination of slip planes between them will be activated at a higher number of cycles so that the fingers bridge by slip when the experiment is continued. But it might also be that the stress-intensity between the fingers will reach a level where the gaps are bridged by ductile rupture or cleavage. In the latter case not all crack planes would correspond to slip planes. This would be a mechanism that is assumed to be responsible for the formation of "factory roofs" in FeSi%3 [Qiao and Kong, 2004; Qiao and Argon, 2003a,b].

6.5.3 Example of Crack Retardation

Figure 6.13 shows an example of the crack-retarding effect of a grain. Such deceleration correlated with a grain boundary has e.g. been described by Zhang and Navarro [Zhang and Edwards, 1992; Navarro and de los Rios, 1988] before. Figure 6.13a shows that the crack doesn't take the direct way from grain o to p. There is only a small branch that goes directly into the central grain p. The crack propagates to the left along the grain boundary and to the right it passes by until it enters grain p sidewards. Figure 6.13b shows a clear dint in the crack front in grain p which represents a local decrease of the growth rate. The crack front in figure 6.13c doesn't show significant signs of a dint anymore. After having passed the central grain the crack has caught up with the surrounding parts.

The white part in grain p and grain o visible in figure 6.13b and c (also visible as red area marked with an arrow in figure 5.7a) is probably caused by a segmentation error. Although this position was probably already cracked at this point of time this couldn't be measured, since, as can be seen in figure 5.5a, the crack plane in this section is almost vertical. The PCT scans were done under vertically applied load. So, the fracture surfaces at those points might have been to close to be detected.

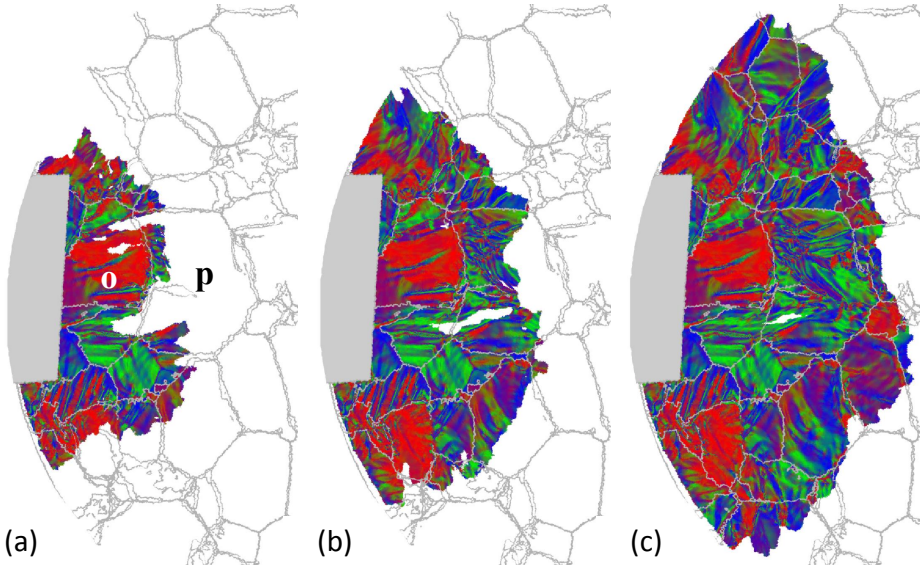

Figure 6.13: Crack front after (a) 59 k, (b) 63 k, (c) 69 k cycles. Grain Boundaries are labeled in grey. The crack has obvious difficulties to traverse grain p.

Figure 6.13 is a good example for a mechanism as described by Cox [Cox and Morris, 1988]. When the crack has difficulties to enter a certain grain it will be retarded in front of the grain, creating a dint in the crack front. Locally this corresponds to an increase in the stress intensity. When the stress intensity in front of the retarding grain is high enough the crack can resume growing.

Further analysis of the mechanism shown in figure 6.13 is hardly possible, given the resolution of the dataset and since the crack propagates on an unknown combination of planes in grains o and p.

6.5.4 Growth Rate Diagrams

That the mean growth rates shown in figure 5.9a show less scatter with increasing crack length is mainly because the local differences even each other out. That there are big local differences is visible on the big errorbars. Those even seem to be proportional to the average values. That means that the higher the maximum growth rates, the bigger the difference to the lowest growth rates. This can be explained for example on the branch that rises up on the right-hand-side of figure 5.9 and covers the principle part of the crack. At this branch the crack almost stops, so that very low growth rates in the order of 1-5 nm/cycles are measured even at 75 k cycles while the main crack branch propagates at about 30 nm/cycle in average.

Figure 6.14a shows the growth rate over the crack length along a 2D section through Beta21S as extracted from figure 5.7b. No clear correlation between growth rate and grain boundary positions are visible. This is partly due to the low time resolution. The peak shown right after the crack entered grain r is mainly due to the high growth rate

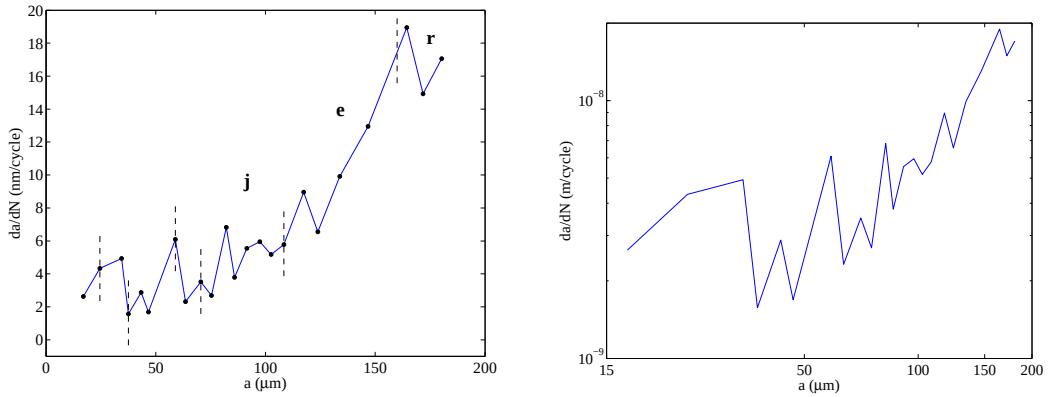

(a) (b)

Figure 6.14: 2D growth rates along plane marked by dashed line in figure 5.7b. (a) Applying a linear scale. The dashed lines mark intersections with grain boundaries and were inserted manually according to figure 5.7. (b) Applying a double logarithmic scale.

in grain e. But partly the missing clear correlation is also due to the change of the growth behavior within a grain. So the crack growth on a combination of unidentifiable planes visible in grain j seems to continue in the first part of grain e but then suddenly changes. This is correspondingly visible in the figure 6.14a.

Considering the increasingly linear appearance of the log-log plot of the graph in figure 5.9a at longer crack lengths (figure 5.9b) then one could think that the crack at the last growth stages measured in Beta21S is already in the Paris regime. But again one must keep in mind that these are values averaged along the front of a 3D crack. The Paris law is only fulfilled when the log-log plot of the growth rate measured on 2D sections is linear proportional to ΔK ($\propto$ square root of the crack length). This fact is illustrated by the log-log plot in figure 6.14b. Here the relation between growth rate and crack length is clearly not linear even at long crack lengths.

6.6 Statistical Analysis

6.6.1 Schmid factor

The ability of a grain to slow down a crack (see for example j) should be related to the ability of the grain to activate plasticity. This is linked with the local value of the Schmid factor i.e. to the local grain orientation and to the local stress tensor. Although the former is known, the latter is more complex to evaluate as the presence of the crack tip induces a tri-axial stress distribution different from the macroscopically applied uniaxial loading. An illustration of this point can be found in figure 5.10 which shows the crystallographic normals recorded for grain e (see figure 6.10). In this grain, it was shown that after a transient state corresponding to the crack entering the grain, cracking occurs mainly on a {101} plane with a local acceleration of the crack growth

rate. Although figure 5.10 shows indeed a concentration of normals around two {101} planes, it can be seen that these planes do not correspond to the highest Schmid factors if a uniaxial stress state is assumed in this grain. Although the $(0\bar{1}1)$ plane has a maximum value of 0.5, it does not correspond to the (101) plane which is observed. The Schmid factors calculated on the simple assumption of a uniaxial state of stress cannot account for our observations. Finite Element Crystal Plasticity (FECP) calculations taking the elastic anisotropy of the grains and the 3D shape of the crack into account can in principle be performed to evaluate the local stress state at the crack tip. First calculations have been carried out based on polycrystal volumes containing artificially introduced notches [Proudhon et al., 2010] and the incorporation of the complex crack geometry into the numerical model is currently under investigation.

6.6.2 Pole Density Distributions

The two alloys investigated show strong differences in the crystallographic pole density distribution (figure 5.11). This can be explained by the ratio between resolution and frequency of plane changes. If no ductile rupture is involved in the fracture surface formation, then, ideally, (in the case of infinite resolution) all intensity in the pole figures would be on the points representing the bcc slip planes. At a lower resolution the transitions between planes get smoothened out and some intensity will be "visible" on lines connecting the bcc planes. This is what happens in figure 5.11a that shows VST55531. There is a clear peak at (101) and a streak of intensity between (101) and (112). The (213) pole lays on this streak and only from the pole figure it can't be told if the {123} plane family is also activated or only {101} and {112}. As can be seen in figure 5.6d significant amounts of the fracture surface in VST55531 belong to transitions points between {101} and {112} planes. The intensity on the streak between (101) and (112) in figure 5.11a is probably due to those transition points and the {123} slip plane family not activated.

In the case of VST55531 there seem to be mostly transitions between {101} and {112} planes. If there were transitions between different types of {101} or between {101} and {112} and the resolution too low to resolve the individual slip events intensity in the pole figures will be also visible at (001) and (111) and in between those planes and the slip planes. This is the case for Beta21S, shown in figure 5.11b.

Figure 6.15 shows the plane normal distribution of Beta21S in the complete stereographic projection, not only its symmetric equivalents in the standard stereographic triangle like in figure 5.11b. There is certainly some kind of "selection rules" involved between which slip planes the crack can alternatingly propagate, otherwise the intensity would be distributed more homogeneously.

The interpretation of the pattern is however extremely complex since there are many unknown parameters (activation of slip systems, validity of the crack growth mechanism discussed in section 6.5.1, out of which combinations of microscopic planes a macroscopic fracture surface can be composed of). If those parameters were known the probability for slip to happen on certain combinations of planes might be investigated. Determining some of these parameters on single crystals and characterizing parts of

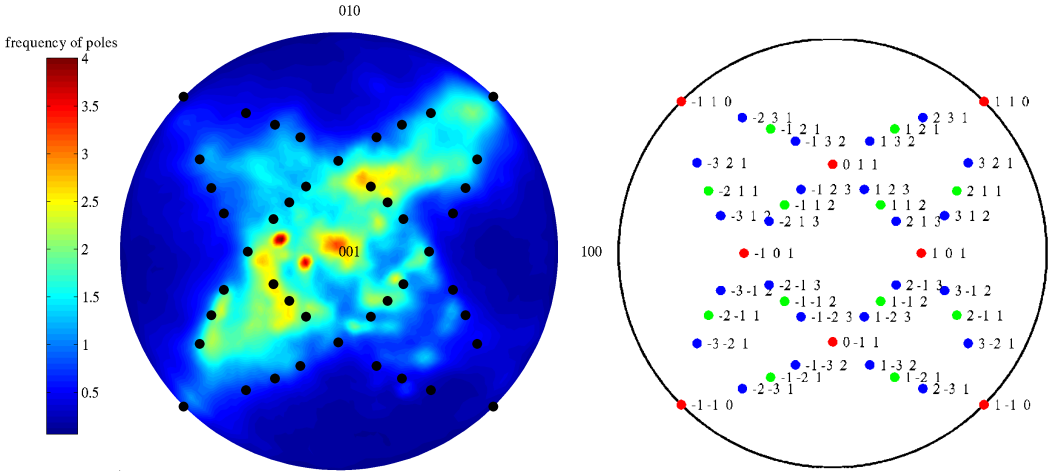

(a) (b)

Figure 6.15: (a) Standard stereographic projection of the crystallographic pole distribution in Beta21S. The black points mark bcc slip planes. (b) Identification of the slip planes shown in (a).

the fracture surface in Beta21S at a much higher resolution (e.g. by X-ray projection microscopy [Mayo et al., 2002]) would be very helpful to interpret the pattern.

6.6.3 Micro Texture

In order to fit the micro structure shown in figure 5.12 the poles were rotated to an angle where the pattern is highly symmetric and easy to understand. Figure 6.16a shows the {100} poles visible in figure 5.12 after rotating by 90° around x. From this perspective the pattern looks like two diagonals that cross in the center at an angle of 45° with two semicircles at the top and at the bottom. This pattern can be simulated by assuming that the (100) poles from all grains lay on the diagonal ① and all (010) poles lay on ② (figure 6.16b). When selecting a random position of a (100) pole on ① the position of pole (010) on ② is also fixed since there must be an angle of 90° between the poles. The cross-product of these two poles is the corresponding (001) pole which lays on ③. Figure 6.16b shows the plot of a row of equiangularly distributed (100) poles and their corresponding (010) and (001) poles.

A set of (100), (010) and (001) poles can be considered as a grain orientation. Figure 6.17 shows the simulated {100}, {110} and {111} pole figures after rotating these grain orientations back by -90° around x. That this pattern shows a distribution similar to the one observed in 5.12 means that the fitting procedure, neglecting scatter, was successful. We thereby know that in Beta21S, on average, one {100} pole is circularly distributed at an angle of about 20° around the z axis (loading axis) and that the other two {100} poles "wobble" around the x-y plane at a maximum angle of about +-30° (see simulated {100} pole figure). This can be especially clearly seen in the {100} pole figure

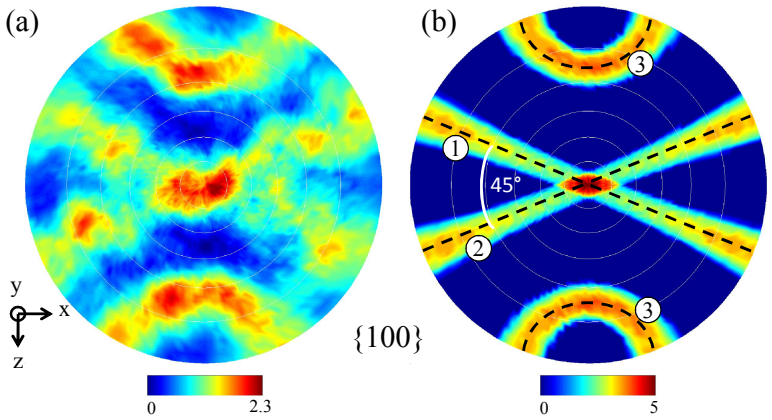

Figure 6.16: (a) 100 pole figure after rotation of poles by 90° around x. (b) Corresponding simulated pattern.

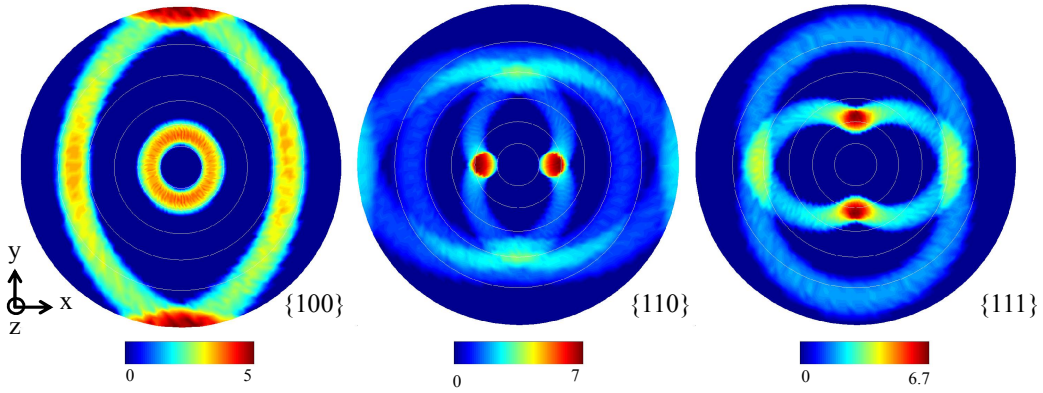

Figure 6.17: Simulated micro texture patterns shown in figure 5.12.

of figure 6.17. There is quite a large scatter in the texture patterns and the density is not confined to certain points but distributed on lines. The texture in Beta21S is therefore not very pronounced and will not strongly influence crack propagation.

In the case of VST55531 the orientation of the about 400 reconstructed grains showed such strong scatter that the effect of texture can be neglected.

6.7 Discussion of Growth Stage Classifications

The definition of stage I and stage II cracks, as shown in section 2.3, is a topic that is still controversially discussed. There are disagreements in the fatigue community about the classification of growth stages, the prevailing fracture mechanisms and the correlation with surface patterns. The lack of precision of the definitions found in the literature are certainly caused by the complexity of fatigue. There is a fluent transition

between a broad variety of mechanisms which are influenced by an even broader variety of parameters. The same alloy can show a completely different behavior after having received a different heat treatment [Blankenship and Starke, 1991]. It is therefore useful to try to summarize the classification of fatigue growth stages found in the literature and to incorporate new insights from this study in order to more precisely identify characteristics of the two extreme cases of fatigue growth: pronounced stage I and pronounced stage II growth.

Krupp [Krupp, 2007] distinguishes the stripes visible on the fracture surface during stage I and the striations visible during stage II according to their spacing. He does not take their orientation or their continuity across grain boundaries into account. Our 3D crystallographic view on the fracture surface, grain boundaries and crack propagation makes visible what might have been overseen so far in 2D sections. The orientation of the surface stripes during stage I growth are not correlated with the shape of the crack front (figure 6.11). Striations produced during stage II growth are parallel to the ancient crack front since they are created by plastic deformation at the crack front. Another detail that is more clearly visible on the 3D fracture surface is that the spacing between the stripes we deal with is not regular. It generally stays constant within one grain but in different grains stripe direction and spacing are normally different (figure 5.6). Those features can be taken into account to identify stage I cracks. Krupp may be right when he states that crack propagation in stage Ib can appear very similar to stage II [Krupp, 2007]. But this seems to be only valid for 2D sections where the stripe/striation orientation is not visible.

The discussed differences between the fracture surface of stage I and II cracks are summarized schematically in figure 6.18. The crack starts in stage I. In this phase the fracture surface is composed of facets corresponding to slip planes and the stripes mark plane changes. The stripes vary in direction and spacing and are usually confined to only one grain. Further away from the crack origin there is a transition phase where in some grains the crack propagates still on crystallographic planes whereas in other grains which are not oriented favorably it propagates already in stage II (yellow). During stage II growth the fracture surface does not correspond to crystallographic planes and the surface pattern is not characterized by sharp kinks but by smooth, wave-like undulations at a spacing which corresponds to the crack advance during one cycle.

An overview of the revised growth stage classification is given in table 6.2. The expression “short fatigue crack” is ambiguous, since it is not the size of a fatigue crack that matters in terms of its behavior but the mechanism. Even a very short crack can already propagate in stage II when only the load is high enough. The expression “stage I fatigue crack” seems to be more appropriate.

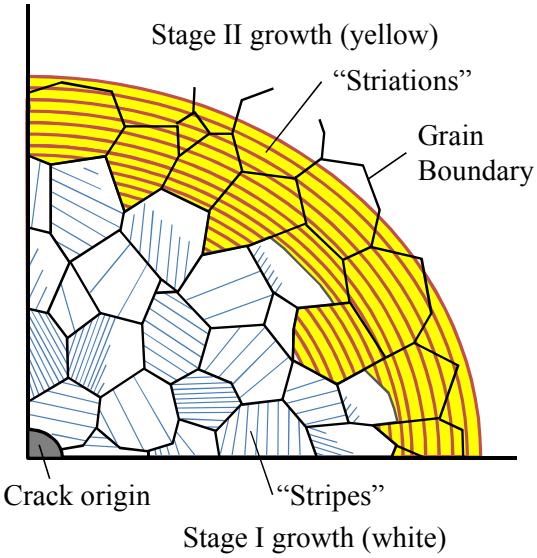

Figure 6.18: Schematic drawing of a fracture surface showing stage I and II fatigue crack growth for a near corner crack.

Proposed term	Stage I fatigue crack	Stage II fatigue crack
Potentially misleading term	Short fatigue crack	Long fatigue crack
Stress intensity at crack tip	High enough to activate slip on mainly one or two slip planes	High enough to activate slip on many independent slip planes
Growth regime	Near threshold regime	Paris regime
Growth prediction	Crystal plasticity, discrete dislocation dynamics	LEFM
Mechanism	Strongly crystallographic: shear on slip planes or dislocation annihilation	No crystallography involved: plastic blunting/ resharpening
Pattern origin	Stripes represent crystallographic plane changes	Striations are caused by plastic blunting/ resharpening
Pattern orientation	Stripes are not correlated with crack propagation direction and different in each grain	Striations represent former crack front, viz. the striations are perpendicular to the crack growth direction
Pattern connectivity	Stripes normally not connected across grain boundaries	Striations form connected lines across grain boundaries
Pattern spacing	Varying, mostly constant within one grain, not linked to growth rate	Corresponds to crack growth per cycle
Pattern morphology	Sharp kinks where planes change (if resolution is high enough to resolve them)	Rather smooth undulations

Table 6.2: Summary of revised features of the two extremes of fatigue growth regimes: pronounced stage I and pronounced stage II fatigue crack propagation.

Chapter 7

Conclusions

Within the framework of this thesis the accuracy of the grain boundary position as reconstructed with Diffraction Contrast Tomography (DCT) was evaluated. The β titanium alloy Beta21S was chosen for this task since this material offers a mechanism with which the position of the grain boundaries can be revealed in Phase Contrast Tomography (PCT). For this material the accuracy could be evaluated to be 2.6 μm on average and similar values can be expected in materials exhibiting comparable values of intragranular orientation spread. The elastic constants of Beta21S needed for numerical simulations were measured using Inelastic X-ray Scattering (IXS): C_{11} = 153 GPa, C_{12} = 101 GPa and C_{44} = 57 GPa.

The occurrence of Stress-Induced Martensitic Transformation (SIMT) was investigated in Beta21S in order to exclude a strong influence on the local stress field and thereby an unnecessary complication of simulations and erroneous interpretation of fracture surface features. No evidence of SIMT could be found using SEM, EBSD, FESEM and XRD. We conclude that if SIMT occurs for microscopic volume fractions below the sensitivity limit of these methods, its impact on the stress field and crack propagation direction must have been negligibly small. In VST55531 the occurrence of SIMT can be excluded, mainly because of the composition of the alloy but also because of the different heat treatment.

The quality of the PCT reconstructions was found to depend critically on the acquisition parameters. The best imaging conditions, as evaluated on the VST55531 sample (mounted in the fatigue machine), were: a sample-to-detector distance of 49 mm, an energy of 52 keV, a pixel size of 0.7 μm and at least 1500 projections. For reasons of image quality and exposure time the use of a smaller fatigue machine would be strongly advisable. This would allow to work at shorter distances, and would reduce artifacts caused by the phase contrast. A reduced weight of the fatigue machine would also reduce mechanical inaccuracies (e.g. wobble of the rotation stage), which is one of the limiting factors for the ultimate spatial resolution achievable with the current instrument.

Oversampling of the 3D tomographic volume data was identified as a mandatory processing step to preserve morphological features close to the resolution during conversion of the crack from volume data into a surface mesh.

A characterization method termed "3-Dimensional X-ray Tomography of Short cracks and Microstructure" (3DXTSM) was developed on the alloy Beta21S and tools for the investigation of the fracture surface orientation, the evolution of the crack front, the 3D local growth rate, the growth rate along arbitrary 2D sections and for statistical analysis were implemented. All those tools are can now be used for further investigations in different material systems.

The combination of DCT and PCT for stage I crack analysis (3DXTSM) is a powerful tool since it precisely provides all crucial information: grain shape, grain position, grain orientation and crack propagation in 3D. Transformation of the crack into a surface mesh and assigning a data structure containing information on grain orientation and crack evolution to each of the surface elements enables quantitative analysis of various aspects of the crack propagation process. The physical colourcoding reveals correlations between crack deflection and grain boundaries and allows for the identification of crack-retarding microstructure configurations. The crystallographic color coding reveals correlations between crystallographic slip planes and fracture surface orientation as well as local crack growth rates.

The two cracks (Beta21S and VST55531) investigated in this study were stage I fatigue cracks until the last growth stage measured. The main difference between the material systems is that in the case of VST55531 the crack changes its plane less frequently. The distance how long a crack propagates on a slip plane before it changes its plane could in principle go down to the inter-atom spacing. The ratio between this distance and the resolution is of great importance for 3DXTSM. Only if the crack stays long enough on a single plane (about 10 μm at the resolution used in this study) the measured fracture surface orientation corresponds to the real orientation. If the distance between the plane changes is close to that value but smaller the plane changes are visible as periodically changing color pattern on the fracture surface. If the distance is very short the single plane changes aren't visible anymore and the normal of the measured fracture surface will be a linear combination of the normals of the participating slip planes. In order to be able to accurately interpret 3DXTSM data, material systems that show pronounced planar slip behavior should be used.

Since according to our results we can't find a significant difference between what is termed single and double slip in the literature we suggest to classify stage I cracks according to their frequency of plane changes.

A low frequency stage I crack has no constant growth direction in polycrystals. This also implies that there is no direct relation between its growth direction and the slip direction(s) of its growth plane. The striations on the fracture surface of a stage I crack are different in morphology, orientation, spacing and continuity from the ones of stage II. This observation can help to identify the prevailing growth stage and thereby the mechanism from post-mortem fractography inspections.

As the fracture surface will be underestimated when the crack changes its plane below the resolution also the growth rates in those regions will be underestimated since they are calculated from the crack advance per measured fracture surface.

We finally point out that even in 3D the average crack growth rate, defined as

the ration between crack surface increase and crack front length, still shows strong fluctuations due to crack - microstructure interactions. Quantitative predictions of the local growth behavior of stage I cracks will necessarily have to be based on the 3D crack shape and the 3D grain microstructure in proximity of the crack.

Chapter 8

Perspectives

This study gave new insights into the growth mechanisms of stage I fatigue cracks but especially the Beta21S sample demonstrated the need for simplification of the material and its crystallographic deformation modes to make it easier to draw clear conclusions. A promising candidate for future investigations that is well suited for the technique 3DXTSM and where results are expected to be easier interpretable is Al-Li2.5%.

First of all Al-Li alloys are interesting for SFC investigation since pronounced stage I growth (up to 1 mm crack length) were reported [Venkateswara Rao et al., 1988]. A pronounced planar slip character means for our method that also at lower resolutions the crack plane can be accurately identified since it stays on large areas on a single plane.

Using a bcc system like Beta21S or VST55531 goes along with the disadvantage that normally more than one slip plane family is active. For each family the dislocation mobility is different which means an unnecessary complication for example for simulations where this would have to be taken into account. Further the propagation of screw dislocations in bcc is more complicated (asymmetry of stress field around the dislocation core, high temperature dependence of mobility) [Kubin, 2011] and less understood than in fcc. Working with an fcc alloy like Al-Li would have the advantage that slip could only occur on one slip plane family, containing four slip planes. Dealing with only four possible slip planes per grain instead of the 18 in bcc (if only taking {101} and {112} into account) means that even if there are small misalignments between DCT and PCT datasets the crystallography of the crack plane can be identified with high accuracy.

Further there is much less effort involved in the heat treatments of Al alloys compared to Ti alloys since the former don't require a shielding gas atmosphere.

Also the low X-ray attenuation coefficient of Al-Li is an advantage, because it means that low photon energies can be used where the resolution and detector efficiency are higher (the latter meaning shorter measurement times). A low X-ray attenuation coefficient also implies that upscaled samples can be investigated which simplifies their handability. At 0.7 μm pixel size a sample of 1 mm diameter and with 100 μm grain size would be a good compromise between having the crack behavior of a polycrystal, easier interpretation and high characterization accuracy.

Al-Li2.5% can be brought to the desired condition by strong plastic deformation followed by a recrystallization heat treatment for 3 minutes at 490 °C and subsequent water quench. A pronounced planar slip character can be obtained by aging for 8 hours at 100 °C [Brechet et al., 1987]. Diffraction tests on Al-Li2.5% in the above mentioned condition confirmed good suitablility for DCT.

In order to shorten measurement times and to improve image quality a smaller fatigue machine should be used. If this is not possible it could be tried to improve the image quality using a phase contrast removal algorithm. The accuracy of the measured fracture surface morphology could be improved by measuring the sample after the fatigue experiment with high resolution tomography outside the fatigue machine in optimum conditions (distance, wobble) or using X-ray zoom tomography [Mokso et al., 2007]. Another possibility would be to break the sample after the fatigue experiment and characterize the fracture topography using SEM, interferometry or confocal microscopy and to convert this signal into a surface mesh.

The surface mesh used for this study describes the outline of the segmented crack. It has therefore an upper and a lower plane that are separated by the crack opening which is up to 15 μm at the notch. Because the real crack plane should be in the middle between these planes an error is introduced. It should be tried to develop an algorithm that finds this intermediate plane.

In order to confirm figure 6.18 the transition between stage I and stage II should be measured using 3DXTSM. In the crystallographic fracture surface view stage II should appear as blunt, completely uncrystallographic waves that describe the crack front at a given number of cycles.

The different slip behavior in the two investigated β Ti alloy systems is probably due to the ω precipitate size. This could be further investigated by TEM observations.

The occurrence of {111} planes on the measured crystallographic fracture surface might indicate that alternating slip in a repetitive manner between the {101} and the {112} plane families is possible in bcc. In how far there are "selection rules" between which planes double slip according to the Neumann model is possible, could be investigated by performing experiments on single crystals.

The automation of the registration and segmentation procedures is currently being established on the 140 PCT volumes of the VST55531 dataset. This dataset is promising to investigate more clearly the effects of crack retardation at grain boundaries. Later on, the fatigue experiment on this sample should be continued. It will give deeper insight in the mechanism behind the formation of the striations in stage I. Perhaps even the fracture of the grain boundary that is necessary to bridge the incompatibility of the slip planes might be visible.

This work has been the ground for a recently accepted A.N.R. project (research project funded by the French national agency for research) coupling 3DXTSM observations with crystal plasticity finite element simulations.

Bibliography

Auld, B. (1973). *Acoustic Fields and Waves in Solids*, volume 1. J. Wiley and Sons, New York. 48

Bania, P. (1994). Beta titanium alloys and their role in the titanium industry of special interest. *Journal of Metals*, 46:16–19. 29

Baruchel, J., Buffière, J.-Y., Maire, E., Merle, P., and Peix, G., editors (2000). *X-ray tomography in Material Science: General Principles*. Hermes Science Publications, Paris. 37

Beucher, S. and Lantuéjoul, C. (1979). Use of watersheds in contour detection. In *International workshop on image processing, real-time edge and motion detection*. 50

Bhattacharjee, A., Bhargava, S., Varma, V., Kamat, S., and Gogia, A. (2005). Effect of β grain size on stress induced martensitic transformation in β solution treated Ti-10V-2Fe-3Al alloy. *Scripta Materialia*, 53:195–200. 77

Birosca, S., Buffière, J., Garcia-Pastor, F., Karadge, M., Babout, L., and Preuss, M. (2009). Three-dimensional characterization of fatigue cracks in Ti-6246 using X-ray tomography and electron backscatter diffraction. *Acta Materialia*, 57(19):5834–5847. 25

Blankenship, C. and Starke, E. (1991). The fatigue crack growth behavior of the Al-Cu-Li alloy Weldalite049. *Fatigue and Fracture of Engineering Materials and Structures*, 14:103–114. 100

Blom, A. F., Hedlund, A., Zahao, W., Fathulla, A., Weiss, B., and Stickler, R. (1986). *The behaviour of short fatigue cracks*, chapter : Short fatigue crack growth in Al2024 and Al7457, page 37. Mechanical Engineering Publications, London. 20

Bosak, A., Krisch, M., Mohr, M., Maultzsch, J., and Thomsen, C. (2007). Elasticity of single-crystalline graphite: Inelastic X-ray scattering study. *Physical Review B*, 75:153408. 48

Bosak, A., Serrano, J., Krisch, M., Watanabe, K., Taniguchi, T., and Kanda, H. (2006). Elasticity of hexagonal boron nitride: Inelastic X-ray scattering measurements. *Physical Review B*, 73:041402(R). 48

Brechet, Y., Louchet, F., Marchionni, C., and Verger-Gaugry, J. (1987). Experimental (TEM and STEM) investigation and theoretical approach to the fatigue-induced dissolution of δ' precipitates in a 2.5 wt% Al-Li alloy. *Philosophical Magazine A*, 56(3):353–366. 106

Buffière, J.-Y., Ferrié, E., Proudhon, H., and Ludwig, W. (2006). Three-dimensional visualisation of fatigue cracks in metals using high resolution synchrotron X-ray microtomography. *Materials Science and Technology*, 22(9):1019–1024. 11, 43, 44

Burgers, W. and Jacobs, F. (1936). Crystal structure of beta-titanium. *Zeitschrift f"ur Kristallographie, Kristallgeometrie, Kristallphysik, Kristallchemie*, 94:299–300. 77

Chesnutt, J. C. and Froes, F. H. (1977). Effect of α-phase morphology and distribution on the tensile ductility of a metastable beta titanium alloy. *Metallurgical and Materials Transactions A*, Volume 8, Number 6,:1013–1017. 30

Christ, H.-J. (1991). *Wechselverformung von Metallen - Zyklisches Spannungs-Dehnungs-Verhalten und Mikrostruktur*. Springer-Verlag. 22, 24

Clément, N., Lenain, A., and Jacques, P. (2007). Mechanical property optimization via microstructural control of new metastable beta titanium alloys. *Journal of Metals*, 59(1):50. 28

Clément, P., Angéli, J., and Pineau, A. (1984). Short crack behaviour in nodular cast iron. *Fatigue and Fracture of Engineering Materials and Structures*, 7(4):251. 25

Cloetens, P. (1999). *Contribution to phase contrast imaging, reconstruction and tomography with hard synchrotron radiation - Principles, implementation and applications*. PhD thesis, Vrije Universiteit Brussel. 37, 38, 52

Cloetens, P., Ludwig, W., Baruchel, J., Dyck, D. V., Van Landuyt, J., Guigay, J., and Schlenker, M. (1999). Holotomography: Quantitative phase tomography with micrometer resolution using hard synchrotron radiation x rays. *Applied Physics Letters*, 75:2912–2914. 82

Cloetens, P., Pateyron-Salomé, M., Buffière, J.-Y., Peix, G., Baruchel, J., Peyrin, F., and Schlenker, M. (1997). Observation of microstructure and damage in materials by phase sensitive radiography and tomography. *Journal of Applied Physics*, 81(9):5878–5886. 38, 43

Collings, E. (1986). *Applied Superconductivity, Metallurgy, and Physics of Titanium Alloys, Volume 1: Fundamentals*. Springer Verlag Gmbh, 1 edition. 74

Cox, B. and Morris, W. (1988). Monte Carlo simulations of the growth of small fatigue cracks. *Engineering Fracture Mechanics*, 31(4):591–610. 95

Davidson, D., Chan, K., McClung, R., and Hudak, S. (2003). *Comprehensive Structural Integrity*, volume 4 Cyclic Loading and Fatigue, chapter : Small fatigue cracks, pages 129–64. Elsevier. 18, 21, 22

Davidson, D. L., Chan, K., and McClung, R. C. (1996). Cu-bearing high-strength low-alloy steels: The influence of microstructure on the initiation and growth of small fatigue cracks. *Metallurgical Transactions A*, 27:2540–2556. 18

De Witte, Y., Boone, M., Vlassenbroeck, J., Dierick, M., and Van Hoorebeke, L. (2009). Bronnikov-aided correction for X-ray computed tomography. *Journal of the Optical Society of America A*, 26(4):890–894. 82

Dey, S., Lauridsen, E., Ludwig, W., Rowenhorst, D., and Fonda, R. (2007). Study of microstructure evolution of grain boundary alpha phase during beta to alpha transformation in Timetal 21S alloy. In Ninomi, M., Akiyama, S., Ikeda, M., Hagiwara, M., and Maruyama, K., editors, *Proceedings of Titanium 2007 Science and Technology*, pages 467–470. The Japan Institute of Metals, Sendai, Japan. 9, 30, 75

Düber, O., Künkler, B., Krupp, U., Christ, H.-J., and Fritzen, C. (2006). Experimental characterization and two-dimensional simulation of short-crack propagation in an austenitic-ferritic duplex steel. *International Journal of Fatigue*, 28(9):983–992. 89

Duerig, Terlinde, and Williams (1980a). The omega-phase reaction in titanium alloy. In *Titanium 80, Science and Technology, Proceedings of the 4th International Conference on Titanium*. Metallurgical Society of AIME. 28

Duerig, T., Albrecht, J., Richter, D., and Fischer, P. (1982). Formation and reversion of stress induced martensite in Ti-10V-2Fe-3Al. *Acta Metallurgica*, 30:2161–2172. 73, 76, 77

Duerig, T., Terlinde, G., and Williams, J. (1980b). Phase transformations and tensile properties of Ti-10V-2Fe-3AI. *Metallurgical and Materials Transactions A*, 11(12):1987–1998. 30

Dunand, D. C. (2004). Processing of titanium foams. *Advanced Engineering Materials*, 6(6):369–376. 28

Eliezer, D., Tal-Gutelmacher, E., and Boellinghaus, T. (March, 2005). Hydrogen embrittlement in hydride- and non hydride- forming systems - microstructural / phase changes and cracking mechanisms. In *Proceedings of the 11th International Conference on Fracture, Turin, Italy*. 28

Fanning, J. (1993). Timetal 21S property data. In Eylon, D., Boyer, R., and Koss, D., editors, *Beta Titanium Alloys in the 1990's*, pages 397–410. TMS, Warrendale, PA. 29

Fanning, J. (2005). Properties of TIMETAL 555 (Ti-5Al-5Mo-5V-3Cr-0.6Fe). *Journal of Materials Engineering and Performance*, 14(6):788. 29

Feltner, C. E. and Laird, C. (1968). Factors influencing the dislocation structures in fatigued metals. *TMS-AIME*, 242:1253–1257. 23

Ferrié, E., Buffière, J., and Ludwig, W. (2005). 3D characterisation of the nucleation of a short fatigue crack at a pore in a cast Al alloy using high resolution synchrotron microtomography. *International Journal of Fatigue*, 27:1215–1220. 25

Ferrié, E., Buffière, J.-Y., Ludwig, W., Gravouil, A., and Edwards, L. (2006). Fatigue crack propagation: In situ visualization using X-ray microtomography and 3D simulation using the extended finite element method. *Acta Materialia*, 54(4):1111–1122. 32

Forsyth, P. (1962). A two stage process of fatigue crack growth. In *Crack Propagation: Proceedings of Cranfield Symposium*, pages 76–94. London: Her Majesty's Stationery Office. 21

Fréour, S., Gloaguen, D., François, M., Perronnet, A., and Guillén, R. (2005). Determination of single-crystal elasticity constants in a cubic phase within a multiphase alloy: X-ray diffraction measurements and inverse-scale transition modelling. *Journal of Applied Crystallography*, 38(1):30–37. 47

Gerold, V. and Karnthaler, H. (1989). On the origin of planar slip in f.c.c. alloys. *Acta Metallurgica*, 37:2177–2183. 24

Gordon, R., Bender, R., and Herman, G. (1970). Algebraic reconstruction techniques (ART) for three-dimensional electron microscopy and X-ray photography. *Journal of Theoretical Biology*, 29:471. 39

Gottstein, G. (2007). *Physikalische Grundlagen der Materialkunde*. Springer-Verlag, Berlin, Heidelberg. 76, 120

Guigay, J. P., Langer, M., Boistel, R., and Cloetens, P. (2007). Mixed contrast transfer and transport of intensity approach for phase retrieval in the Fresnel region. *Optics Letters*, 32:1617–1619. 82

Haicheng, G. and Shujuan, S. (1990). Microstructural effect on fatigue thresholds in β titanium alloy Ti-10V-2Fe-3Al. In *Fatigue90*. 76

Heinl, P., Rottmair, A., Koerner, C., and Singer, R. F. (2007). Cellular titanium by selective electron beam melting. *Advanced Engineering Materials*, 9(5):360–364. 28

Heinz, A. and Neumann, P. (1991). Representation of orientation and disorientation data for cubic, hexagonal, tetragonal and orthorombic crystals. *Acta Crystallographica Section A: Foundations of Crystallography*, 47(6):780–789. 40

Hendriks, C., van Vliet, L., Rieger, B., van Kempen, G., and van Ginkel, M. (1999-2010). DIPimage user manual. Technical report, Quantitative Imaging Group, Delft University of Technology, Delft, The Netherlands, http://www.qi.tnw.tudelft.nl/DIPlib. 52

Herbig, M., King, A., Reischig, P., Proudhon, H., Lauridsen, E. M., Marrow, J., Buffière, J.-Y., and Ludwig, W. (2011). 3D growth of a short fatigue crack within a polycrystalline microstructure studied using combined diffraction and phase contrast X-ray tomography. *Acta Materialia*, 59:590–601. 11, 26, 57, 60

Hertzberg, R. (1995). *Deformation and Fracture Mechanics of Engineering Materials.* Wiley, 4th edition. 24

Hirsch, P. and Humphreys, F. (1969). *Physics of Strength and Plasticity.* M.I.T. Press, Cambridge. 24

Holzapfel, C., Schäf, W., Marx, M., Vehoff, H., and Mücklich, F. (2007). Interaction of cracks with precipitates and grain boundaries: Understanding crack growth mechanisms through focused ion beam tomography. *Scripta Materialia*, 56:697–700. 25, 88

Honeycombe, R. (1984). *Plastic Deformation of Metals.* Edward Arnold, London, 2nd sub edition. 63, 85

Hornbogen, E. and zum Gahr, K.-H. (1976). Microstructure and fatigue crack growth in a γ-Fe-Ni-Al alloy. *Acta Metallurgica*, 24:581–592. 92

Jackson, J. (1999). *Classical Electrodynamics.* John Wiley & Sons, Inc., 3 edition. 35

Johnson, G., King, A., Honnicke, M., Marrow, T., and Ludwig, W. (2008). X-ray diffraction contrast tomography: a novel technique for three-dimensional grain mapping of polycrystals. II. the combined case. *Journal of Applied Crystallography*, 41:310–318. 26

Kak, A. C. and Slaney, M. (2001). *Principles of Computerized Tomographic Imaging.* Society of Industrial and Applied Mathematics. 37, 38, 52, 80

Kim, H. S., Lim, S. H., Yeo, I. D., and Kim, W. Y. (2007). Stress-induced martensitic transformation of metastable beta-titanium alloy. *Materials Science and Engineering: A*, 449-451:322–325. 73, 77

King, A., Herbig, M., Ludwig, W., Reischig, P., Lauridsen, E., Marrow, T., and Buffière, J.-Y. (2010). Non-destructive analysis of micro texture and grain boundary character from X-ray diffraction contrast tomography. *Nuclear Instruments and Methods in Physics Research B - Beam Interactions with Materials and Atoms*, 268(3-4):291–296. 69, 70

Krupp, U. (2007). *Fatigue crack propagation in metals and alloys: microstructural aspects and modelling concepts.* Wiley-VCH, Weinheim. 18, 19, 20, 21, 89, 100

Kubin, L. (2011). *Mesoscale Simulations of Dislocations and Plasticity.* Clarendon Press, Oxford. 105

Kuroda, D., Niinomi, M., Morinaga, M., Kato, Y., and Yashiro, T. (1998). Design and mechanical properties of new β type titanium alloys for implant materials. *Materials Science and Engineering A*, 243(1-2):244–249. 47

Labiche, J.-C., Maton, O., Pascarelli, S., Newton, M., Ferre, G., Curfs, C., Vaughan, G., Homs, A., and Carreiras, D. (2007). The FReLoN camera as a versatile X-ray detector for time resolved dispersive EXAFS and diffraction studies of dynamic problems in materials science, chemistry and catalysis. *Review of Scientific Instruments*, 78:091301. 36, 43

Laird, C. and Smith, G. (1962). Crack propagation in high stress fatigue. *Philosophical Magazine*, 77:847. 21, 22

Laird, C. and Thomas, G. (1967). On fatigue-induced reversion and overaging in dispersion strengthened alloys systems. *International Journal of Fracture Mechanics*, 3:81–97. 21

Langer, M. (2008). *Phase Retrieval in the Fresnel Region for Hard X-ray Tomography*. PhD thesis, INSA Lyon. 37

Langer, M., Cloetens, P., and Peyrin, F. (2010). Regularization of phase retrieval with phase-attenuation duality prior for 3D holotomography. *IEEE Transactions on Image Processing*, 19:2428–2436. 82

Lankford, J. (1982). The growth of small fatigue cracks in 7075-T6 aluminium. *Fatigue of engineering materials and structures*, 5:233. 19, 20

Leyens, C. and Peters, M., editors (2003). *Titanium and Titanium Alloys - Fundamentals and Applications*. Wiley-VCH. 28, 34

Li, S., Cui, T., Hao, Y., and Yang, R. (2008). Fatigue properties of a metastable b-type titanium alloy with reversible phase transformation. *Acta Biomaterialia*, 4:305–317. 76

Ludwig, W., Buffière, J., Savelli, S., and Cloetens, P. (2003). Study of the interaction of a short fatigue crack with grain boundaries in a cast Al alloy using X-ray microtomography. *Acta Materialia*, 51:585–595. 25

Ludwig, W., King, A., Reischig, P., Herbig, M., Lauridsen, E., Schmidt, S., Proudhon, H., Forest, S., Cloetens, P., du Roscoat, S. R., Buffière, J., Marrow, T., and Poulsen, H. (2009a). New opportunities for 3D materials science of polycrystalline materials at the micrometre lengthscale by combined use of X-ray diffraction and X-ray imaging. *Materials Science and Engineering: A*, 524(1-2):69–76. 25

Ludwig, W., Reischig, P., King, A., Herbig, M., Lauridsen, E., Marrow, T., and Buffière, J. (2009b). Three-dimensional grain mapping by X-ray diffraction contrast tomography and the use of friedel pairs in diffraction data analysis. *Review of Scientific Instruments*, 80:033905. 26, 39, 42, 45, 52

Lukáš, P. and Klesnil, M. (1972). Fatigue damage and dislocation substructure. In Devereux, O., McEvily, A., and Staehl, R., editors, *Proceedings of the 2nd international conference on corrosion fatigue, Storrs, Connecticut, 1971*, pages 118–132. National Association of Corrosion Engineers NACE, Houston, Texas. 23

Martin, T. and Koch, A. (2006). Recent developments in X-ray imaging with micrometer spatial resolution. *Journal of Synchrotron Radiation*, 13:172–179. 36, 43

Mayo, S., Miller, P., Wilkins, S., Davis, T., Gao, D., Gureyev, T., Paganin, D., Parry, D., Pogany, A., and Stevenson, A. (2002). Quantitative X-ray projection microscopy: phase-contrast and multi-spectral imaging. *Journal of Microscopy*, 207(2):79–96. 81, 98

McMillian, J. and Pelloux, R. (1967). *Fatigue crack propagation under program and random loads, Special Technical Publications 415.* American Society for Testing and Materials, Philadelphia. 22

Miller, K. and de los Rios, E., editors (1992). *Short Fatigue Cracks - European Structural Integrity Society, Publication 13.* Mechanical Engineering Publications, London. 24

Miller, K., Mohamed, H., and de los Rios, E. (1986). *The behaviour of short fatigue cracks*, chapter : Fatigue damage accumulation above and below the fatigue limit, page 491. Mechanical Engineering Publications, London. 18

Mokso, R., Cloetens, P., Maire, E., Ludwig, W., and Buffière, J.-Y. (2007). Nanoscale zoom tomography with hard X rays using Kirkpatrick-Baez optics. *Applied Physics Letters*, 90:144104. 81, 106

Murakami, Y. (1980). Critical review of phase transformations and heat treatment. In *Titanium 80, Science and Technology, Proceedings of the 4th International Conference on Titanium*, page 156. Metallurgical Society of AIME. 28

Nadot, Y., Ranganathan, N., Mendez, J., and Béranger, A. (1997). A study of natural cracks initiated on casting defects by crack front marking. *Scripta Materialia*, 37(5):549–553. 25

Nag, S. (2008). *Influence of beta instabilities on the early stages of nucleation and growth of alpha in beta titanium alloys.* PhD thesis, The Ohio State University. 29

Navarro, A. and de los Rios, E. (1988). Short and long fatigue crack growth: A unified model. *Philosophical Magazine A*, 57:15. 94

Neelakantan, S., del Castilloa, P. R.-D., and van der Zwaaga, S. (2009). Prediction of the martensite start temperature for β titanium alloys as a function of composition. *Script Materialia*, 60:611–614. 76

Neumann, P. (1969). Coarse slip model of fatigue. *Acta Metallurgica*, 17:1219–25. 21, 23

Neumann, P., Fuhlrott, H., and Vehoff, H. (1979). Experiments concerning brittle, ductile, and environmentally controlled fatigue crack growth. In *Fatigue Mechanisms*, pages 371–395. Proceedings of an ASTM-NBS-NSF symposium, Kansas City, Mo, May 1978, American Siciety ofr Testing and Materials. 91

Neumann, P., Vehoff, H., and Fuhlrott, H. (1977). On the mechanisms of fatigue crack growth. In *Fracture 1977, Part IV, Fatigue: Mechanisms*, volume 2, pages 1313–1324, ICF4, Waterloo, Canada. 91

Newman, J. (1998). The merging of fatigue and fracture mechanics concepts: a historical perspective. *Progress in Aerospace Sciences*, 34:347–390. 24

Newman, J. J. (1992). FASTRAN II: A fatigue crack growth structural analysis program. Technical report, NASA TM 104159. 19

Newman., J. J., Phillips, E., and Swain, M. (1999). Fatigue-life prediction methodology using small crack theory. *International Journal of Fatigue*, 21:109. 19, 20

Paganin, D., Mayo, S., Gureyev, T., Miller, P., and Wilkins, S. (2002). Simultaneous phase and amplitude extraction from a single defocused image of a homogeneous object. *Journal of Microscopy*, 206:33–40. 82

Paris, P. and Erdogan, F. (1960). A critical analysis of crack propagation laws. *Journal of Basic Engineering*, 85:528. 17, 18

Pearson, S. (1975). Initiation of fatigue cracks in commercial aluminium alloys and the subsequent propagation of very short cracks. *Engineering Fracture Mechanics*, 7:235–247. 18, 19, 24, 25

Penning, P. (1976). Minimization of shears for pencil glide in body-centered cubic crystals. *Metallurgical and Materials Transactions A*, 7(6):1021–1026. 88

Petzow, G. (1978). *Metallographic Etching*. American Society for Metals, Metals Park, Ohio. 34

Pineau, A. (1986). Short fatigue crack behavior in relation to three-dimensional aspects and crack closure effect. In Ritchie, R. and Lankford, J., editors, *Small fatigue Cracks: 2nd International Conference, Santa Barbara, USA*, pages 191–211. Metallurgical Society of AIME, Warrendale, PA. 24

Pommier, S. (2002). 'Arching' effect in elastic polycrystals: implications for the variability of fatigue lives. *Fatigue and Fracture of Engineering Materials and Structures*, 25(4):331–348. 24

Poulsen, H. (2004.). *Three-Dimensional X-Ray Diffraction Microscopy: Mapping Polycrystals and their Dynamics*. Springer, Berlin, 1 edition. 26, 40

Proudhon, H., Forest, S., and Ludwig, W. (2010). Large scale finite element simulations of polycrystalline aggregates: applications to X-ray diffraction and imaging for fatigue metal behaviour. In Hansen, N., Jensen, D. J., Nielsen, S., Poulsen, H., and Ralph, B., editors, *Proceedings of the 31st Risø International Symposium of Materials Science*. Risø National Laboratory for Sustainable Energy, Technical University of Denmark, Roskilde, Denmark. 97

Qiao, Y. and Argon, A. (2003a). Cleavage crack-growth-resistance of grain boundaries in polycrystalline Fe-2%Si alloy: experiments and modeling. *Mechanics of Materials*, 35:129–154. 94

Qiao, Y. and Argon, A. (2003b). Cleavage cracking resistance of high angle grain boundaries in Fe-3%Si alloy. *Mechanics of Materials*, 35:313–331. 94

Qiao, Y. and Kong, X. (2004). An energy analysis of the grain boundary behavior in cleavage cracking in Fe-3wt.%Si alloy. *Materials Letters*, 58:3156–3160. 94

Ravichandran, K. and Li, X. (2000). Fracture mechanical character of small cracks in polycrystalline materials: concept and numerical K calculations. *Acta Materialia*, 48:525540. 24

Ravichandran, K., Ritchie, R., and Murakami, Y., editors (1999). *Small Fatigue Cracks: Mechanics, Mechanisms and Applications*. Elsevier, Oxford, UK. 24

Reid, C. N., Routbort, J. L., and Maynard, R. A. (1973). Elastic constants of Ti 40 at.% Nb at 298 K. *Journal of Applied Physics*, 44:1398–1399. 47

Ritchie, R. and Lankford, J., editors (1986). *Small Fatigue Cracks*. Metallurgical Society, Warrendale, PA. 24

Ro, Y., Agnew, S., and Gangloff, R. (2007). Crystallography of fatigue crack propagation in precipitation-hardened Al-Cu-Mg/Li. *Metallurgical and Materials Transactions A*, 38A(12):3042–3062. 88

Rodrigues (1840). Title unknown. *Journal of Pure and Applied Mathematics*, 5:380–440. 39

Ruppen, J., Bhowal, P., Eylon, D., and McEvily, A. (1979). On the process of subsurface fatigue crack initiation in Ti-6Al-4V. In Fong, J., editor, *Fatigue Mechanisms. Proceedings of an ASTM-NBS-NSF symposium*, pages 47–68. 19

Russ, J. (2003). *The Image Processing Handbook*. CRC Press LLC, Boca Raton, Florida. 45

Schäf, W. (2010). *Über die Wechselwirkung kurzer Ermüdungsrisse mit Korngrenzen: Systematische Experimente mit Focussed Ion Beam Microscope und mikrostruktureller Tomographie*. PhD thesis, Naturwissenschaftlich-Technischen Fakulät III Chemie, Pharmazie, Bio- und Werkstoffwissenschaften der Universität des Saarlandes. 8, 20

Schäf, W., Marx, M., Vehoff, H., Heckl, A., and Randelzhofer, P. (2011). A 3D-view on the mechanisms of short fatigue cracks interacting with grain boundaries. *accepted by Acta Materialia*. 20, 25, 26, 88, 92, 93

Schijve, J. (2009). *Fatigue of Structures and Materials*. Springer, 2 edition. 17

Schubert, K., Meissner, H. G., Poetzschke, M., Rossteutscher, W., and Stolz, E. (1962). Einige Strukturdaten metallischer Phasen. VII. *Naturwissenschaften*, 49:57. 77

Sharma, B. and Donohue, J. (1962). A refinement of the crystal structure of gallium. *Zeitschrift fuer Kristallographie, Kristallgeometrie, Kristallphysik, Kristallchemie*, 117:293. 77

Shiozawa, K. and Matsushita, H. (1996). Crack initiation and small fatigue crack growth behaviour of beta Ti-15V-3Cr-3Al-3Sn alloy. In Lütjering, G. and Nowark, H., editors, *Fatigue '96, Proceedings of the Sixth International Fatigue Congress*, page 301. Pergamon, Berlin. 17

Smith, S. W. (1997). *The Scientist and Engineer's Guide to Digital Signal Processing*. California Technical Publishing. 39, 40

Spowart, J. (2006). Automated serial sectioning for 3-D analysis of microstructures. *Scripta Materialia*, 55(1):5–10. 25

Suresh, S. (2003). *Fatigue of Materials*. University Press, Cambridge, 2nd edition. 19, 21

Suresh, S. and Ritchie, R. (1984). Propagation of short fatigue cracks. *International Metal Reviews*, 29:445–76. 20

Szanto, I. (1955). On the determination of high-purity alpha-titanium lattice parameters. *Acta Technica Academiae Scientarum Hungaricae*, 13:363–372. 77

Tanaka, K. and Mura, T. (1984). Fatigue crack growth along planar slip bands. *Acta Metallurgica*, 32(10):1731–1740. 23

Taylor, B. and Weidmann, E. (2008). Application notes - metallographic preparation of titanium. Technical report, Struers. 31

Taylor, C., Zhai, T., Wilkinson, A., and Martin, J. (1999). Influence of grain orientations on the initiation of fatigue damage in an Al-Li alloy. *Journal of Microscopy-Oxford*, 195:239–247. 25

Terlinde, G. and Fischer, G. (1996). Titanium 95. In Blenkinsop, P., Evans, W., and Flower, H., editors, *Science and Technology*, pages 2177–2194. Institute of Metals, London. 29, 30

Timet (2010). TIMETAL 21S: high strength, oxidation resistant strip alloy. Technical report, http://www.timet.com/pdfs/21S.pdf. 29

Vehoff, H. and Neumann, P. (1987). In situ SEM experiments concerning the mechanism of ductile crack growth. *Acta Metallurgica*, 27:915–920. 23

Venkateswara Rao, K., Yu, W., and Ritchie, R. (1988). Fatigue crack propagation in aluminum- lithium alloy 2090: Part I. long crack behavior. *Metallurgical and Materials Transactions A*, 19(3):549–561. 105

Verreman, Y. and Nie, B. (1996). Early development of fatigue cracking at manual fillet welds. *Fatigue and Fracture of Engineering Materials and Structures*, 19(6):669–681. 25

Weiss, I. and Semiatin, S. (1998). Thermomechanical processing of beta titanium alloys - an overview. *Materials Science and Engineering A*, 243:46–65. 28, 29

Welsch, G., Boyer, R., and Collings, E. W., editors (1994). *Materials properties handbook: titanium alloys*. ASM International. 27, 29, 31, 76

Wilkinson, A., Henderson, M., and Martin, J. (1996). Examination of fatigue crack plastic zones using scanning-electron-microscope-based electron diffraction techniques. *Philosophical Magazine Letters*, 74(3):145–151. 25

Wilkinson, A., Roberts, S., and Hirsch, P. (1998). Modelling of the threshold conditions for propagation of stage I fatigue cracks. *Acta Materialia*, 46:379. 21

Yang, Y., Li, G. P., Cheng, G. M., Li, Y. L., and Yang, K. (2009). Multiple deformation mechanisms of Ti-22.4Nb-0.73Ta-2.0Zr-1.34O alloy. *Applied Physics Letters*, 94(061901):1–3. 73, 77

Zaefferer, S., Wright, S., and Raabe, D. (2008). Three-dimensional orientation microscopy in a focused ion beam-scanning electron microscope: A new dimension of microstructure characterization. *Metallurgical and Materials Transactions A*, 39A:374. 25

Zappfe, C. and Worden, C. (1951). Fractographic registrations of fatigue. *Transactions of the American Society for Metals*, 43:985–69. 21

Zhai, T., Jiang, X., Li, J., Garratt, M., and Bray, G. (2005). The grain boundary geometry for optimum resistance to growth of short fatigue cracks in high strength Al alloys. *International Journal of Fatigue*, 27:1202. 20

Zhai, T., Wilkinson, A., and Martin, J. (2000). A crystallographic mechanism for fatigue crack propagation through grain boundaries. *Acta Materialia*, 48:4917. 20, 88, 93

Zhang, Y. and Edwards, L. (1992). Effect of grain boundaries on the development of plastic deformation ahead of small fatigue cracks. *Scripta Metallurgica et Materialia*, 26(12):1901–1906. 25, 94

Zwicker, U. (1974). *Titan und Titan-Legierungen*. Springer Verlag, Berlin-Heidelberg-New York. 28

Index

Appendix

The Schmid Factor

Schmid's law [Gottstein, 2007] links an uniaxial load applied to a body with the shear stresses acting on a certain plane in a certain direction of the body. The law can be applied to calculate how much shear stress is resolved on a slip system in an uniaxially loaded single crystal (see figure 1). If F is the uniaxially applied load acting on the crystal's cross section S_0, χ is the angle between F and the slip plane normal and Θ the angle between F and the slip direction then the resolved shear stress τ on the slip system is:

$$\tau = \frac{F}{S_0} \cdot \cos(\Theta) \cdot \cos(\chi). \tag{1}$$

$\cos(\Theta) \cdot \cos(\chi)$ varies between 0 and .5 and is called the Schmid factor or the slip plane activation.

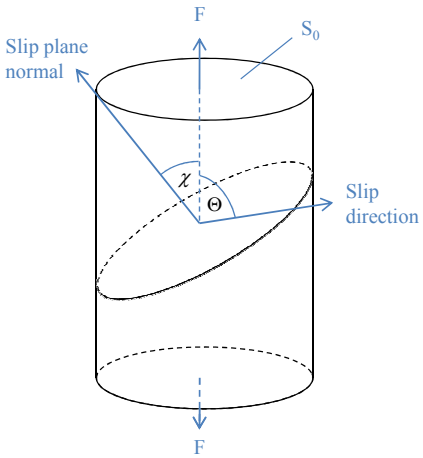

Figure 1: Using Schmid's law the activation of each slip system in a single crystal can be calculated.

Preparation of the IXS Sample

The inelastic X-ray scattering experiment requires a sample that is plastically undeformed, has a thickness of about 100 μm, is polished on both sides, has a grain size big

enough so that at most places only a single grain is in the sample cross-section and has a very clean sample surface. Additionally, the grain boundaries must be deeply etched (at least 3-5 μm) on both sides in order to make them visible during the experiment. A 3 mm x 3 mm x 1.6 mm part of Beta21S received an additional heat treatment for 20 hours at 860 °Cin order to increase the grain size to about 150 μm and was subsequently quenched in water. In order to ease co-planar grinding the sample was embedded in just enough resin to cover the surface. The polymerase reaction was aided by heating the resin for several minutes on a hot plate at 100 °C. The bottom side of the embedded sample was glued to a cylindrical metal sample holder using wax (Tripod wax, Struers). At least 100 μm were removed from the first side by grinding and polishing. Etching was done for 7.5 minutes. After turning the sample the procedure was repeated. The final sample thickness was between 70 and 160 μm.

Publications

Peer-reviewed

Herbig, M., King, A., Reischig, P., Proudhon, H., Lauridsen, E. M., Marrow, J., Buffière, J.-Y., and Ludwig, W. (2011). 3D growth of a short fatigue crack within a polycrystalline microstructure studied using combined diffraction and phase contrast X-ray tomography. *Acta Materialia*, 59:590-601.

Ludwig, W., King, A., Herbig, M., Reischig, P., Proudhon, H., and Buffière, J.-Y. (2010b). Characterization of polycrystalline materials by combined use of synchrotron X-ray imaging and diffraction techniques. *Journal of Metals*, 62(12):22–28.

King, A., Herbig, M., Ludwig, W., Reischig, P., Lauridsen, E., Marrow, T., and Buffière, J.-Y. (2010). Non-destructive analysis of micro texture and grain boundary character from X-ray diffraction contrast tomography. *Nuclear Instruments and Methods in Physics Research B - Beam Interactions with Materials and Atoms*, 268(3-4):291–296.

Ludwig, W., Reischig, P., King, A., Herbig, M., Lauridsen, E., Marrow, T., and Buffière, J. (2009b). Three-dimensional grain mapping by X-ray diffraction contrast tomography and the use of Friedel pairs in diffraction data analysis. *Review of Scientific Instruments 2009*, 80:033905.

Ludwig, W., King, A., Reischig, P., Herbig, M., Lauridsen, E., Schmidt, S., Proudhon, H., Forest, S., Cloetens, P., du Roscoat, S. R., Buffière, J., Marrow, T., and Poulsen, H. (2009a). New opportunities for 3D materials science of polycrystalline materials at the micrometre lengthscale by combined use of X-ray diffraction and X-ray imaging. *Materials Science and Engineering: A*, 524(1-2):69–76.

Non peer-reviewed

Proudhon, H., Herbig, M., Buffière, J.-Y., and Ludwig, W. (9-13 Mai 2011). Simulation par éléments finis de la déformation de polycristaux à partir d'images de tomographie par contraste de diffraction. In *CSMA 2011, 10e Colloque National en Calcul des Structures, Presqu'île de Giens (Var).*

Ludwig, W., Herbig, M., King, A., Reischig, P., Proudhon, H., and Buffière, J. (June 2010a). The grain microstructure of polycrystalline materials as revealed by the combined use of synchrotron X-ray imaging and diffraction techniques,. In *Actes des Journées Annuelles de la Société Française de Métallurgie et de Matériaux, Paris*.

Ludwig, W., Reischig, P., King, A., Herbig, M., Proudhon, H., Buffière, J.-Y., Rutishauser, S., and David, C. (2010c). Thoughts about the optimum data acquisition geometry and time resolution of monochromatic beam X-ray diffraction microscopy experiments. In *Proceedings of the 31st Risø Int. Symposium on Materials Science, Risø National Laboratory for Sustainable Energy, Technical University of Denmark, Roskilde, Denmark*.

FOLIO ADMINISTRATIF

THESE SOUTENUE DEVANT L'INSTITUT NATIONAL DES SCIENCES APPLIQUEES DE LYON

NOM : HERBIG
(avec précision du nom de jeune fille, le cas échéant)

DATE de SOUTENANCE : 26/01/2011

Prénoms : Michael

TITRE : 3D Short Fatigue Crack Investigation in Beta Titanium Alloys using Phase and Diffraction Contrast Tomography

NATURE : Doctorat

Numéro d'ordre : 05 ISAL

Ecole doctorale : Matériaux de Lyon

Spécialité :

Cote B.I.U. - Lyon : T 50/210/19 / et bis

CLASSE :

RESUME :

X-Ray Diffraction Contrast Tomography (DCT) is a recently developed, non-destructive synchrotron imaging technique which characterizes microstructure and grain orientation in polycrystalline materials in three dimensions (3D). By combining it with propagation based phase contrast tomography (PCT) it is for the first time possible to observe in situ the 3D propagation behavior of short fatigue cracks (SFCs) within a set of fully characterized grains (orientation and shape). The combined approach, termed 3-Dimensional X-ray Tomography of Short cracks and Microstructure (3DXTSM), has been developed on the metastable beta titanium alloy “Beta21S”.

A big part of this work deals with the challenges encountered during development of the 3DXTSM methodology. In the combined dataset, each point on the 3D fracture surface can be associated with a multidimensional data structure containing variables describing the grain orientation, the local fracture surface normal and the propagation history. The method uses a surface mesh composed of triangles that describes the crack (in other words: the fracture surface) in the last propagation state measured. Grain orientations, crack fronts, local growth rates and grain boundaries can be visualized by assigning colors to this mesh. The data structure can be interrogated in a number of different ways. Tools for extracting pole figures and pole density distribution functions have been implemented. An algorithm was developed that is capable of measuring the 3D local growth rate of a crack containing branches. The accuracy of the grain boundaries as reconstructed with DCT was evaluated and the elastic constants of Beta21S were determined.

The first experiment, conducted on the metastable beta titanium alloy Beta21S, allowed to establish and validate the 3DXTSM methodology itself. The quantitative analysis of crack propagation in this alloy was compromised by the fact that changes in crack propagation behavior occur at length scales which could only partly be resolved with the experimental settings used. Apart from the resolution the slip character was identified as one of the key factors that decide in how far the measured data represents reality and thereby about the data interpretability. A second 3DXTSM experiment using optimized conditions was designed and conducted on the near beta alloy “VST55531”. The observation of crystallographic growth behavior in this alloy confirms the prevalence of stage I crack propagation.

Due to the 3D nature of this study it could be observed that the orientation of the corrugated fracture surface patterns visible during stage I is independent of the crack growth direction. The characteristics of stage I and II were correspondingly revised. No correlation between slip directions and growth direction of a crack propagating on a single slip plane was observed.

The crystallographic orientation of the fracture facets observed do not correspond to the most activated slip systems (Schmid factor). This suggests that modifications of the stress field due to the 3D crack geometry and the elastic anisotropy of the material need to be taken into account to model crack propagation. This could be achieved, in future work, using crystal plasticity finite element simulations.

MOTS-CLES : 3D, short fatigue crack, synchrotron imaging, beta titanium, phase contrast tomography, diffraction contrast tomography

Laboratoire (s) de recherche : MATEIS UMR CNRS 5510

Directeur de thèse: Jean-Yves BUFFIERE et Wolfgang LUDWIG

Président de jury :

Composition du jury : Ulrich KRUPP (rapporteur), Maxime SAUZAY (rapporteur), Haël MUGHRABI (examineur), Jean PETIT (examineur) et Henry PROUDHON (examineur)